Recommended Practices in Laser-Induced Fluorescence (LIF) Diagnostics for Electric Propulsion

Vernon H. Chaplin[*]
Jet Propulsion Laboratory, California Institute of Technology, Pasadena, CA 91109, USA

Stéphane Mazouffre[†]
ICARE-CNRS, 45071 Orléans, France

Wensheng Huang[‡]
NASA Glenn Research Center, Cleveland, OH 44135, USA

Christoph Eichhorn[§]
Leibniz Institute of Surface Engineering (IOM), Permoserstr. 15, 04318 Leipzig, Germany

Azer P. Yalin[¶]
Colorado State University, Fort Collins, CO 80523, USA

Parker J. Roberts[‖] and Benjamin A. Jorns[**]
University of Michigan, Ann Arbor, MI 48105, USA

Mark W. Crofton[††]
Consultant, Rancho Palos Verdes, CA 90275, USA

Abstract

Laser-induced fluorescence (LIF) spectroscopy uses Doppler-shifted laser photons to excite a bound electron transition in an atom or ion, with subsequent fluorescence emission detected in order to measure the local velocity distribution function (VDF) and/or particle density. Due to its non-invasive nature, high spatial resolution, and acceptable difficulty of implementation, LIF has become a favored diagnostic for electric propulsion (EP) plasmas, particularly in the study of Hall thrusters. This paper presents recommended best practices for LIF measurements in electric thrusters, drawn from over three decades of implementation heritage in the EP community. Focusing on both single-photon LIF (typically used to measure VDFs) and two-photon LIF (TALIF, typically used to determine densities), the paper covers selection of atomic transitions to target, experimental setups, and interpretation of data.

---

[*] Technologist, Electric Propulsion Group, vernon.h.chaplin@jpl.nasa.gov

[†] Research Director, ICARE, CNRS, stephane.mazouffre@cnrs-orleans.fr

[‡] Research Engineer, Electric Propulsion Systems Branch, wensheng.huang@nasa.gov

[§] Senior Researcher, Tools Department, christoph.eichhorn@iom-leipzig.de

[¶] Professor, Department of Mechnical Engineering, azer.yalin@colostate.edu

[‖] Doctoral Candidate, Department of Aerospace Engineering, pjrob@umich.edu

[**] Associate Professor, Department of Aerospace Engineering, bjorns@umich.edu

[††] Consultant, mwcrofton@outlook.com

Part I

Single Photon Absorption LIF

1 Introduction

Laser-induced fluorescence (LIF) is an active spectroscopic technique that enables spatially resolved measurements of the velocity distributions and densities of atoms and ions. Following the invention of the laser and rapid advancement of the technology in the 1960s, LIF was first applied as a plasma diagnostic by Stern and Johnson in 1975 [1]. Applications to electric thrusters running on xenon propellant began in the 1990s with pioneering measurements in Hall thrusters by Manzella [2] and Cedolin et al. [3]. Around this time, development of narrow linewidth tunable diode lasers [4] facilitated easier implementation of the diagnostic, and in the years that followed improvements in experimental techniques and analysis methods were reported in numerous research articles and PhD theses [5–17]. Thanks to its non-invasive nature (in contrast to inserted probes that can perturb the discharge [18, 19]), LIF has become a central tool in the study of Hall thruster physics and computational model validation [20–23], and valuable applications have been demonstrated for other electric propulsion (EP) technologies such as gridded ion thrusters [24], arcjets [25], hollow cathodes [26, 27], magnetic nozzles [28], and field emission thrusters [29].

LIF works by setting the laser wavelength to excite a bound electron transition in the target atom or ion species; the subsequent fluorescence emission produced as the electron spontaneously falls back to a lower energy state is detected, producing a signal proportional to the total rate of laser photon absorption events in the measurement volume. Particles with finite velocity component v_x in the direction toward the laser source will see the incoming photons Doppler shifted, such that for a transition with rest frame wavelength λ_0, laser photons with wavelength λ will interact with particles moving at velocity

$$v_x = c\left(\frac{\lambda}{\lambda_0} - 1\right). \tag{1}$$

In the most common application, the laser is scanned across a range of wavelengths around λ_0 to map out the 1D velocity distribution function (VDF), where the fluorescence signal is approximately proportional to the instantaneous laser intensity and the density of target particles with velocity near v_x (line profile broadening mechanisms that determine quantitatively what is meant by "near" will be discussed later in the paper). The VDF is a fundamental kinetic property of the gas or plasma that fully describes the state of the target species on the spatial and temporal scales accessible by the measurement—it can be used to calculate bulk fluid properties such as the mean velocity and temperature.

For common EP propellants such as xenon and krypton, straightforward laser setups cannot produce individual photons capable of inducing atomic transitions out of the ground state, so excited states must be targeted. Often the target is a metastable state, which cannot spontaneously decay according to the electric dipole selection rules and therefore tends to have relatively high density. The ratio of the population density of a given excited state to the ground state density depends in a complex way on the local free electron properties [30], so single-photon LIF cannot easily be used to measure the overall atom or ion density, and applications are usually limited to VDF measurements and evaluation of higher moments of the distribution. However, pulsed ultraviolet (UV) lasers can produce sufficiently intense beams at 200–300 nm to induce two-photon absorption processes with non-negligible probability, enabling direct density measurements of neutral xenon and krypton [31] by integrating over the VDF.

This paper presents recommended practices for applications of LIF techniques in electric propulsion testing. These diagnostics require moderately complex experimental setups and sophisticated data analysis methods to extract the fluorescence signal from the more intense background light emission, ensure adequate spatial and/or temporal resolution for a given application, and avoid unphysical distortions in the interpretation of the data. The first part of the paper discusses single-photon absorption LIF: topics covered include target transitions for various propellants, test equipment selection and setup, data analysis methods and uncertainty quantification, line profile broadening mechanisms, and high-speed measurement techniques. The majority of the discussion focuses on applications of LIF to Hall thruster testing, but methods for characterizing other EP devices are also described. The second part of the paper outlines best practices for two-photon absorption LIF (TALIF), covering motivation and challenges unique to EP discharges, TALIF schemes, rate equations and saturation, experimental setups, data analysis and uncertainty quantification, and the outlook for future innovations.

2 Atomic Transitions for Single-Photon LIF

Species	$\lambda_{exc.}$(nm)	$\lambda_{fluo.}$(nm)	Initial State	Excited State	Final State	Ref.
Xe II	834.953	542.063	$5s^2 5p^4 (^3\mathrm{P}_2) 5d\ ^2[4]_{7/2}$	$5s^2 5p^4 (^3\mathrm{P}_2) 6p\ ^2[3]^{\mathrm{o}}_{5/2}$	$5s^2 5p^4 (^3\mathrm{P}_2) 6s\ ^2[2]_{3/2}$	[2]
Xe II	605.280	529.366	$5s^2 5p^4 (^3\mathrm{P}_2) 5d\ ^2[3]_{7/2}$	$5s^2 5p^4 (^3\mathrm{P}_2) 6p\ ^2[2]^{\mathrm{o}}_{5/2}$	$5s^2 5p^4 (^3\mathrm{P}_2) 6s\ ^2[2]_{5/2}$	[32]
Xe I	834.910	473.544	$5s^2 5p^5 (^2\mathrm{P^o}_{1/2}) 6s\ ^2[1/2]^{\mathrm{o}}_1$	$5s^2 5p^5 (^2\mathrm{P^o}_{1/2}) 6p\ ^2[3/2]_2$	$5s^2 5p^5 (^2\mathrm{P^o}_{1/2}) 6s\ ^2[3/2]^{\mathrm{o}}_1$	[33]
Xe I	823.388	823.388	$5s^2 5p^5 (^2\mathrm{P^o}_{3/2}) 6s\ ^2[3/2]^{\mathrm{o}}_2$	$5s^2 5p^5 (^2\mathrm{P^o}_{3/2}) 6p\ ^2[3/2]_2$	$5s^2 5p^5 (^2\mathrm{P^o}_{3/2}) 6s\ ^2[3/2]^{\mathrm{o}}_2$	[32]
Kr II	729.181	474.029	$4s^2 4p^4 (^3\mathrm{P}) 4d\ ^4\mathrm{D}_{7/2}$	$4s^2 4p^4 (^3\mathrm{P}) 5p\ ^4\mathrm{P^o}_{5/2}$	$4s^2 4p^4 (^3\mathrm{P}) 5s\ ^4\mathrm{P}_{5/2}$	[34]
Kr I	760.362	760.362	$4s^2 4p^5 (^2\mathrm{P^o}_{3/2}) 5s\ ^2[3/2]^{\mathrm{o}}_2$	$4s^2 4p^5 (^2\mathrm{P^o}_{3/2}) 5p\ ^2[3/2]_2$	$4s^2 4p^5 (^2\mathrm{P^o}_{3/2}) 5s\ ^2[3/2]^{\mathrm{o}}_2$	[34]
I II	696.069	516.264	$5s^2 5p^3 (^4\mathrm{S^o}) 5d\ ^5\mathrm{D^o}_4$	$5s^2 5p^3 (^4\mathrm{S^o}) 6p\ ^5\mathrm{P}_3$	$5s^2 5p^3 (^4\mathrm{S^o}) 6s\ ^5\mathrm{S^o}_2$	[35]
I I	906.079	906.079	$5s^2 5p^4 (^3\mathrm{P}_2) 6s\ ^2[2]_{5/2}$	$5s^2 5p^4 (^3\mathrm{P}_2) 6p\ ^2[3]^{\mathrm{o}}_{7/2}$	$5s^2 5p^4 (^3\mathrm{P}_2) 6s\ ^2[2]_{5/2}$	[36]
Cs I	852.346	852.346	$5p^6 6s\ ^2\mathrm{S}_{1/2}$	$5p^6 6p\ ^2\mathrm{P^o}_{3/2}$	$5p^6 6s\ ^2\mathrm{S}_{1/2}$	[29]

Table 1: LIF schemes that have been studied for electric thrusters. The listed excitation and fluorescence transition wavelengths are evaluated in vacuum.

This section describes the laser absorption and fluorescence emission atomic transitions recommended for studies of common EP propellants. A summary is provided in Table 1. The wavelengths reported here are all evaluated in vacuum. Some references instead report the wavelength in air; in cases for which the vacuum wavelength has not been previously reported to at least 1 pm precision, it was derived by multiplying the observed wavelength in air reported in the NIST Atomic Spectra Database (ASD) [37] by the index of refraction for air from Ref. 38, since NIST used the formula in this paper to derive their reported wavelengths in air. Because uncertainties in the last digit of the excitation wavelength values can correspond to uncertainties of hundreds of meters per second in particle velocities derived from the Doppler shift, for LIF applications in which absolute velocity accuracy is critical, it is recommended to use a stationary reference to measure the wavelength corresponding to zero velocity.

The atomic states are labeled using the spectroscopic configuration and term notation for each element that is used in the NIST ASD. Unless otherwise specified, the standard term notation for LS (Russell-Saunders) coupling ($^{2S+1}L_J$) is used, where S, L, and J are the overall spin, orbital, and total angular momentum quantum numbers for the valence electrons and the core angular momentum term is shown in parentheses. For neutral and singly-ionized xenon (Xe I and Xe II), neutral krypton (Kr I), and neutral iodine (I I) Racah notation is used, in which the number in square brackets is the sum of the core electrons' total angular momentum and the orbital angular momentum of the excited electron.

2.1 Xenon

LIF studies in Hall thrusters operating on xenon have most commonly targeted the singly-ionized (Xe II) transition at 834.953 nm, which is conveniently accessible with a tunable diode laser, with fluorescence emission detected at 542.063 nm [2]. A visible excitation transition at 605.280 nm has also been used, with fluorescence detected at 529.366 nm [32]. Both of these laser absorption transitions have metastable lower levels, leading to relatively high population density of the target state.

For neutral xenon (Xe I), the most common LIF schemes use excitation at 834.910 nm, with fluorescence detected at 473.544 nm [33], or excitation at 823.388 nm, with fluorescence detected at the same wavelength [32]. The latter scheme has the advantage of a metastable lower level, leading to higher signal intensity, but having an identical detection wavelength (a "resonant" scheme) causes the measurement to be susceptible to distortion by laser photons scattered into the detector.

2.2 Krypton

For neutral krypton, candidate transitions for LIF occur at 810.658 nm and 760.362 nm [34]. It is the second of these which has received more attention in spectroscopic data, and the spin splitting and stable isotopic shifts are known [39, 40]. The lower state of the 760.362-nm transition $\left(\left({}^2\mathrm{P^o}_{3/2}\right)5s\ {}^2[3/2]^{\mathrm{o}}_2\right)$ has a long 40 s lifetime, and the upper state $\left(\left({}^2\mathrm{P^o}_{3/2}\right)5p\ {}^2[3/2]_2\right)$ primarily decays resonantly with a 77% branching ratio [37]. Notably, the inverse emission process to this absorption line also represents the fluorescence for some TALIF schemes, described further in Sec. 7.3. To date, little work has been performed on single-photon laser-induced fluorescence for neutral krypton, and TALIF instead has been used to investigate the neutral densities and velocities by tagging methods. More work to investigate these transitions is needed.

In contrast, single-photon LIF for singly ionized krypton has been successfully used in Hall thrusters as an ion velocity diagnostic. While Scharfe identified several suitable transitions [41], the near-IR transition from state $\left({}^3\mathrm{P}\right)4d\ {}^4\mathrm{D}_{7/2}$ to state $\left({}^3\mathrm{P}\right)5p\ {}^4\mathrm{P^o}_{5/2}$ occurring at 729.181 nm has received the most study [34, 42–44]. For this transition, the upper state decays with an 80% branching ratio to the $\left({}^3\mathrm{P}\right)5s\ {}^4\mathrm{P}_{5/2}$ state, emitting a 474.029-nm photon. The upper state lifetime is approximately 13 ns for this decay path, enabling a high upper limit on time resolution [37].

2.3 Argon

Argon is of growing interest for electric propulsion due to its high atmospheric abundance and low cost, which in some cases may outweigh disadvantages in ionization efficiency, thrust per ion, and storage volume compared to xenon and krypton. However, very little argon neutral or ion LIF work has been performed with electric propulsion systems. The lowest excited level of neutral Ar is 11.55 eV above the $3p^6\ {}^1S_0$ ground state and is designated $\left({}^2\mathrm{P}^o_{3/2}\right)4s\ {}^2[3/2]^o_2$; the 811.531 nm transition from this metastable level to the $\left({}^2\mathrm{P}^o_{3/2}\right)4p\ {}^2[5/2]_3$ state was used for laser absorption spectroscopy in an arcjet [45] and would also be a good candidate for LIF. An earlier argon arcject study [46] employed LIF to excite the 727.3 nm transition from the $\left({}^2\mathrm{P}^o_{3/2}\right)4s\ {}^2[3/2]^o_1$ level of argon to the $\left({}^2\mathrm{P}^o_{1/2}\right)4p\ {}^2[1/2]_1$ state, with fluorescence detected at 826.5 nm, 772.4 nm, and 727.3 nm; use of a non-metastable target state may only be feasible in plasma sources with relatively high plasma and gas density. Another possible target is the transition from the $\left({}^2\mathrm{P}^o_{3/2}\right)4s\ {}^2[3/2]^o_2$ metastable state to the $\left({}^2\mathrm{P}^o_{1/2}\right)4p\ {}^2[3/2]_1$ state at 714.7 nm [46]; fluorescence could be detected at 714.704 nm, 794.818 nm, or 852.144 nm.

For Ar II, several LIF schemes have been explored [47, 48]. A partial energy level diagram and table depicting several of these are available [47].

2.4 Iodine

Laser absorption spectroscopy for neutral iodine has been demonstrated for the transition between the lower $\left({}^3P_2\right)6s\ {}^2[2]_{5/2}$ level and the upper $\left({}^3P_2\right)6p\ {}^2[3]^o_{7/2}$ level at 906.079 nm [36]. This transition should be suitable for use in a resonant LIF scheme, with fluorescence radiation collected at the laser excitation wavelength.

A proposed scheme for singly-ionized iodine was first investigated by Hargus et al. using emission spectroscopy [35]. The metastable $\left({}^4S_0\right)5d\ {}^5D^o_4$ state is excited to the $\left({}^4S_0\right)6p\ {}^5P_3$ state by absorption of a 696.0694 nm photon. The upper state relaxes to the $\left({}^4S_0\right)6s\ {}^5S^o_2$ state, emitting a fluorescence photon at 516.264 nm. Detailed information about the transition can be found in [49, 50].

2.5 Cesium

Measurements of the ground-state Cs atom velocity vector and density by resonant LIF in the plume of a cesium-fed Field Emission Electric Propulsion (FEEP) thruster were made using the so-called D2 transition of cesium in the near-infrared (IR) [29]. The ground-state $6s\,{}^2S_{1/2}$ state is excited to the $6p\,{}^2P^o_{3/2}$ state by absorption of a 852.346 nm photon. The fluorescence radiation due to excitation is captured at the same wavelength.

2.6 Molybdenum and Other Metals

The grids that extract ionized propellant in ion engines have been commonly made of molybdenum. It is possible to use single-photon LIF with a continuous wave (CW) laser to probe the ground state of neutral Mo and measure the density of eroding material in real time. Due to the very low density that is produced during engine operation, typically much less than 10^{15} m^{-3}, the TALIF technique or other pulsed laser approach is not sufficiently sensitive. For single-photon LIF on Mo, near ultraviolet light is generated with a dye laser using a suitable near-uv dye such as Exalite 392E, or by frequency-doubling a high-resolution tunable dye or Ti:Sa laser, either in-cavity or with an external resonator [24].

The first studies of sputtered molybdenum atoms produced in an operating ion engine environment[51, 52] utilized the transition at 390.2953 nm from the $\left({}^6S\right) 5s\; a\,{}^7S_3$ ground state to the excited state with electron configuration $\left({}^6S\right) 5p\; z\,{}^7P^{\mathrm{o}}_2$. Resonant fluorescence was detected at the same wavelength. For these early studies the laser frequency was fixed at the peak of the Doppler profile, because the laser linewidth was comparable to the width of the profile. Later work was done with single frequency (very narrow linewidth) dye and Ti:Sa laser sources utilizing either the same transition or others, and the laser frequency was scanned to record the line profile of the transition. Integration over the entire profile provides a good measure of relative density, although note that the existence in Mo of many energy levels within a few eV of the ground state may mean that atoms in the ground state make up a smaller percentage of the total density than they would in noble gases. Some of these studies used a stronger transition deeper in the UV (313.2594 nm), from the ground state to the $\left({}^6D\right) 5p\; y\,{}^7P^{\mathrm{o}}_4$ state. All $y\,{}^7P^{\mathrm{o}}$ and $z\,{}^7P^{\mathrm{o}}$ levels fluoresce strongly, with lifetime less than 20 ns. Due to the brief excited state lifetimes, and the low densities of plume species, collisional quenching has no effect on the observed molybdenum LIF signal.

While molybdenum has been studied primarily in connection with gridded ion engines, its detection via LIF has potential application to other devices such as Hall thrusters as well. For example, a small molybdenum (or other suitable material) patch introduced on the downstream surface of a pole piece could be used to monitor the erosion rate.

LIF in the near UV is applicable to other metal atoms such as titanium, tungsten and tantalum [53, 54] which are also utilized as electric propulsion materials. To provide absolute density calibration a small sputter target can be inserted at normal incidence to the ion beam, and the ratio of target LIF signal to plume LIF signal can be obtained. From the ion energy, flux, known sputter yield and estimated average velocity of the sputtered atoms, their absolute density near the target can be calculated. Another calibration approach has also been utilized. The absolute deposition rate recorded by a quartz crystal microbalance (QCM) system, swept at constant distance from the extraction grids, provided absolute molybdenum atom flux in the far-field at high angles. Together with a model constructed to relate density and flux at the grid with the measured far-field flux at the QCM, an estimate for molybdenum density at the grid face was obtained.

2.7 Tracer Gases

Since many tunable lasers used for LIF can access a limited wavelength range (e.g., 10s of nm), implementing the diagnostic for multiple propellants may require costly investments in dedicated laser equipment for each target transition. Recent work by Simmonds et al. [55] demonstrated the feasibility of seeding a krypton Hall thruster discharge with $\leq$ 1% xenon to enable LIF measurements at 834.953 nm, from which the spatially resolved electric field could be derived [56]. Even with this low xenon concentration that did not significantly change the discharge telemetry, high signal-to-noise ratio (SNR) was demonstrated because the krypton spontaneous emission spectrum contains no strong lines near the 542.066 nm xenon fluorescence wavelength; xenon tracers are expected to be applicable in other common propellants for the same reason. The method remains to be validated through direct comparisons between LIF measurements on the main propellant species and on the tracer gas under the same operating conditions.

3 Hardware Setup for Single-Photon LIF

3.1 Tunable Laser Technologies

Historically, both ring-dye lasers and Ti:Sapphire lasers were used for LIF investigations of xenon ions in the plumes of electric propulsion devices [5, 57]. These types of lasers are able to be scanned in a precise band of wavelengths as well as tuned widely over several hundred nanometers. However, most modern single-photon LIF schemes use tunable diode lasers due to their comparative simplicity of operation and lower cost. These diodes typically emit light in the red to near-IR bands, although some examples of blue and near-UV diodes exist [34]. They also provide less flexibility, since a given diode is constrained to a narrower range of possible wavelengths (typically around 20 nm). Today, tunable diode lasers can be purchased with highly customizable center wavelengths, and when combined with tapered amplifiers they can commonly reach CW powers of several hundred milliwatts. These units are extremely temperature sensitive but generally come with internal Peltier coolers or other thermal control hardware. In such systems, tuning the cavity temperature set point can be a useful strategy for mitigating mode hops and making large tuning jumps in the laser wavelength [58].

3.2 Laser Safety

Typical single-photon LIF setups use CW laser sources with power levels ranging from 10 mW to > 1 W. Lasers with power ≥ 5 mW and < 500 mW are categorized as Class 3B according to the American National Standards Institute (ANSI) classification system [59], indicating that they are hazardous to the eyes, while lasers with power ≥ 500 mW are categorized as Class 4, identifying an additional hazard of skin burns from short-duration exposure. High power lasers may also pose high voltage, chemical, and/or fire hazards, depending on the type of laser. Exposure of the eyes to high power lasers is of particular concern because the concentrated energy can cause retinal damage and associated vision degradation that is often irreversible. All experimental setups utilizing Class 3B and 4 lasers should be subject to review by an appropriately trained safety officer at the hosting institution prior to operation. The review should include a laser hazard analysis in which the minimum required optical density of protective eyewear is calculated, along with the nominal hazard zones (distance from the source) for the direct output of the laser, the beam when focused by a lens, the beam when exiting an optical fiber, and the beam following diffuse reflection. Several software tools that can complete this analysis are commercially available.

Common methods for hazard mitigation include safety glasses designed to have adequate attenuation (optical density) over the laser's wavelength range, light-proof barriers such as walls or curtains surrounding the area where the beam is propagating through free space, warning signs and barricades to prevent accidental access to the laser area by unprepared individuals, and interlocks on the laser output. Beam paths should be terminated in dedicated beam dumps designed to handle the incident energy, unless the optical configuration naturally defocuses the beam to a safe intensity before it reaches any surfaces. Injuries most commonly occur during alignment operations, when personnel are more likely to enter the beam path or look toward the source. Whenever possible, alignment should be carried out with low-power (< 5 mW) visible lasers, or if the high-power LIF laser must be used, neutral density filters should be inserted in the beam path for attenuation. Operators should be aware of the possibility of unexpected reflections (for example, off of misaligned optics or jewelry worn by the operator), taking particular care in cases where the laser wavelength is in the ultraviolet or infrared and the beam is therefore invisible to the naked eye. Phosphorescent laser detector cards and UV/IR sensitive cameras are often used to maintain operator awareness of the path followed by an invisible laser beam and mitigate risks associated with eye-based alignment techniques.

3.3 Optical Components and Layout

All LIF optical layouts consistent of an injection scheme to transmit and focus the laser light from the head to a targeted volume in the plasma and a collection scheme to convey fluoresced light from the volume to the detection system. The common goals for the combination of these elements are to 1) maximize laser power in the plasma to increase signal (while maintaining an acceptably low level of saturation—see Sec. 4.3), 2) minimize the detection volume to increase spatial resolution ($\lesssim 1$ mm spot size is typical), and 3) maximize the amount of fluoresced light return to the detector for increasing signal to noise. We provide in

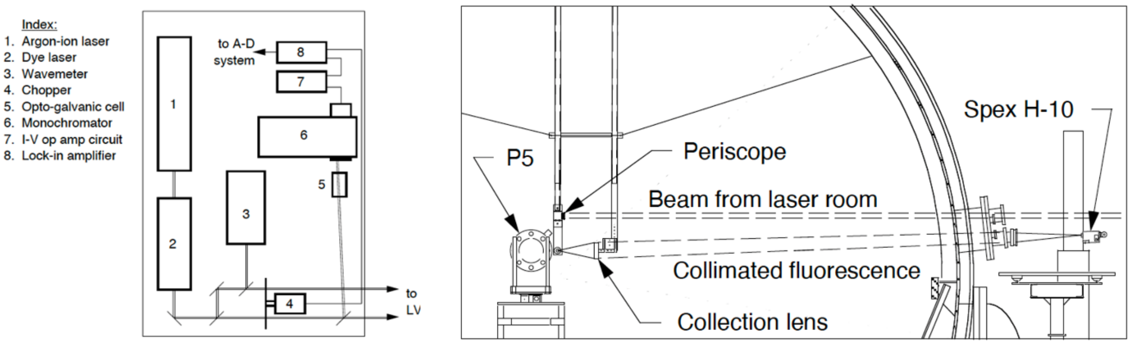

Figure 1: Free space coupled laser induced fluorescence configuration from Ref. 60 (reproduced with permission). Left: optical table setup with key labeled components. The laser light is coupled from the table via free space to the chamber ("LVTF"). Right: beam path through the side of vacuum chamber wall where "P5" denotes a Hall thruster test article and "Spex H-10" is a spectrometer.

the following an overview of best practices for the injection and coupling schemes for the purpose of achieving these common goals.

3.3.1 Free-Space Coupled Setups

Injection schemes for LIF systems fall into two categories: free space, in which the light from the laser head is re-directed by a series of mirrors and lenses through space into the plasma, and fiber-coupled, in which the laser light is coupled into a fiber which then conveys the light to a separate focusing optic adjacent to the plasma. Figure 1 shows an example of an air-coupled scheme for an LIF system taken from Ref. 60. Depending on the degree of collimation from the laser head, this system does not in principle require a focusing optic to achieve a small spot size.

The free space technique has three major advantages. The first is that it can maximize the amount of laser light sourced from the head into the plasma. Unlike fiber-based systems where there is inherent loss at the input coupler, at transitions between fibers, and within the cables, this system has minimal attenuation. The second major advantage is that alignment of the injected light into the plasma can be adjusted by manipulating the optical components external to the vacuum setup. This is a major benefit over fiber-coupled systems that require specialized in-situ motion stages in the vacuum chamber that are prone to failure. The third advantage is that the light polarization from the head (typically linear) is preserved. This can be a critical consideration where effects like Zeeman splitting can be avoided with a judicious choice of polarization and alignment with respect to the test article's magnetic field.

There are two key challenges with the free space scheme. First, the approach requires direct optical access from outside the vacuum system to the plasma of interest. This can prohibit interrogating certain velocity directions or region of the plasma system. The second difficulty is that, depending on the size of the chamber, the injection scheme can be meters long from the exterior to the plasma of interest. This can make it challenging to identify optical components that maintain small beam size and alignment on this scale.

The key consideration in the implementation of free space system is to have a fine-axis motor control for the beam path into the chamber. This system in principle should have three degrees of freedom to allow for alignment and adjustment during testing.

3.3.2 Fiber Coupled Setups

Figure 2 shows an example of a fiber-coupled scheme for an LIF system taken from Ref. 10. The system consists of one or more fiber optic cables that are located near the laser head. The laser beam is coupled from the laser head via a fiber-coupler, an optic that focuses the collimated beam into the narrow aperture of the fiber. The fiber is then inserted into the vacuum chamber either via a vacuum coupler or a potted flange. Inside the chamber, the fiber is mated to an optical scheme that focuses the light from the fiber aperture into the volume of interest in the plasma. Optical bench configurations for LIF configurations (as

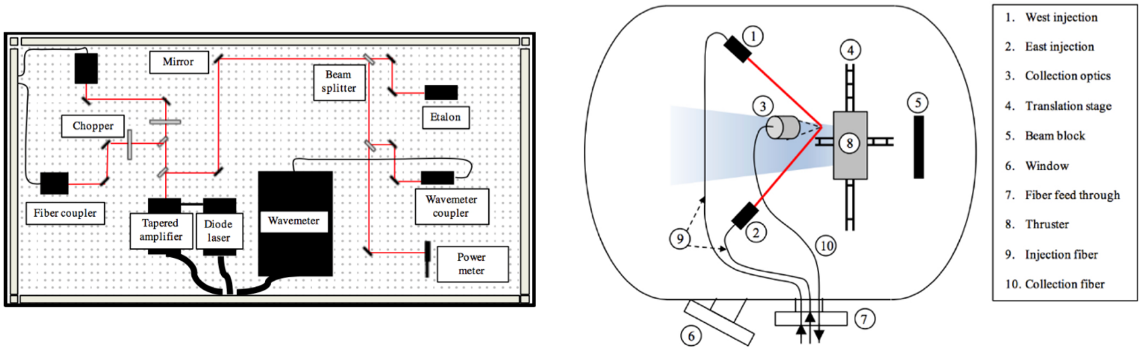

Figure 2: Optical configuration for a fiber-coupled laser induced fluorescence system from Ref. 10 (reproduced with permission). Left: Optical table showing key components and the fiber couplers. Two fiber couplers are employed in this case to allow for simultaneous interrogation of two directions. Right: Layout in vacuum chamber for Hall thruster testing.

shown in Fig. 2) share the common need to provide a space for coupling the laser light into the plasma, facilitating beam diagnostics, and in some cases, providing a return path for the collection optics.

The major advantage of the fiber-based system is ease of placement for the injection scheme. The proximity of the injection optics to the plasma source allows for increased flexibility for the injection orientation with respect to test articles.

The major challenge with fiber-coupling is the loss from attenuation and beam quality that can result from transiting the fiber. Attenuation in power greater than 50% is not unusual in a typical and unoptimized setup. This reduction in power stems from difficulty in focusing the laser head light into the fiber, losses in coupling across the vacuum chamber interface, and losses from the injection optics inside the chamber. There are two types of fibers that can be adopted to address these challenges. Single mode fibers have smaller cores ($< 10\ \mu$m diameter) and as such allow for smaller achievable spot-size (and thus spatial resolution) when focused into the plasma. These cores also maintain higher beam quality. The primary disadvantage is that it is more difficult to couple the laser head light into the smaller core, representing a major loss for power injected into the plasma, which adversely impacts signal. As an alternative, multimode fibers typically have larger core sizes ($\geq 50\ \mu$m), allowing for a higher fraction of light coupled into the fiber. Multimode fibers, however, cannot achieve the same focused size as single mode and can suffer from beam quality aberrations. The choice between fiber modes is ultimately dictated by the needs of the experimenter, trading signal strength versus spot size and beam quality.

A key challenge with a fiber-coupled scheme is adopting a repeatable strategy for focusing light into the fiber. There are couplers commercially available to help facilitate this. In the selection of these systems, careful consideration must be given to the wavelength, beam width from the laser head, and the numerical aperture and diameter of the target fiber. It is recommended to procure fiber coupler stages with a minimum of three axes of movement to allow for maximized laser coupling. To facilitate the alignment process with the coupler, it can be helpful to "butt couple" a visible laser pen into the vacuum side of the optic that runs in reverse of the light from the laser head. This will produce a visible beam emerging from the fiber-coupler back toward the laser head. To achieve rough initial alignment, the laser head beam and this beam can be "beam walked" (i.e., ensuring that the two beams are coincident all along the path by adjusting the coupler stages and steering mirrors, if present).

Another key challenge is to reduce losses in the beam as it is coupled into the vacuum chamber. The ideal configuration is a fiber that is potted through a vacuum flange in such a way that the core is never broken. These configurations, however, are typically custom and expensive. As an alternative, off the shelf fiber couplers can be used that consist of a threaded pass-through with a lens. This results in a butt couple between the air and vacuum side optics. This approach has higher loss but is less expensive and allows for the simplified replacement of damaged cables.

Misalignments in the fiber resulting from changes in the orientation of the fiber with respect to the coupling element can yield major losses in performance. "Keyed" connectors such as FC/PC thus are recommended over SMA. Similarly, fiber ends should be periodically checked for cleanliness as even small

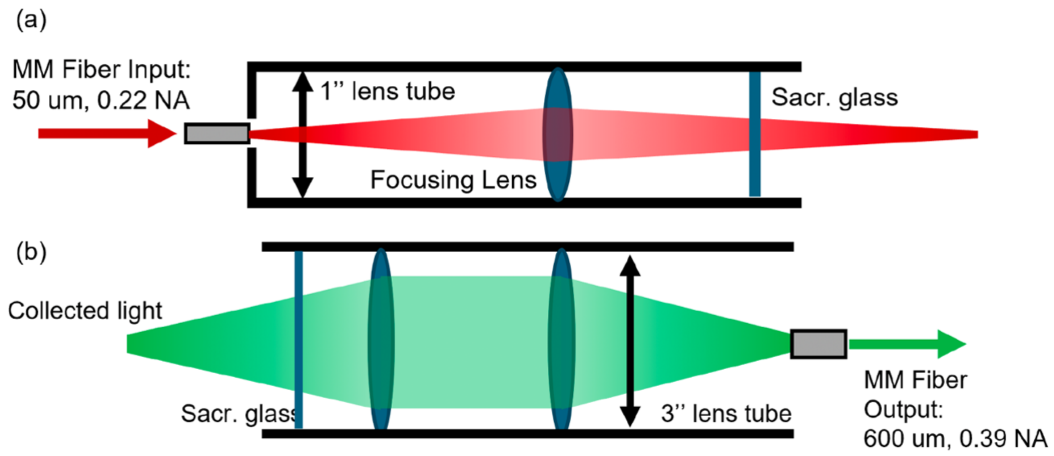

Figure 3: a) Injection optic and (b) collection optic for a fiber-coupled LIF scheme. Figure from Ref. 61 (reproduced with permission).

dust particles can dramatically attenuate the beam across coupling junctions.

It is highly recommended to procure fibers that have stainless-steel jacketing. This is to avoid incidental damage to the fibers when arranging them in the experimental configuration. With respect to core size and configuration, both single mode (< 10 μm) and multimode (≥ 50 μm) fibers have commonly been employed in electric propulsion applications. Care must be taken to ensure that the power density into the fiber will not exceed the damage threshold. This is particularly a concern for the fiber aperture where overfocusing of the fiber-coupler can yield a smaller effective beam size into the optic at the interface.

The role of the injection optic is to couple the light emerging from the fiber on the vacuum side of the system into the plasma volume. This is typically achieved by focusing the emerging light, which has a cone angle dictated by the numerical aperture of the fiber, into a beam waist coincident with the point of interest. Figure 3(a) shows an example of such a configuration from Ref. citenumRobertsthesis2025 in which a single lens is employed to focus the light to a point to a beam waist of 1 mm at a distance over a meter away from the optics. The experimenter can employ the linearized version of the lens equation to determine the approximate location of the fiber with respect to the lens in order to focus the light to a desired location and spot size. The aperture must be chosen to encompass the entire beam at this idealized placement. As can be seen in Fig. 3(a), it is common to place a clear window downstream of the focusing lens, which serves as shield to the plasma. This is necessary as the optics are in the chamber and exposed to ion bombardment. The overall optic assembly must be mounted on one or more translation stages or rotation stages to allow for in-situ fine alignment to correct for thermal drifts during chamber pumpdown and plasma operation (Fig. 2).

Figure 3(b) shows an example of a typical collection optic configuration. It is nearly a uniform practice to rely on fiber coupling for this component of the system. In this case, light is fluoresced from the plasma along the path of the injection beam. The collection optic is positioned to intercept light along a solid angle oriented toward the narrowest point of the injection beam. This solid angle is dictated by the diameter of the focusing lens of the collection light and its focal length. The emerging light is collimated and then passed to another focusing lens that couples this light into a large-diameter > 500 μm typically) multimode fiber optic. The fiber then passes through the chamber wall and is coupled to the detector. The two-lens setup can be surrounded by a darkened tube to absorb stray light coupled into the system and increase signal to noise. Loss of light along the fiber transmision path from the collection optic to the detector is less of a concern than losses of laser power along the injection path since the desired fluorescence signal and the background plasma emission signal will be attenuated equally.

The goals of collection optic design are to ensure maximum signal is coupled out of the plasma while maintaining the desired spatial resolution. This requires maximizing solid angle to the system, which requires in principle a combination of proximity to the fluoresced volume in the plasma (shorter focal length) as well as larger optic aperture. However, there are limitations to this approach because lenses with very low f-number (i.e., large diameter and short focal length) tend to have larger aberrations, which undesirably increases the size of the measurement volume. Regardless if light is maximized into the collimating optic, there is still a potential choke point at the fiber itself, which is dictated by its numerical aperture (angle of acceptance) and diameter. The experimenter needs to balance optic size, how feasible it is to actually place the optic near the plasma without perturbing the system, and the size of the fiber. This trade in large part can be evaluated through a consideration of the entendu in the system, which is a preserved factor for the system that dictates the magnitude of light transmitted.

Focusing performance of each optical assembly can be improved by the use of achromatic lenses, which in addition to having nearly wavelength-independent focal length also have significantly reduced aberrations compared to plano-convex spherical lenses.

3.4 Laser Wavelength and Power Metering

In order to accurately calculate the neutral or ion velocity distribution from the Doppler-shifted absorption line profile (Eq. 1), the tunable laser wavelength must be precisely known throughout the wavelength scan, and the laser power should ideally be held constant as the wavelength is varied. In typical LIF setups, a fraction of the laser power is sampled from the main beam by beam splitters (for example, 1%/99% or 10%/90%) and diverted to beam diagnostics. Commercial wavelength meters are available with fast ($\gg 1$ Hz) response times and absolute optical frequency accuracy on the order of 50 MHz (corresponding to wavelength uncertainty of ~ 0.1 pm at $\lambda = 835$ nm); these may have an internal wavelength calibration source or require an external calibration input [31]. Some setups alternately use a Fabry-Perot etalon for wavelength monitoring [62].

Real-time power monitoring of relative laser power variations may be accomplished with a commercially available high-speed photodiode. To correct for modest power drift ($< 20\%$) when calculating the IVDF, it is usually acceptable to divide the LIF signal at each laser wavelength by the measured instantaneous power. Since LIF measurements on electric thrusters are typically carried out with the atomic transition somewhat saturated (see Sec. 4.3), the assumption of signal strength depending linearly on power is an approximation, and the limitations of this approach must be recognized. Using the laser or laser amplifier's built-in power locking feature, without real time power monitoring, may be sufficient in some cases, but the power stability should be verified by an independent beam diagnostic during the initial test setup. Convenient handheld laser power meters are available for absolute measurements of laser power at a given location, which is useful for ensuring efficient power coupling through the optical train to the measurement volume (see Sec. 3.3) and for evaluating the relationship between the incident laser intensity and the saturation intensity (Sec. 4.3). In some setups, the relative laser power as a function of wavelength may be measurably different at the interrogation volume compared to at the power sampling location on the optical table, for example due to slight movement of the optical cavity that affects coupling of the light into the optical fiber leading to the chamber.

3.5 Fluorescence Wavelength Filtering and Photon Detection

Since thrusters produce energetic plasma and the interrogation volume for LIF is typically a small fraction of the overall plasma volume, the collection lens of an LIF setup often collects much more light from spontaneous emission than from laser-induced fluorescence. To improve the SNR, it is often necessary to perform wavelength filtering, and some kind of monochromator is typically used. Generally, monochromators with longer effective light path are better at controlling the precision of the band of wavelengths that can pass through in exchange for taking up more physical space. Another important factor is the ability of the monochromator to suppress stray light. Given the large amount of natural fluorescence collected by a typical LIF setup, even 0.01% of the stray light can have a higher magnitude than the LIF signal.

To detect the signal that passes through, a photon detector is typically mounted to the output of the monochromator. Common photon detectors include, in order of increasing amplification factor, fast-acting photodiodes, photo-multiplier tubes (PMTs), and photon counters. For most time-averaged LIF applications, a PMT provides a good amount of signal with acceptable noise and is fast enough to respond to acousto-optic and electro-optic beam modulators (i.e., beam choppers, see Sec. 3.6). Some applications with high photon collection rates and slow chopping rate ($\sim$ kHz) could enable the use of photodiode. In applications with very low photon collection rates, a photon counter may be needed. PMTs output a current that is typically converted to a voltage by an active transimpedance amplifier [20] or by directly reading the voltage drop across a load resistor [15]. If the detector or downstream lock-in amplifier is saturating due to excessive background light signal, the gain of the amplifier may be reduced, or a neutral density filter can be used to reduce the amount of light entering the detector.

An alternate approach for wavelength filtering, which has the advantage of higher optical throughput than a monochromator in a far smaller package, is to mount an optical bandpass filter at the input to the detector [63]. The achievable spectral resolution is lower than that of a mid-sized monochromator, but moderately priced filters now exist with ~ 2 nm full width at half maximum (FWHM) of the transmission band, with customizable center wavelength.

3.6 Laser Modulation and Lock-in Amplifiers

The continuous output of a diode, dye or Ti:Sa laser is typically passed through a mechanical "chopper", a device that periodically blocks the beam at frequencies up to a ~ 10 kHz. Due to this the fluorescence signal received at the photon detector is amplitude modulated. To demodulate the oscillating detector output it is typically fed into a lock-in amplifier (for detectors such as PMTs that act as a current source, current-to-voltage conversion is first carried out using a transimpedance amplifier or a resistor), which uses the chopper frequency as a reference to perform phase-sensitive detection. Phase-sensitive detection essentially involves multiplying the modulated data by a sine wave with frequency and phase matching the modulation, then low-pass filtering; for details refer to Ref. 64. This process greatly suppresses the noise at all other frequencies (primarily from background plasma light) and increases the SNR. Generally the lock-in amplifier should be operated in a single-phase mode (often called "X mode"), rather than "R mode" in which two demodulated signals constructed from reference waveforms 90 degrees out of phase from one another are combined in quadrature, because "R mode" rectifies noise at the chopping frequency such that it doesn't average to 0 in the final result. While a single chopping frequency can be used, if the laser beam is split into two or more legs they can be chopped at different frequencies and use separate lock-in amplifiers, allowing for simultaneous measurement of VDFs along multiple axes with a single collection optic and detector. When two or more probe beams are utilized, one may be transverse to the thruster axis of symmetry and the other longitudinal, or they may form an arbitrary angle. Geometrical relationships for each situation have been previously analyzed [46, 65].

For high-speed LIF measurements, the modulation frequency achievable with a mechanical chopper is insufficient, in which case an acousto-optic modulator (AOM) [15, 66] or electro-optic modulator (EOM) [20] may be used to modulate the laser beam at frequencies exceeding 1 MHz. Chopping at high frequency may also be useful for improving SNR in time-averaged LIF measurements if the power spectrum of background light emission from the plasma peaks at lower frequencies [67]. If a lock-in amplifier capable of locking to MHz frequencies is not available, the modulated data may be digitized at high-speed so that phase-sensitive detection can be performed numerically in post-processing [15, 66].

AOMs [68] work via Bragg diffraction, in which a large-amplitude acoustic wave (frequency ~ 100 MHz) driven through an optically transparent material causes diffraction of some fraction of the laser photons passing through the material. In a typical LIF setup, the directly transmitted beam path is terminated in a beam block, while the first-order diffracted path (which exits the AOM with an angular deflection of $\sim 1^\circ$ compared to the transmitted path) is directed to the fiber coupler or window leading to the vacuum chamber. The RF amplifier driving the acoustic wave is modulated either digitally (on/off) or sinusoidally to modulate the laser intensity that reaches the LIF measurement volume along the diffracted path. The achievable chopping frequency is limited by the acoustic wave propagation time across the laser beam within the AOM, so it can be improved if the beam is tightly focused, but this requirement must be balanced against the degradation in diffraction efficiency (and corresponding decrease in laser power delivered to the measurement volume) if the laser beam divergence is too large.

3.7 Motion Stages

One of the advantages of LIF is the ability to achieve fine spatial resolution, determined essentially by the size of the overlap between the injected laser beam and the focal cone of the collection optic. With typical focusing and alignment methods the diameter of this region can easily be reduced to ~ 1 mm, less than the size of plasma structures of interest such as the acceleration region of Hall thrusters [69, 70]. Given this small spatial extent of the measurement, the value of LIF lies in its ability to provide neutral or ion flow measurements at multiple locations.

It is difficult (though not impossible) to translate both the injected beam and collection line of sight relative to the plume while maintaining a precise tolerance on the alignment. For this reason, a common practice is to place the plasma source itself on positioning stages for relative motion between the interrogation volume and the thruster. The thruster's propellant lines and electrical harness must be properly designed to allow full range of motion without leaks or snags. Care must be taken to ensure that the precision and repeatability of the motion system does not cause any systematic positioning errors or loss of laser-limited spatial resolution. In practice, motion stages with lead screws can readily reach below 1 mm of repeatability [71], depending on the choice of lead screw pitch, and magnetic linear encoders can monitor the stage location relative to a reference position with accuracy better than 0.1 mm. When encoders are integrated into the motion stages, uncertainty in the LIF measurement position is typically dominated by alignment uncertainty (see Sec. 3.8). Tensioned string potentiometers can also be used for monitoring the stage positions, but they have larger uncertainties (0.5–1 mm in optimized setups) and are sensitive to electrical drifts.

For some applications of LIF to EP, a single stage for axial translation of the test article is sufficient. A 2D or 3D motion stage apparatus can be used to extract axial-radial maps of ion divergence [72] as well as ion swirl speeds [21, 73] in thruster plumes. When vertically lifting large thrusters or translating them over significant distances, care must be taken to ensure that the thruster remains level; counterweighting or force redirection structures may be necessary for this purpose. As described in the following section, mounting the LIF optics on small motion stages can provide additional flexibility for in situ corrections of thermally-induced alignment drift.

3.8 Alignment and Position Referencing Techniques

In many electric thruster applications, thermal-induced position drift makes it difficult to simultaneously maintain alignment across multiple laser injection and collection optics. It is often necessary to add micro-motors to the laser injection and/or collection optics to allow remote control of the tilt and pan (or translation of the optics along two axes) for the purpose of compensating for thermal drift. Which motion axis need to be motorized, such that adjustment is possible while the facility is evacuated, and which motion axis can be left to manual adjustment is highly dependent on the facility, the test setup, and the power level of the test article. It may be feasible, for example, to keep the collection optic fixed while moving the thruster and each injection optic as needed to maintain alignment [69]. Some pathfinding activities may be needed to determine the best approach. The remaining technique descriptions focus on a test setup where the thruster is on translation stages and the tilt and pan of each set of optics are motorized, but equivalent techniques can be applied to other variations of test setup.

To align the laser injection and collection optics, the typical approach is to deploy some combination of low-power visible light sources (e.g., low power gas HeNe laser for the laser injection optics, incoherent gas lamp or low-power laser for the collection optics) or the light from the actual measurement laser, at reduced power if needed for safety [20, 69]. If the wavelength of the alignment light is much different than that of the measurement light (i.e., the wavelength of the laser for injection optics and wavelength of the fluorescence for collection optics), difference in the behavior of the optics with wavelength should be accounted for. For example, the lens may need to be achromatic over a range of wavelengths that covers both the measurement light and the alignment light for the alignment to be effective.

Rough positioning of the optics prior to chamber pumpdown is typically accomplished with geometric measurements (e.g., measuring tape, straight edge, laser level, laser protractor, etc.). If the thruster will be mounted on a two- or three-axis translation stage assembly, the stages should first be leveled and aligned perpendicular to one another. When the thruster is installed, it should be aligned with the coordinate system defined by the stages (i.e., with the thruster aligned to fire along the direction of the axial stage). When the test setup includes an axially injected beam, a useful technique is to place a mirror on a known flat (forward-facing) surface of the thruster and adjust the axial beam alignment until the beam overlaps its reflection. Take care that all optics and laser involved are able to handle the increased power from having the laser overlap itself. Similar techniques involving precisely angled mirrors can be used for other laser injection axes. The thruster may need to be mounted on a platform with some tilt and roll adjustment to aid this part of alignment. Once one of the injection axes is defined, other axes can be positioned by using

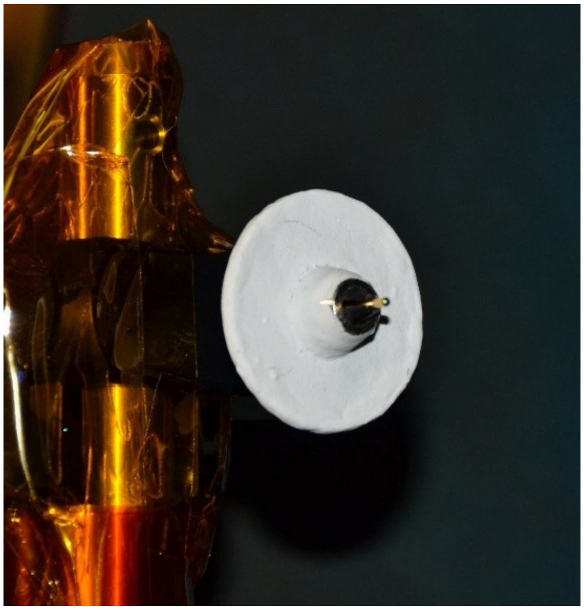

Figure 4: Custom-built reference target for in-situ laser alignment [20].

laser protractor. Another useful technique is to mount an alignment pin or similar feature on the motion stages; by aligning the injection beam to this pin with a visible low-power laser, and then moving each stage an appropriate distance to translate the pin's position along the desired laser injection axis, the injection optic alignment can be verified by noting whether the defocused laser spot remains centered horizonally and vertically on this pin.

A feature on the dynamic side of the translation stages, as close to the thruster as possible or on the thruster, is typically used as an alignment and positioning reference for both initial and in-situ alignment adjustments under vacuum. For example, this reference can be the edge of a cathode bore, a feature of a fastener on the thruster face, or even a custom built target as shown in Fig. 4. When performing the alignment, the typical approach is to first use the thruster translation stages to bring the reference feature into the interrogation area to a pre-defined position. Then, light is sequentially injected through each set of laser injection and collection optics, and the tilt and pan motors are used to align each set of optics so that their light spot lands at the reference feature. A different color of light can be used for the collection optics so that the overlap between the collection optic's beam spot and each injection optic's beam spot can be checked [69]. For carrying out alignment under vacuum in a large vacuum chamber, it is useful to have a high-zoom camera view the alignment feature either from inside the vacuum chamber or through a chamber window. Another approach is possible if the reference feature has a reflective hemispherical surface like the tip in the custom target shown in Fig. 4 [20]. For this approach to work well the tip should be approximately the size of the beam spot. When aligning with this type of target, the measurement laser light can be placed on the target and the intensity of the reflection collected by the collection optic can be used to align the optics.

Once initial alignment is complete, it may be necessary to check where the interrogation zone lands as the thruster is moved. For example, depending on the weight of the thruster and the strength of the stages used, it is possible for the thruster support to droop slightly as the motion stages are moved. This may necessitate fine tuning the alignment (e.g., minor tilt or roll adjustment to the thruster, or raising or lowering optics to get the laser plane to align with the motion stage travel axis).

It is worth noting that a special alignment technique for troubleshooting purpose can be used during steady thruster operation (i.e., when the discharge condition negligibly changes over the alignment period). In this case, alignment can be checked by setting the interrogation zone at a known quiescent location (e.g., upstream of acceleration region for a Hall thruster), setting the laser wavelength to the wavelength of peak intensity, and measuring the amount of fluorescence collected as the motors are tweaked. Note that the use of thruster plasma for alignment is only recommended as a check of other alignment techniques as changes in the condition of the plasma can be mistaken for changes in the test setup alignment.

Alignment is typically performed once before test facility evacuation and periodically throughout testing. The exact frequency of alignment can vary from once per hour to once per day and is highly dependent on the facility, the test setup, and the power level of the test article. Some pathfinding activity may need to be performed to identify an appropriate alignment frequency. For larger test facilities, alignment may shift during facility evacuation due to slight changes in the position and shape of the facility. This can be accounted for by checking alignment more frequently during evacuation or using a large target disc (see Fig. 4) with a camera to quickly locate where the laser beam has drifted to. The motors of stages used to align the optics must have sufficient angular or linear range to encompass the extent of plausible drifts during both pump-down and thruster operation.

4 Analysis of Single-Photon LIF Data

There are many approaches to analyzing laser-induced fluorescence data, and the user is advised to weigh the trade-offs of effort versus payoff when determining which approach to implement. Implementing multiple approaches as an exploratory activity can also help determine the best path forward for subsequent analyses. Regardless of selected approach, the user should try to estimate the uncertainty in the final results associated with the fidelity of analysis performed.

4.1 Basic Analysis Techniques

Typical LIF data analysis begins with converting laser wavelength into velocity using Eq. 1 and applying power corrections to the signal intensity as a function of wavelength (necessary if the laser power delivered to the interrogation volume varies as a function of wavelength, see Sec. 3.4). Assuming an accurate reference(s) is used, it is possible to stitch or stack multiple LIF scans together. Stitching LIF scans from multiple ranges of wavelengths allow a wider range of particle velocities to be mapped than if only one scan is done, but may increase measurement uncertainty. Ideally, each of the scans being stitched should have a wavelength range that covers the stationary wavelength reference, if a wavelength reference is in use. Scans being stitched together should have at least 33% overlap in wavelength range (preferably 50% or more), and errors induced by stitching will be minimized if the scans have relatively high SNR (> 20). Stacking multiple LIF scans from the same wavelength range with the same data acquisition settings can be done to increase the signal-to-noise level of the resulting scan. Once pre-processing corrections are completed, the result should be in the form of signal (also called relative intensity) versus velocity for each laser injection axis.

The simplest approach to analyzing LIF data is to identify the most probable particle velocity, i.e., the velocity at which the signal peaks. The next level of complexity involves calculating the first moment integral of the signal as a function of velocity, yielding the mean velocity u of all particles measured along the associated laser injection axis. The mean velocity is equal to the most probable velocity for an equilibrium, Maxwellian velocity distribution. If multiple laser axes are used, perform the first moment calculation for each laser axis and use geometry to calculate the associated two-dimensional or three-dimensional velocity vector. A typical form of the first moment integral is

$$u = \frac{\int_{-\infty}^{\infty} I(v)\, v dv}{\int_{-\infty}^{\infty} I(v)\, dv} \tag{2}$$

where u is the mean velocity, $I(v)$ is the relative intensity as a function of velocity (proportional to the VDF $f(v)$, and v is the velocity along the laser axis being analyzed. Similarly, the ion or neutral temperature T along the measurement axis (or the effective temperature associated with the kinetic energy spread, if the ions/atoms are not sufficiently collisional to be thermalized) can be calculated from the second moment integral:

$$T = \frac{M}{k_B} \frac{\int_{-\infty}^{\infty} I(v)\,(v-u)^2\, dv}{\int_{-\infty}^{\infty} I(v)\, dv} \tag{3}$$

where M is the atomic mass and k_B is the Boltzmann constant. If the velocity distribution function has been normalized so that the total area under the curve is unity, then the lower integral in each case drops away. When evaluating the moment integrals, care should be taken to address the effects of noise before integration. Example of noise effects that should be removed include a DC offset in the signal that can occur when certain instruments are electrically floated, and recording of the absolute magnitude of noise (obtained from a lock-in amplifier operating in R mode) instead of the phased component of noise (obtained from a lock-in amplifier operating in X mode). Any noise that does not average to zero over the domain of the signal will create an artificial bias in the associated moment integrals. It is also important for the laser wavelength scan to be broad enough that the measured signal after averaging out the noise goes to zero at the bounds.

For data sets where the Doppler-induced broadening are at least an order of magnitude greater than non-Doppler broadening effects (e.g., hyperfine structures, Zeeman effect), a curve-fit approach can typically be used to reduce the data. This criterion may be met for some transitions in certain regions of the test article of interest but is not generally satisfied for all cases. The user should perform a basic analysis to estimate the expected broadening due to non-Doppler effects, particularly hyperfine structures and the Zeeman effect, in the measurement regions of interest and compare that to the width of the measured distribution functions to determine whether the criterion is met. Refer to Sec. 4.4 for more details.

The most common curve fitting function is a Gaussian, representing the Maxwell-Boltzmann distribution exhibited by plasmas in thermal equilibrium [3, 20, 69, 74–77]. However, in many cases within EP plasmas the heavy particles are not sufficiently collisional to maintain equilibrium, and their VDFs deviate significantly from a Maxwellian shape. Other commonly used forms include the skew-normal distribution to better capture tails (low- or high-velocity) often present in non-Maxwellian plasmas, and a two-Gaussian distribution for situations when either two ion/neutral populations are present [20] or when the velocity distribution appears to be bi-model due to phenomenon like plasma oscillations [20, 21, 73, 78]. The Gaussian, skew-normal, and two-Gaussian functions are shown in Eqs. 4, 5, and 6, respectively.

$$I(v) = A_1 \exp\left(\frac{(v-u_1)^2}{v_{T1}^2}\right) \tag{4}$$

$$I(v) = A_1 \exp\left(\frac{(v-c_1)^2}{c_2^2}\right)\left[1+\operatorname{erf}\left(\frac{c_3\,(v-c_1)}{c_2}\right)\right] \tag{5}$$

$$I(v) = A_1 \exp\left(\frac{(v-u_1)^2}{v_{T1}^2}\right) + A_2 \exp\left(\frac{(v-u_2)^2}{v_{T2}^2}\right). \tag{6}$$

In these equations, the adjustable fit parameters are the mean velocity u_j, thermal velocity $v_{Tj} \equiv \sqrt{2k_B T_j/M}$, and amplitude A_j for population j, as well as the skew normal fit parameters c_1–c_3. For any general curve-fit form, once the curve-fit constants have been derived, the first moment integral can be calculated to obtain the average velocity, while the curve-fit result is the velocity distribution function. Although the curve-fit approach is more resistant to noise than direct moment integral calculation, it is not entirely immune, particularly if the SNR is in the single digit range. DC offsets as described earlier in this section should be properly removed prior to data analysis.

If the Zeeman effect in the signal is non-negligible but not dominant (Zeeman broadening a few times less than Doppler broadening) and a model of the Zeeman effect exists for the transition line in question, it is still acceptable to use the curve-fit approach provided that the Zeeman effect is appropriately removed. Information regarding the magnitude of the external magnetic field strength for the polarization direction in question most be available. This is typically obtained using a magnetic field map either measured or simulated depending on the application. In this scenario, the curve-fit algorithm must be set to fit the chosen equation form convolved with the Zeeman model informed by the local magnetic field strength. For example, if the measurement location has an external field strength of 1000 G in σ polarization, the lineshape for 1000 G is generated from the Zeeman model and convolved with the curve-fit lineshape with the initial set of curve-fit parameters. The algorithm then compares the result with the measured lineshape and adjusts the curve-fit parameters in an iterative fashion to achieve a good match. Once the curve fit is completed, the velocity distribution function, with the Zeeman effect removed, is represented by the final curve-fit [20]. For reference, the convolution operator is defined mathematically by

$$f(x) * g(x) \equiv \int_{-\infty}^{\infty} f(x-y)\, g(y)\, dy, \tag{7}$$

where $*$ denotes convolution.

The primary advantage of the curve-fit approach is that it is resistant to noise and fairly straightforward to implement. The primary disadvantage of the curve-fit approach is that the curve-fit form may not adequately represent the measured distribution function (e.g., fitting a Gaussian form to a population that has a long energy tail).

4.2 Deconvolution Methods

Mathematically, the measured LIF signal can be represented as a convolution of various Doppler and non-Doppler components:

$$I(\nu) = [(h(\nu) * L(\nu)) * g(\nu)] * w(\nu) \approx h(\nu) * g(\nu)\,, \tag{8}$$

where ν is the photon frequency, $h(\nu)$ is the hyperfine line profile accounting for the Zeeman effect, $L(\nu)$ is the Lorentzian natural and Stark broadening (often negligible and ignored in EP plasma applications), $g(\nu)$ is the Doppler component, and $w(\nu)$ is the laser linewidth (negligible for diode lasers). Deconvolution (denoted by $*^{-1}$) can be used to retrieve the Doppler component:

$$g(\nu) = I(\nu) *^{-1} h(\nu)\,. \tag{9}$$

One method to perform the deconvolution operation is to use Fourier transforms. Based on the convolution theorem, the Fourier transform of the convolution of two functions is the point-wise product of the Fourier transforms of each function. Similarly, deconvolution can be performed by first performing the Fourier transform (denoted by $\mathcal{F}\{f(x)\}$), then performing point-wise division, and then performing the inverse Fourier transform:

$$g(\nu) = \mathcal{F}^{-1}\left\{\frac{\mathcal{F}\{I(\nu)\}}{\mathcal{F}\{h(\nu)\}}\right\}. \tag{10}$$

However, the division operation tends to amplify any noise in the measured intensity. One approach to reduce the noise is to use an inverse Gaussian filter, which suppresses high-frequency noise at the expense of smearing out the signal [60]. Aside from determining the correct amount of filtering to use, some techniques require the domain of analysis to be symmetric about zero. This can be achieved by padding any missing part of the domain with zeros before performing the transform. The artificially added domain parts are then removed after the transform. Numerous texts exist on the use of Fourier transforms to perform deconvolution, for example Ref. 79. The user is encouraged to perform their own research on the optimal implementation of Fourier transform-based deconvolution for their application.

Another method for performing deconvolution is called Tikhonov Regularization. The Tikhonov method was first proposed to solve ill-posed problems; i.e., problems for which the solution is not unique or does not vary continuously with the data inputs. Petrov's description of the application of Tikhonov's method to spectral deconvolution [80] is cited here because the original paper by Andrey N. Tikhonov in 1963 (Soviet Mathematics volume 4, page 1035-1038) does not appear to be publicly available. The Tikhonov method reframes the deconvolution problem in the form of matrices and arrays:

$$b(\nu) = c(\nu) *^{-1} a(\nu) \quad \leftrightarrow \quad \boldsymbol{b} = \boldsymbol{A}^{-1}\boldsymbol{c}, \tag{11}$$

where $\boldsymbol{b}$ and $\boldsymbol{c}$ are the line profiles $b(\nu)$ and $c(\nu)$ in vector format, respectively, and $\boldsymbol{A}^{-1}$ is the inverse of the broadening function in the form of a square matrix (the rows of $\boldsymbol{A}$ should each contain a vector representing the broadening function, shifted to be centered on the diagonal matrix element in each row). The form in Eq. 11 is unstable to noise; to reduce the influence of noise, both sides of the equation are multiplied by $\boldsymbol{A}^T\boldsymbol{A}$, where $\boldsymbol{A}^T$ is the transpose of $\boldsymbol{A}$, and then a term is added to the left-hand side:

$$\boldsymbol{A}^T\boldsymbol{A}\boldsymbol{b} + \alpha\boldsymbol{I}\boldsymbol{b} = \boldsymbol{A}^T\boldsymbol{c}, \tag{12}$$

where $\boldsymbol{I}$ is the identity matrix and α is called the regularization parameter, held constant in a given run. Whereas the original deconvolution problem using noisy data is ill-posed, the modified format shown in equation 12 yields a single solution for a given choice of α. The Tikhonov method does not add filter-related broadening but can still artificially smooth out sharp features, with higher values of α leading to decreased noise effects but increased smoothing. Techniques exist to optimize the value of α to balance suppressing noise versus maintaining sharp features [81]. The primary advantage of Tikhonov regularization is good accuracy. The primary disadvantage is computation speed associated with the need to perform matrix inversion [78].

Given the challenge that experimental noise poses for deconvolution, another useful technique is to fit a function such as those shown in Eqs. 4–6 to the measured line profile $I(\nu)$, then perform deconvolution either analytically (when feasible, as in Ref. 77) or numerically using one of the techniques described above. This approach should only be used if a functional form can be identified that fits the data well.

4.3 Saturation

Saturation of the LIF signal occurs when the population of the upper level of the target transition becomes comparable to the population of the lower level and thus the rate of stimulated emission, in which the incident laser photon triggers de-excitation of an atom or ion in the upper state [82], becomes comparable to the rate of photon absorption by an atom or ion in the lower state. This process is an important consideration for designing LIF experiments because it can lead to distortion of the measured IVDF. The basic features of saturation may be derived from a simple two-level model of the atom that includes only the lower and upper states of the laser-driven transition [63]. Considering a single hyperfine component, and considering only the population of particles moving with velocity between v and $(v + dv)$ along the laser injection axis, the equilibrium population density of the upper state when the laser intensity is I_ν at frequency ν is

$$n_2(\nu; v) = \left(\frac{g_2}{g_1 + g_2}\right)\left(\frac{I_\nu}{I_\nu + \left(\frac{g_1}{g_1+g_2}\right)\frac{8\pi h\nu_0^3}{c^2 L(\nu;\nu_0,v)}}\right) n_t(v)\,, \tag{13}$$

where the subscript 1 represents the lower state and 2 represents the upper state, g_i are the statistical weights of the levels, h is Planck's constant, c is the speed of light, $L(\nu; \nu_0, v)$ is a Lorentzian function representing the naturally broadened line profile function, ν_0 is the rest frame line center frequency, and $n_t(v) = n_1(\nu; v) + n_2(\nu; v)$ is the total population of particles in the infinitesmal velocity bin. Note that the LIF signal intensity is proportional to the upper state population. The population fraction $n_2(\nu; v)\,/n_t(v)$ of the upper state is maximized at the laser frequency $\nu = (1 - v/c)\,\nu_0$ corresponding to the peak of the Lorentzian function, which means that the center of the line profile function saturates faster than the wings. As a result, operating in a highly saturated regime causes the measured line profile to be artificially broadened, leading the LIF measurements to overestimate the ion or neutral temperature.

At its peak, the Lorentzian function evaluates to $4/\gamma$, where γ is the total spontaneous decay rate of the upper level into all lower states, so we have

$$n_2((1 - v/c)\,\nu_0; v) = \left(\frac{g_2}{g_1 + g_2}\right)\left(\frac{I_\nu}{I_\nu + \left(\frac{g_1}{g_1+g_2}\right)\frac{2\pi\gamma h\nu_0^3}{c^2}}\right) n_t(v) \equiv \left(\frac{g_2}{g_1 + g_2}\right)\left(\frac{I_\nu}{I_\nu + I_{sat.}}\right) n_t(v)\,, \tag{14}$$

where $I_{sat.}$ is called the "saturation intensity". Saturation acts on the homogeneous line profile, which is a property of an individual atom or ion, rather than the inhomogeneous Doppler profile, which is a property of a collection of particles. To calculate the overall effect of saturation on the apparent IVDF measured by LIF, we must integrate Eq. 13 over all ion velocities [63]:

$$n_2(\nu) = \int_{-\infty}^{\infty} n_2(v, \nu)\, dv \propto I(\nu)\,, \tag{15}$$

where $I(\nu)$ is the LIF signal intensity defined in Sec. 4.1, not to be confused with the laser intensity I_ν at frequency ν. The saturated line profile should also be summed over all isotopes, as this portion of the hyperfine structure acts as an inhomogeneous line profile broadening mechanism. The hyperfine structure components due to nuclear spin should be included in the original homogeneous line profile for each isotope, requiring the Lorentzian profile function used above to be replaced by a more complex function in some cases. For situations with substantial Doppler broadening, it may be possible to operate at laser intensities many times the saturation intensity while maintaining acceptable accuracy of mean velocity and temperature measurements [63], but for high enough intensities significant distortion will always occur.

In general, it is not possible to remove the distortion brought on by saturation from raw LIF traces in post processing. This is because modeling saturation effect requires knowledge of the laser intensity profile

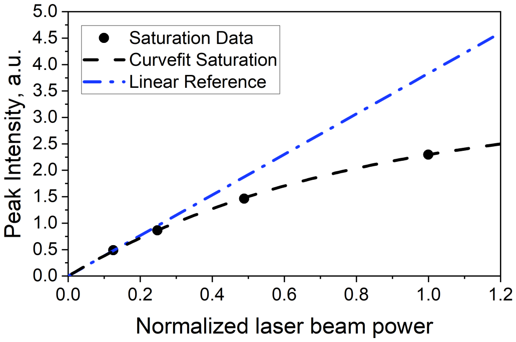

Figure 5: An example saturation study performed on a Hall thruster operating at 300 V, 6 kW [78].

at the interrogation zone. It is possible to make an approximation or to measure this profile in a static application, but in an electric propulsion application the laser intensity profile can vary with thermal drift, complicating any attempt at correction. The preferable approach is to avoid excessive saturation when the application involves measuring VDFs. This is accomplished by performing saturation studies in which the input laser intensity is varied, e.g., using neutral density filters, to map the response as a function of input laser intensity.

Figure 5 shows an example plot from a saturation study of the Xe II 834.953 nm transition performed at the exit plane, on the channel centerline, of a Hall thruster operating at 300 V, 6 kW [78]. In this example, the peak intensity is the key metric because, as seen in Figure 2, it is the most sensitive part of the lineshape to saturation effect. The black dashed line is a curve-fit based on Equation 14 and the blue dot-dash line is a reference for where the data point would have laid if the response was completely unsaturated. For an LIF study where precise VDF is not the goal, a linearity threshold of 10% is typically sufficient, which for this example would have corresponded to the data point at a normalized laser beam power of 0.25 (second from the left). Another approach for saturation study is to plot the total response (i.e., integrated over all frequencies) versus input laser power; a threshold of no more than a few percent is typical for this approach. Lastly, if the goal of an LIF study is to obtain precise VDF, then the key metric should the full-width-at-half-maximum value, or the ion temperature, or some equivalent measure of the width of the distribution. In this scenario, the threshold is simply the maximum acceptable amount of broadening for the study and is typically set at a few percent.

4.4 Hyperfine Structure and Zeeman Splitting

4.4.1 Hyperfine Structure

Isotope	124	126	128	129	130	131	132	134	136
Abundance	0.096	0.090	1.919	26.44	4.075	21.18	26.89	10.44	8.87

Table 2: Abundances of natural Xe isotopes in %.

Xenon is chosen here as a reference. Examples of optical transitions for xenon are shown in Table 1, and the composition of the natural mixture of xenon isotopes is shown in Table 2. There are a multitude of even isotopes with different abundances. Those isotopes do not exhibit a hyperfine splitting as their nuclear spin is zero. The slight nucleus mass and volume differences are, however, at the origin of an energy shift for all levels. The consequence is a slight difference in wavelength for a given transition of different isotopes, the so-called isotope shift (IS).

There are also two odd isotopes: ^{129}Xe and ^{131}Xe with a nuclear spin $\mathbf{I}$ of 1/2 and 3/2, respectively. Energy levels of those isotopes do exhibit a hyperfine splitting that is described by the total angular momentum quantum number $\mathbf{F} = \mathbf{I}+\mathbf{J}$, where $\mathbf{J}$ is the total angular momentum of electrons [83, 84]. The energy shift of a sublevel is given by the sum of the magnetic dipole and the electric quadrupole contributions [83, 85, 86]:

$$\Delta E = \Delta F_M + \Delta F_Q. \tag{16}$$

The two components read:

$$\Delta F_M = \frac{1}{2} A \left[F(F+1) - J(J+1) - I(I+1) \right] = \frac{1}{2} A \cdot R, \tag{17}$$

$$\Delta F_Q = \frac{1}{4} B \frac{\left[\frac{3}{2} R(R+1) - 2J(J+1)I(I+1) \right]}{J(2J-1)I(2I-1)}, \tag{18}$$

where the numbers A and B are the magnetic dipole and electric quadrupole constants, respectively. From the theory of hyperfine interaction, the ratio between the magnetic dipole constants A of the ^{129}Xe and the ^{131}Xe isotopes scales as the ratio of their nuclear moments μ times the reciprocal of their respective nuclear spin. The ratio is equal to -0.2964. Note that $\mu_{129} = 0.7768\,\mu_B$ and $\mu_{131} = 0.6908\,\mu_B$, where μ_B is the Bohr magneton.

The selection rule for a hyperfine transition is $\Delta F = F - F' = [0, 1]$. The $F \to F' = 0$ transition is forbidden. Hyperfine splitting therefore gives 12 components for the Xe II line at 834.953 nm. The intensity of any hyperfine component can be computed from Clebsch-Gordan coefficients [87]. Note that the relative intensity for each isotopic component can be calculated from the isotope abundance.

The isotope shifts and the hyperfine structure (HFS) of a spectral line can be resolved when overcoming the limitation set by Doppler broadening using non-linear absorption techniques based on selective saturation of individual atomic transitions [85, 88] or intermodulated spectroscopy [50].

4.4.2 Zeeman Effect

The Zeeman effect corresponds to the splitting of a spectral line into several components due to the presence of a static magnetic field. The lineshape is modeled either in the weak or strong field approximation. The latter corresponds to the occurrence of the Paschen–Back effect. The choice of relying either on the weak or strong field approximation depends on the local strength of the applied magnetic field in the context of the hyperfine interaction [83]:

$$\begin{array}{rcll} g_J \mu_B |B|/(Ah) & \ll & 1 & \text{weak field} \\ g_J \mu_B |B|/(Ah) & \gg & 1 & \text{strong field} \end{array}$$

where g_J is the Landé g-factor, μ_B is the Bohr magneton, $|B|$ is the magnetic field strength, A is the magnetic dipole constant and h is the Planck constant. For the modeling of the usual xenon line profiles, the weak field approximation is valid as long as the magnetic field intensity remains below $\sim 0.1\,\mathrm{T}$ for atoms and $50\,\mathrm{mT}$ for singly-charged ions. In practice, the modeling of a line consists in four distinct steps:

1. Find all the allowed optical transitions;
2. Quantify the associated detuning frequency or wavelength;
3. Determine the relative intensity of each line;
4. Include Doppler broadening and Doppler shift to finally retrieve the complete lineshape.

In the weak field regime, the upper and lower energy levels of the probed transition are solved by the determination of the total angular momentum F and the magnetic quantum number $\mathbf{M}_F = \mathbf{M}_J + \mathbf{M}_I$ for the hyperfine sub-levels, whereas the electronic angular momentum J and the magnetic quantum number M_J are required for the even isotopes [85, 89]. The hyperfine components are beforehand identified by the dipole–dipole selection applied to the F quantum number as previously explained. In the strong field case, F and M_F are undefined quantum numbers, therefore the set (I, J, M_I, M_J) needs to be used instead. Finally the optically allowed transitions are set by the values of $\Delta M_{F,J}$. A laser beam polarization perpendicular to the $\mathbf{B}$ field vector corresponds to the so-called σ-components with $\Delta M_{F,J} = \pm 1$, while polarization parallel to the magnetic field produces the π-components with $\Delta M_{F,J} = 0$. The selection

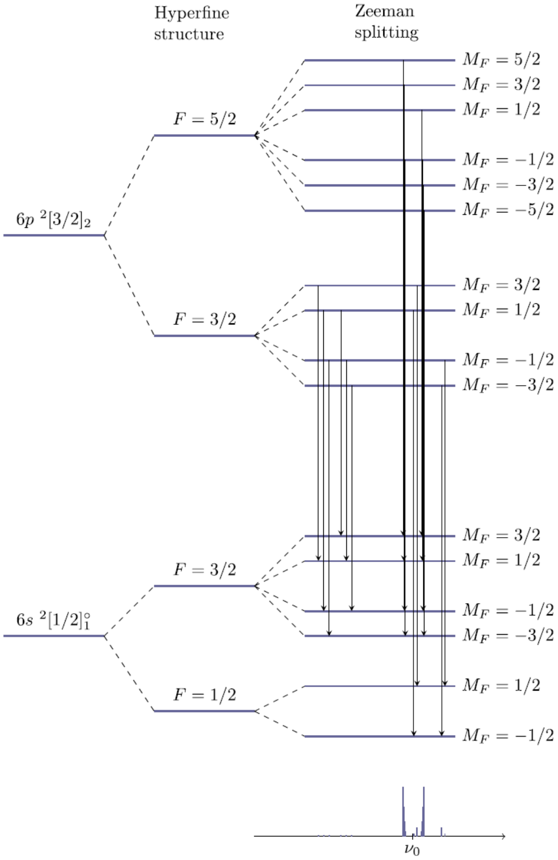

Figure 6: Hyperfine and Zeeman components for the ^{129}Xe σ-transitions of the Xe I line at 834.68 nm [28]. The lines are spaced in accordance with the computed detuning from the reference frequency ν_0. The relative intensity of each line is shown below the diagram.

rule $\Delta M_I = 0$ must additionally be accounted for whenever the strong field condition is met. For the $\left({}^2P^o_{1/2}\right) 6s\,^2[1/2]^o_1 \rightarrow \left({}^2P^o_{1/2}\right) 6p\,^2[3/2]_2$ transition of Xe I, assuming only the σ-components are allowed and the weak field approximation holds, the selection rules lead to 6 lines for each even isotope, 18 for ^{129}Xe, and 54 for ^{131}Xe. Under the same assumptions, the $\left({}^3P_2\right) 5d^2[4]_{7/2} \rightarrow \left({}^3P_2\right) 6p^2[3]^o_{5/2}$ transition of Xe II comprises 12 lines for the each even isotope, 36 for ^{129}Xe, and 108 for ^{131}Xe. An example of the allowed σ-transitions due to HFS and Zeeman effect is shown in Fig. 6 for the ^{129}Xe isotope of the Xe I line at 834.910 nm [28]. Several additional transitions appear when the π-components are included.

The energy shift of each transition is computed as the sum of three terms [90]: the isotopic shift ΔE_{IS}, the HFS contribution ΔE_{HFS}, and the Zeeman effect contribution ΔE_Z. The values of ΔE_{IS} for the Xe I and Xe II lines are for instance tabulated in [91] and [92], respectively. In Fig. 6, the energy reference ν_0 is the one of ^{132}Xe since it is the most abundant isotope without hyperfine structure. The hyperfine constants A and B needed to calculate the magnetic dipole and electric quadrupole contributions to the HFS for odd isotopes (refer to Eqs. 17 and 18) can be found in [83, 93] for some xenon transitions. ΔE_Z, is a function of the magnetic quantum number $M_{F,J,I}$, the strength of the magnetic field and the Landé g-factor g_F or g_J, depending on the isotope atomic number and the weak/strong field regime. Complete expressions for ΔE_{HFS}, ΔE_Z and g_F can be found in [83]. The values of g_J and the nuclear magnetic dipole moments μ_I necessary to compute g_F are provided in references [37, 94].

After the energy shift of each transition is known, the complete spectrum is built by determining the relative intensity of each peak. The equations of interest are reported in [83] for each of the π and σ components. They are function of F and M_F for the odd isotopes and J and M_J for the even isotopes. The computed intensities must be weighted accounting for the natural abundance of each isotope [95] and

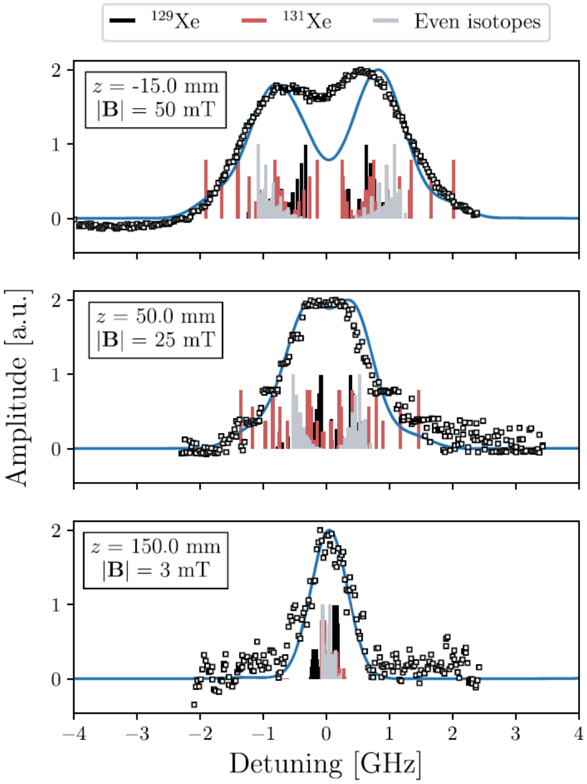

Figure 7: Experimental (squares) and simulated (line) lineshape for the $5d\,^2[4]_{7/2} \rightarrow 6p\,^2[3]^{\circ}_{5/2}$ transition of Xe II. Experiments were performed at various axial positions z in the magnetic nozzle of a helicon plasma thruster [28]. Only σ-components are considered in the calculation.

hyperfine components tabulated in [96] as a function of I, ΔJ and ΔF. Furthermore, in order to account for the laser polarization direction, the intensity of each π transition is scaled by $\sin(\theta)$, where θ is the local relative angle between the laser beam wave vector $\boldsymbol{k}$ and the magnetic field $\boldsymbol{B}$.

At last, Doppler broadening and Doppler shift of each transition are addressed. It is reasonable to assume that the Doppler broadening dominates over the natural line width and the laser bandwidth (which is very narrow for CW laser sources). A Gaussian profile, i.e., an equilibrium velocity distribution, is applied to each component, exhibiting identical width (temperature) and frequency shift (velocity). Eventually, the modelled lineshape stems from the sum of all individual Gaussian profiles.

Figures 7 and 8 show two simulated xenon ion lineshapes compared to the experimental spectra measured by means of LIF spectroscopy. Measurements were performed in the magnetic nozzle of a helicon plasma thruster firing at 350 W [28]. A similar study has also been carried out with a greater magnetic field in the nozzle of an electron cyclotron resonance (ECR) plasma thruster [97]. In the case of Figure 7, measurements were performed along the nozzle axis with a polarization vector perpendicular to the magnetic field so only σ-components were considered in the simulation. In the second case, measurements were performed off axis with a 15° angle between $\boldsymbol{k}$ and $\boldsymbol{B}$, therefore π-components were accounted for as well. A fixed ion temperature of 800 K was assumed in the simulations here; temperature can alternately be treated as a free parameter when fitting the model to the experimental data. As can be seen in the two figures, there is a fairly good agreement between simulation outcomes and measurements. However, a relatively poor match in the 0 GHz region is found for the double-peak lineshape of Fig. 7. A slight misalignment and/or a relatively large probed volume would enable the occurrence of π-transitions that are not taken into account in the calculation. The most probable velocity is estimated within the code by finding the frequency offset (Doppler shift) that gives the best match between the experimental and modeled lineshapes.

Modeling of the lineshape with IS, HFS and Zeeman splitting furnishes the temperature and the most probable velocity with a reasonable accuracy. The error bars result from several contributing factors, such

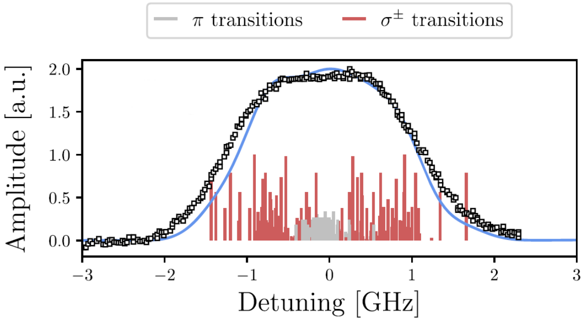

Figure 8: Experimental (squares) and simulated (line) lineshape for the $5d\,^2[4]_{7/2} \rightarrow 6p\,^2[3]^{\circ}_{5/2}$ transition of Xe II. Experiments were performed off the axis of the magnetic nozzle of a helicon plasma thruster [28]. Both σ- and π-components are taken into account here.

as uncertainty in the hyperfine constants and isotopic shifts, the angle between $\boldsymbol{k}$ and $\boldsymbol{B}$, the quality of the raw data, and the robustness of the fitting algorithm. It is also possible to utilize fitting of a Zeeman broadening model to LIF absorption line profiles to make an in situ measurement of the local magnetic field in a thruster [98–100].

The Xe II 834.953 nm transition is known to have very narrow hyperfine structure, and at magnetic field strengths typical in Hall thrusters, Zeeman broadening of this transition by σ polarized photons can be accounted for via a simple linear model [67, 78]. Convolving the measured line profile with the Zeeman profile function

$$h(\nu) = \frac{1}{2}\left[\delta\left(\nu - \frac{1}{2}\alpha B\right) + \delta\left(\nu + \frac{1}{2}\alpha B\right)\right] \tag{19}$$

(where ν is the photon frequency, B is the magnetic field strength and the measured value of α is 2.7273 MHz/Gauss [78]), we find that the apparent ion temperature for a Zeeman-broadened Maxwellian is

$$T_i^* = T_i + \frac{m_i}{4k_B}\left(\frac{c}{\nu_0}\alpha B\right)^2. \tag{20}$$

Here T_i is the actual ion temperature, T_i^* is the apparent temperature that would be derived from a second moment integral of the LIF data if no Zeeman splitting correction were applied, c is the speed of light, and ν_0 is the line center frequency. The temperature error is a simple offset proportional to B^2, which may be neglected if $T_i^* \gg (m_i/4k_B)\,(c\alpha B/\nu_0)^2$. Alternately, when Zeeman splitting of the 834.953 nm transition is non-negligible, Eq. 19 may be used in a deconvolution algorithm to remove the effect (refer to Sec. 4.2). The situation is more favorable for π polarization of the laser, which leads to Zeeman broadening of the 834.953 nm line that is at least an order of magnitude smaller than that associated with σ polarization. Whether such shortcuts exist is highly situation dependent, and the user is advised to perform literature review of the specific transition line they are reducing data for prior to data reduction. In many cases, detailed modeling of the Zeeman and/or hyperfine broadening, following the procedures described earlier in this section, may be necessary for accurate estimates of the mean velocity and particularly the temperature. Alternately, the user may be able to derive an empirical model using a variety of spectroscopic methods [101, 102].

4.5 Electric Field Calculations

The electric field distribution plays a fundamental role in the dynamics, physical processes, and organization of plasma discharges as it governs to a large extend the species transport, wave structures, ionization phenomena and sheath properties. Electrostatic probes like Langmuir and emissive probes are widely employed to determine the local plasma potential, from which the electric field can be derived. However, the suffer from a variety of drawbacks, such as the lack of a complete theory, contamination issues, and their inherent intrusive nature [18, 19]. LIF measurements of the ion velocity distribution function (IVDF) can provide an attractive alternate for indirect determination of the electric field if an appropriate physical model is used.

The purpose of this section is to evaluate the applicability of different models for computing the electric field distribution from CW LIF measurements in low-pressure plasma discharges with unmagnetized ions. These techniques have been primarily applied to Hall thrusters.

4.5.1 Energy Conservation Method

The ion mean velocity (first order moment of the VDF, see Eq. 2) or the most probable velocity can be used to evaluate the accelerating potential U from the steady state energy conservation equation assuming a collision-free medium. The equation then simply reads:

$$\frac{1}{2} m_i v^2 = eU \qquad \longrightarrow \qquad E_x = -\frac{m_i}{2e}\frac{d}{dx}\left(v^2\right), \tag{21}$$

where notations have their usual meaning. Here all ions are singly-charged and the velocity at the origin is assumed to be zero. The electric field is then computed from the spatial derivative of the potential. This approach is the simplest one. Two comments can be made here. First, the use of the most probable velocity is preferred to avoid underestimation of the local electric field due to an overlap between ionization and acceleration regions (or in some cases the first moment may be calculated by integrating over a limited range of velocities that excludes the low-energy ion population [103]). Second, all spatial derivatives should be considered to obtained information on the electric field vector instead of solely the component along the laser axis. To achieve this, in principle a three-dimensional LIF system must be put in place, but 2D measurements are often sufficient in Hall thrusters, where the axial and radial ion velocity components far exceed the azimuthal velocity [73], and even 1D measurements may be adequate on the channel centerline.

4.5.2 Fluid Equations Method

Instead of using the conservation of the ion kinetic energy to assess the $\boldsymbol{E}$ field, a relatively crude approach, we can start from the fluid equations, as explained in Ref. 9. The proposed model relies on steady-state continuity and momentum conservation equations for unmagnetized ions with negligible ion losses, charge-exchange collisions, and momentum-exchange collisions. Neglecting in addition the shear stress and assuming the neutral flow velocity is zero, the electric field axial and radial components are given by [9]:

$$\begin{aligned} \frac{eE_z}{m_i} &= u_z\frac{du_z}{dz} + \nu_i u_z + \frac{1}{nm_i}\frac{dp_{zz}}{dz}, \\ \frac{eE_r}{m_i} &= u_r\frac{du_r}{dr} + \nu_i u_r + \frac{1}{nm_i}\frac{dp_{rr}}{dr}, \end{aligned} \tag{22}$$

where $\boldsymbol{u}$ is the ion mean velocity, ν_i the ionization frequency, n is the plasma density, and p is the ion pressure. To further simplify the previous set of equations, one can assume cold ions ($T_i = 0$). In that case only the ionization contribution remains. With this method, the ionization and pressure gradient terms need to be determined for the electric field to be computed. Measuring or assessing these terms is a complicated task that requires additional experiments. Another method based on the Boltzmann equation can then be considered.

4.5.3 Boltzmann Equation Method

Neglecting charge-exchange collisions, momentum-exchange collisions, and the neutral gas temperature compared to the ion energy, the steady state Boltzmann equation for ions reads

$$\boldsymbol{v}\cdot\nabla_{\boldsymbol{x}} f_i + \boldsymbol{a}\cdot\nabla_{\boldsymbol{v}} f_i = \nu_i f_0, \tag{23}$$

where $\nabla_{\boldsymbol{x}}$ and $\nabla_{\boldsymbol{v}}$ stand for the spatial and velocity gradients, $\boldsymbol{a} = e\boldsymbol{E}$ is the acceleration, $f_i(v)$ is the ion VDF and $f_0(v)$ is the VDF of the neutrals, approximated by a Dirac delta function [104]. The use of the Boltzmann equation has two main advantages. First, it considers the kinetic nature of the plasma processes. Second, the ionization and acceleration terms can be evaluated independently. The 1D1V expression of the axial electric field (i.e., the expression considered only one spatial dimension and one velocity direction) has been developed by Perez-Luna et al. [104] while the 2D2V radial and axial electric field expressions

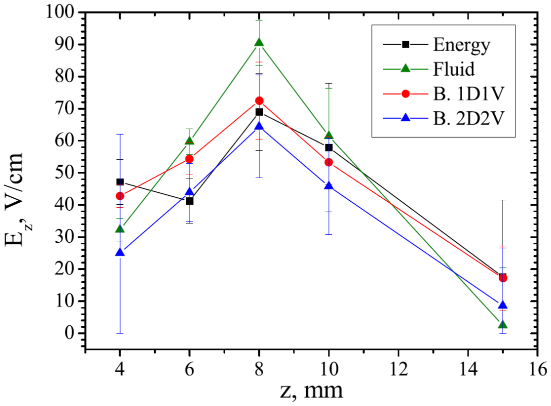

Figure 9: Axial electric field profiles calculated with the energy conservation, the fluid equations, the Boltzmann 1D1V and 2D2V models [9]. $z = 0$ refers to the thruster channel exit plane.

.

have been derived by Spektor [72]. The two methods rely on the determination of the moments of the ion VDF; in its simplest form, the method of Perez-Luna et al. requires only 1D LIF measurements along the direction of the electric field, while Spektor's method requires 2D LIF measurements. The electric field expressions given in Ref. 72 assume that the local 2D ion VDF is the product of the radial and axial VDFs, namely: $f(\boldsymbol{x}, v_r, v_z, t) = f(\boldsymbol{x}, v_r, t) \times f(\boldsymbol{x}, v_z, t)$. This approach is valid for isotropic Maxwellian plasmas. The unambiguous determination of the complete ion velocity distribution can be achieved with optical tomography techniques via the measurement of a large number of 1D ion VDFs [62, 105].

4.5.4 Comparison Between the Methods

Experiments have been performed to compare the four methods with a 200 W permanent magnet Hall thruster fed with xenon as the propellant [9]. The thruster operated at 200 V with a mean discharge current of 0.9 A. The background pressure in the chamber reached 2×10^{-5} mbar. The thruster was mounted on two perpendicular linear translation stages to allow a displacement parallel and perpendicular to the centerline. The optical train and detection brench used for these time-resolved LIF measurements was described in detail in [8]. The $5d\,^2[4]_{7/2} \rightarrow 6p\,^2[3]^{\circ}_{5/2}$ Xe II transition was probed by an amplified tunable single-mode external cavity laser diode at 834.953 nm. The fluorescence light was captured at 542.063 nm and processed with a lock-in amplifier. LIF measurements were performed at several axial and radial locations beyond the channel exit plane with axial (dz) and radial (dr) steps both equal to 0.5 mm for evaluating gradients. Note that neither the isotopic and hyperfine structures nor the Zeeman splitting were taken into account in the study.

Figure 9 shows the results of the electric field on-axis profile calculations. The error bars globally tend to widen when the distance from the source increases due to the reduction in the signal-to-noise ratio. The peak in E_z outside the channel is clearly visible and distinguished by the four methods. The field values are lower with the 2D2V computation for reasons that are not completely understood; more experiments are needed to fully validate this method. The fluid model provides acceptable values of the electric field, although it appears to overestimate the peak field. Surprisingly, calculations based on the very simple energy conservation law give values in good agreement with the ones obtained with the more sophisticated approaches.

In conclusion, the comparative study reveals that the 1D1V Boltzmann equation is a good a trade-off between physical meaning and complexity, especially when ionization plays a significant role. The 2D2V formulation, although more comprehensive, needs additional study before it can be trusted to give reliable results; large error bars may be unavoidable with this method due to high-order moments, which makes proper evaluation of the electric field profile and ionization term difficult. Also note that non-classical ion heating mechanisms in the vicinity of the Hall thruster acceleration region [23, 73, 103] may invalidate these Boltzmann/Vlasov approaches, which assume that any spread in the velocity distribution is due to ions being born at different potentials.

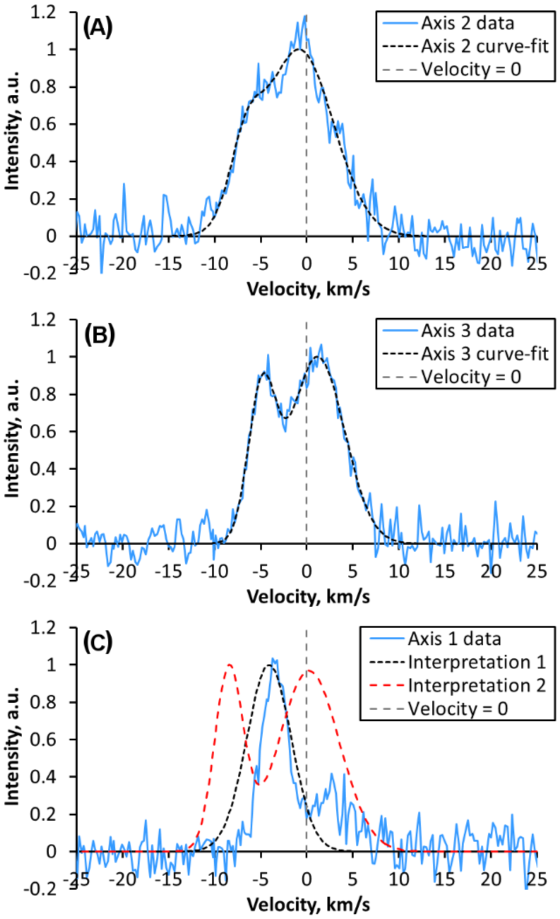

Figure 10: Example of two ion populations mapped along (A) Axis 2, (B) Axis 3, and (C) Axis 1 near the pole of a 600 V, 12.5 kW Hall thruster [20]. (C) also shows two interpretations of the Axes 2 and 3 data when projected onto Axis 1. Axis 1 is axial relative to the thruster, Axis 2 is 47° counter-clockwise from Axis 1 when viewing the test setup top-down, and Axis 3 is 47° clockwise from axis 1 in the same view.

.

4.6 Identifying Ion Populations In Multi-Directional Measurements

When measuring ion velocity along two axes in a plane, in situations with multiple ion populations present it is not always possible to determine which VDF peak on one measurement axis is correlated with a given peak on the other measurement axis. The addition of a third measurement axis with sufficient angular separation with the other two axes can usually resolve this issue.

Figure 10 shows example data near the pole of a 600 V, 12.5 kW Hall thruster [20]. In this example, subplot C shows data from measurement Axis 1, which is pointed along the firing axis. Subplot A shows data from Axis 2, which is 47° counter-clockwise from Axis 1 when viewing the test setup top-down, and subplot B shows 47° clockwise from Axis 1 in the same view. If only data from Axes 2 and 3 (subplots A and B, respectively) were available, since each of these two subplots exhibit two ion populations, it is not possible to correlate the peaks (i.e., we cannot determine whether the left population in subplot A should go with the left population or the right population in subplot B). However, with the addition of Axis 1 data (Figure 3 subplot C), one can compare the profiles predicted by different correlations of Axis 2 and 3 data (called Interpretations 1 and 2 in the subplot) to Axis 1 data and see which correlation leads to a better match. In this example, two-Gaussian curve-fits (see Eq. 6) were performed on Axes 2 and 3 data to generate the average velocity and standard deviation of each ion population. Interpretation 1 corresponds to the left peak of the Axis 2 data correlating to the right peak of the Axis 3 data, and Interpretation 2 corresponds to the reverse correlation. Then, for each ion population, the average velocities on Axes 2 and 3 were used to calculate, via geometry, the predicted velocity on Axis 1, and the standard deviations from Axes 2 and 3 were averaged to obtain the predicted standard deviation on Axis 1. Comparing the resulting predicted profiles to the measured Axis 1 profile, Interpretation 1 was a much better match than Interpretation 2. This correlation technique can be further optimized with the use of a standard error metric when comparing predicted profiles to measured profiles (e.g., root mean square of error, mean absolute error, R-squared).

Use of three LIF laser axes in a single measurement plane can still be effective when there are three ion populations present [106]. However, any specific data set may exhibit more than one interpretation that are similar in goodness according to the chosen error metric. In such a scenario and if parametric data is available, it may be possible to examine nearby data sets in the parameter space. In the cited example, a Hall thruster exhibited two ion populations at a particular near-pole location when operating at 600 V, 12 kW but exhibited a third ion population at the same location when operating at 300 V, 3 kW. The data suggested that the third ion population may be of different nature than the first two and can be isolated [106].

4.7 Uncertainty Analysis

4.7.1 Statistical Uncertainty in Mean Velocity and Temperature

LIF is typically a fairly noisy diagnostic due to the competition between the laser-induced fluorescence and spontaneous emission from the plasma, in addition to electrical noise sources. With laser powers around 100 mW and phase-sensitive detection integration times on the order of 0.5-1 second, signal-to-noise ratios above 5-10 can readily be achieved for (ground state) ion/atom densities on the order of 10^{16}–10^{18} m^{-3}, typical of the near field of electrostatic thrusters. Note that the noise level will depend not only on the local plasma parameters in the interrogation volume, but also on the line integrated density in the region between the collection optic and the measurement location.

The estimation of distribution moments corresponding to ion velocity and temperature is susceptible to corruption by any noise that survives the lock-in amplification process. In order to quantify the random sources of error and propagate it through complex calculations to the moments of the distribution, Monte Carlo strategies of both numerical and analytical varieties are helpful. A resampling method known as bootstrapping [107, 108] is useful in the case of numerical moment-taking. Data points (ordered pairs of velocity and signal intensity) are randomly sampled from the measured LIF dataset with replacement (i.e., a single measured data point can be included in the set more than once) in order to create a new bootstrap dataset, which contains the same number of points as the original dataset but usually does not include every measured data point. A large number ($\sim 10^4$) of bootstrap datasets are generated, and numerical moments are calculated for each one. The variance in the mean velocity and temperature calculated from the bootstrap datasets approximates the true variance of these parameters in the limit of large sample numbers [109].

A related strategy for determining the uncertainty in the fitting method is to adopt a Bayesian parameter inference approach [21, 67, 110, 111]. We begin by assuming a fitting model $M(v, \theta)$ for the IVDF, where v is the velocity and the model parameters are $\theta = [A, u, T]$ in the example of a Gaussian fit. We also assume a noise model, for example that the measured signal $f(v)$ at a given velocity is normally distributed around the true IVDF value, with some variance σ^2., i.e.,

$$f(v) - M(v, \theta) \sim \mathcal{N}(0, \sigma^2). \tag{24}$$

The goal of Bayesian inference is to leverage Bayes' rule to update a probability distribution $p(\theta)$, representing our prior knowledge about the value of the fitting parameters, into one conditioned on the data d we observe, $p(\theta|d)$. Bayes' rule gives this as

$$p(\theta|d) = \frac{p(d|\theta)p(\theta)}{p(d)}, \tag{25}$$

where the likelihood $p(d|\theta) \propto \exp\left[-\left(f(v) - M(v, \theta)\right)^2 / 2\sigma^2\right]$ is a result of our noise model, and the prior distribution must be chosen as a hyperparameter. A good choice for the prior is a minimally biasing uniform distribution between a range of realistic physical values for each parameter. Finally, $p(d)$ is the marginal probability of all possible datasets known as the ”evidence”, which is a normalizing constant and can typically be ignored. Many off-the-shelf software packages are available for applying Markov Chain

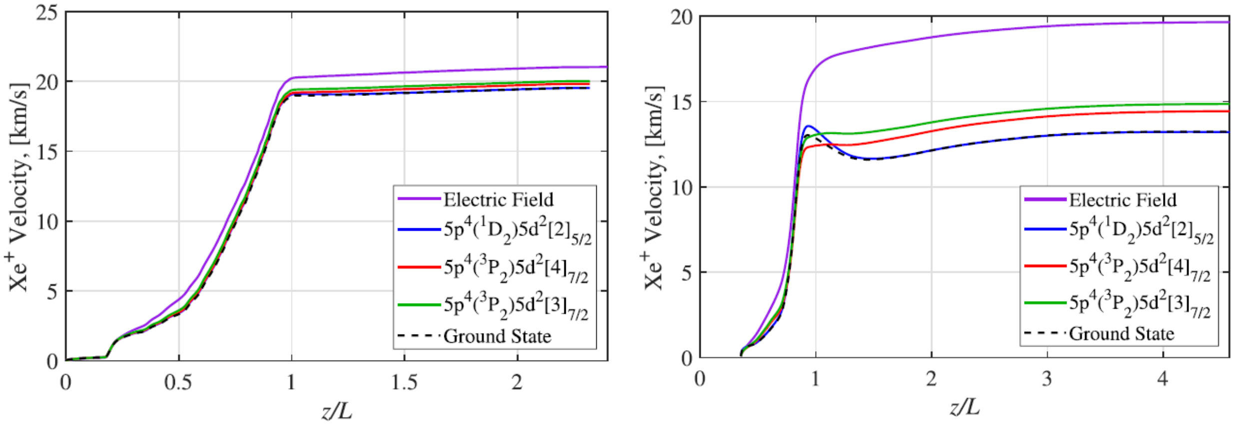

(a)

(b)

Figure 11: Simulated mean velocities along the centerline of the SPT-100 Hall thruster (a) and the HET-P70 Hall thruster (b) of the target metastable states for the Xe II 834.953 nm LIF scheme (red) and the Xe II 605.280 nm scheme (green), compared with the ground state ion velocity and the velocity of a non-metastable excited state (blue). The purple curves show the velocity that would be attained by singly-charged ions starting from rest upstream of the acceleration region, and the x-axis is normalized to the channel length of each thruster. Figures reproduced from Ref. 112 with permission.

Monte Carlo (MCMC) methods to the efficient sampling of these types of probability problems, such as Metropolis Hastings or Hamiltonian Monte Carlo algorithms.

In either case, the end product of these sampling methods is a large vector of mean velocities or temperatures representing the distribution of possible values. These samples can be propagated through further calculations by performing them element-wise and keeping track of statistics on the results, which unlike standard error propagation formulas allows for non-Gaussian probability distributions on the values of downstream calculations. The downside of this is a modest increase in complexity and computational expense to keeping track of larger variables. The experimenter must also, of course, be careful to avoid systematic errors due to the experimental apparatus—an example of this would be reflection of the injected beam off of a thruster surface and back through the focal cone of the collection optic. In this case, the IVDF will be distorted in a systematic way due to the convolution of multiple injection paths.

5 Metastable versus Ground State Ion Velocities

Since single-photon LIF on common EP propellants like xenon and krypton must target transitions out of excited states, it is important to assess whether the VDF of the target state, which typically has a population density $\lesssim 1\%$ of the overall ion or atom density, is representative of the overall VDF for all particles. Minimal discrepancy is expected for non-metastable target states, since they spontaneously decay with a characteristic timescale of ~ 1 μs or faster and must be replenished by electron-impact excitation of ground state ions or atoms. However, for the more common case with a metastable target level, it is not obvious that the measured velocities must always match those of the bulk population. An initial quantitative study of this problem was carried out by Konopliv et al. [112], focusing on LIF measurements targeting the 834.953 nm and 605.280 nm transitions of singly-ionized xenon in Hall thrusters. A collisional-radiative (CR) model built to calculate the populations of Xe II excited states as a function of plasma properties such as electron temperature (T_e) and density (n_e) [30] was combined with a 1D fluid model for ions, and plasma parameters from higher fidelity simulations of several thrusters were used as inputs in order to calculate the mean velocities of metastable and ground state ions as a function of position along the channel centerline.

Figure 11 shows the simulation results for two representative cases. In the flight-proven SPT-100 Hall thruster (Fig. 11a), the Xe II excited states maintain mean velocities similar to that of the ground state ions, with the velocities of the $5s^2 5p^4\left(^3\mathrm{P}_2\right)5d\ ^2[4]_{7/2}$ state (the lower level of the 834.953 nm transition) and the $5s^2 5p^4\left(^3\mathrm{P}_2\right)5d\ ^2[3]_{7/2}$ state (the lower level of the 605.280 nm transition) ultimately exceeding the ground state ion velocity by $\sim$ 300 m/s and $\sim$ 500 m/s, respectively, at the furthest downstream location. All ion states reach a lower mean velocity than would be expected from acceleration by the axial electric field alone because creation of ions from slow neutrals within and downstream of the acceleration region acts as an effective drag force on the ions. While high-energy electron and ion impacts can produce metastable ions directly from ground state neutrals through an ionization-excitation process [113], downstream of the acceleration region this process becomes relatively rare, and the remaining deceleration from charge exchange (CEX) collisions mostly affects the ground state ions, so they end up a mean velocity lower than that of the metastables. This effect is exaggerated in the laboratory Hall thruster shown in Fig. 11b, which does not have optimized ionization efficiency and thus has a much higher neutral gas density in the downstream region that can act as a source of slow ions. Even in this case, the location of the acceleration region can be accurately measured by LIF on metastable ions. Also note that the fluid model in Ref. 112 could only calculate the mean ion velocity, but in reality the ions created by ionization and CEX downstream of the acceleration region would form a low-velocity tail on the IVDF. Therefore, LIF measurements on metastables that focus on the most probable velocity or the mean velocity of the main fast ion population should have high accuracy, while the shape of the low-velocity portion of the measured line profile may deviate from the true IVDF if the neutral density is high.

A different type of IVDF distortion that can occur when targeting metastable states was pointed out by Romadanov et al. 114. These authors found that during large-amplitude breathing mode oscillations of a Hall thruster, the fluorescence signal measured by a high-speed LIF diagnostic targeting the Xe II 834.953 nm transition collapsed to zero during one phase of the oscillation, even though probe measurements showed that the local plasma density was finite at this time. This effect, which was attributed to a large reduction of the electron temperature at this oscillation phase such that the metastable ion state was not significantly populated, could induce errors in IVDFs measured with time-averaged LIF because they would incorrectly weight contributions from different phases of the oscillation.

Part II

Two-Photon Absorption LIF (TALIF)

6 Introduction

While in the previous part of the paper emphasis was put on the measurement of velocity distribution functions, the spatially resolved density of the neutral propellant is another major point of interest in the plasma diagnostic characterization of a thruster. In principle, the intensity of the LIF signal is a measure of the density of the initial state. For single-photon LIF applied to EP devices, as already discussed, the lower level is typically an excited electronic state populated by collisional processes, such that it can not generally be assumed to be in thermal equilibrium. Since the population distribution of states does not follow a Boltzmann distribution, the ground state density (or overall species population) cannot be reliably found from measuring the excited state in the absence of a suitable model. In contrast, since depletion of the electronic ground state due to population of excited states is negligible for typical low-temperature plasma applications, the ground state density can generally be considered equal to the total species density, within the uncertainty of the LIF measurement, for electric thruster plumes.

For widely used gridded ion- and Hall effect thruster propellants, such as xenon, krypton and argon, a single-photon LIF scheme involving the ground state as the lower state would require laser photons in the far or extreme vacuum-ultraviolet region of the spectrum. To avoid such wavelengths, which are difficult to produce from practical sources, two photons can be simultaneously absorbed instead of just one. This approach, known as two-photon absorption laser-induced fluorescence (TALIF) spectroscopy, requires high intensity irradiation as can be most readily generated from short-pulse ($\leq$ 10 ns) laser systems. For the neutrals of xenon and krypton, TALIF excitation schemes can be performed with laser photons above 200 nm, i.e., out of the vacuum ultraviolet. For their respective ions, as well as for some other target species such as argon neutrals, three-photon absorption would be necessary to keep the laser wavelength above the vacuum ultraviolet limit. In contrast to single-photon LIF discussed earlier in this contribution, the need for high intensity is driven by the low absorption cross section and transition probability for n-photon absorption processes, which scale with approximately the n-th power of the laser intensity.

While multi-photon LIF measurements of ground state ions may yet be demonstrated, research has focused heavily on neutral Xe and Kr owing to the relative ease of these measurements and established techniques. These species also have an important role in many processes (and therefore also for model validation). For example, neutral particles are involved in the charge-exchange (CEX) reactions, whereby the collision between a fast (accelerated) ion and a slow (thermal) neutral results in a fast neutral and a quasi-thermal ion. In gridded ion thrusters, these slow ions are generated within the grid assembly, or just downstream from the exit, and are the main driver of grid erosion. As a result of charge exchange, ions may acquire trajectories that strike the grid during extraction, and ions formed just downstream may be back-accelerated in the electric field imposed by the negatively biased accelerator electrode. These surface impingement events may cause significant sputter-erosion of the accelerator grid. Grid erosion during thruster operation over several years is a significant issue for thruster performance and lifetime, and therefore is the subject of extensive experimental and numerical investigation [115–119].

Neutral particles also play a critical role in many aspects of the physics and operation of HETs. Again, neutrals participate in CEX reactions which have direct impact on sputter erosion of the insulator channel (device lifetime) [120]. The distribution of neutrals in the near plume also directly influences the ingestion of background gas into the thruster, which in turn influences the achieved thrust and anode efficiency (so called neutral ingestion effect) [121]. The former point is an example of a facility effect, i.e., the mismatch of the thruster test environment between terrestrial chamber testing and in-space operation, which is a problem of increasing importance particularly for high-power thrusters [122]. Another facility effect related to neutrals, which can be studied via TALIF, is the varying neutral density field that results from the location and design of pumping systems in the vacuum chamber, as well as due to particles reflecting (scattering) off chamber walls (which in some cases causes particles to be directed back to the thruster) [123]. In terms of HET oscillations, neutrals play a prominent role in the (so called) breathing mode oscillation, which is driven by a predator-prey ionization instability inside the discharge chamber. As fractional ionization of neutral species rises it eventually causes collapse of the discharge, with recovery occurring as propellant flow re-establishes sufficient neutral density (the elapsed time for these processes determines the oscillation frequency). The use of temporally-resolved TALIF to study these oscillations in HETs is a relatively recent development, discussed in Section 11.

Long optical pathways of the experimental setup due to large-scale vacuum facilities, the very small particle densities in the thruster plume and elsewhere, and the often strong competing plasma luminosity, are among the challenges for use of TALIF in EP diagnostics. In the following sections of the paper, theoretical and experimental aspects of TALIF spectroscopy are discussed, with emphasis on recommendations derived from investigations of HETs [124–126] and gridded ion engines [127–133].

7 Theory

7.1 Rate equation model

The TALIF process consists of the state-selective simultaneous absorption of two laser photons to populate an excited level of the atom or molecule of interest, and the observation of the subsequent fluorescence from the excited level. The quantitative treatment of the TALIF process, and multi-photon absorption in general, have been extensively described in the literature [134–138]. A very brief summary of this topic, following Bamford et al [134], is given here. As for single-photon LIF, it is common to formulate a set of rate-equations for the number densities (populations) of the energy levels involved:

$$\begin{aligned} \dot{n}_0(r,z,t) &= -\sigma^{(2)}\Phi^2(r,z,t)n_0(r,z,t) \\ \dot{n}_2(r,z,t) &= \sigma^{(2)}\Phi^2(r,z,t)n_0(r,z,t) - (A+Q)n_2(r,z,t). \end{aligned} \tag{26}$$

where n_0 and n_2 are the number densities of the lower (initial) level (i.e. the ground state for most TALIF studies) and the two-photon excited level, respectively. Here A and Q are the de-excitation rates by spontaneous emission and collisional deactivation (quenching), respectively, and $\sigma^{(2)}$ is the two-photon absorption cross section. Note that A is the sum of the radiative transition rates over all fluorescence channels out of the two-photon excited level. The photon flux $\Phi(r,z,t)$ may be written in terms of the intensity $I(r,z,t)$, the temporal laser profile $F(t)$ and the spatial laser profile (fluence) function $H(r,z)$:

$$\Phi(r,z,t) = I(r,z,t)/\hbar\omega = F(t)H(r,z)/\hbar\omega \tag{27}$$

The rate equations may be solved using the standard method of variation of parameters. Assuming that the ground state population is invariant over the spatial extent and time duration of the measurement, its depletion due to the excited state population is negligible ($n_0(r,z,t) \equiv n_0 = \text{constant}$) and the laser pulse width is significantly smaller than the effective lifetime of the excited state ($\tau_p \ll \tau_{eff} = 1/(A+Q)$), the number of photons emitted per unit volume integrated over time is

$$\begin{aligned} n_{\hbar\omega}(r,z,t\to\infty) &= A_{21}\int_{-\infty}^{\infty} n_2(r,z,t)\mathrm{d}t \\ &= \frac{A_{21}\sigma^{(2)}n_0H^2(r,z)}{(A+Q)(\hbar\omega)^2}\int\limits_{-\infty}^{\infty} F^2(t)dt \end{aligned} \tag{28}$$

for the observed fluorescence channel with Einstein coefficient A_{21}. Assuming further a Gaussian spatial laser profile and using the standard formulae for laser beam evolution:

$$H(r,z) = \frac{2E}{\pi a^2(z)}e^{-2r^2/a^2(z)}, \qquad a^2(z) = a_0^2\left[1+\left(\frac{z}{z_0}\right)^2\right] \tag{29}$$

where E denotes the laser pulse energy, z_0 the Rayleigh length and a_0 the beam waist at the focus point, spatial integration of eq. 28 yields the total number of emitted photons on the selected fluorescence channel:

$$N_{\hbar\omega} = \frac{A_{21}}{A+Q}\frac{\sigma^{(2)}N_0LE^2}{\pi a_0^2(\hbar\omega)^2}\int\limits_{-\infty}^{\infty} F^2(t)dt \tag{30}$$

where it has been assumed that the length L of the detection volume is small compared to the Rayleigh length, and the beam waist can be regarded as constant. It is convenient to define the detected signal intensity, S, as:

$$S = \frac{1}{4\pi}\frac{N_{\hbar\omega}D}{L} = \frac{A_{21}}{A+Q}\frac{\sigma^{(2)}n_0DE^2}{4\pi^2a_0^2(\hbar\omega)^2}\int\limits_{-\infty}^{\infty} F^2(t)\mathrm{d}t. \tag{31}$$

Here, the calibration constant D has been introduced, which accounts for all relevant parameters related to efficiencies, sensitivities and the geometry of the experimental apparatus. If the absolute particle density is to be measured, various calibration approaches can be employed as described in Section 9.5, see also reference [135]. When collisional quenching rates are much smaller than for spontaneous emission, as is typically the case in electric propulsion applications where particle densities (pressure) are low, the term $A_{21}/(A+Q) \approx A_{21}/A$ reduces to the branching ratio of the selected fluorescence transition.

The relation $S \propto E^2$ in Eq. 31 is characteristic of the unsaturated TALIF process. Note that this square law (as well as Eq. 31) may not apply if additional processes influence the level populations. Examples for such processes include Resonance-Enhanced Multiphoton Ionization (REMPI), where a two-photon excited state is ionized by another laser photon before it is de-excited by spontaneous emission, and Amplified Spontaneous Emission (ASE), where the fluorescence emission becomes strongly non-isotropic with a preferred direction along the laser beam propagation axis. For an overview of these phenomena, see e.g. reference [139]. REMPI and ASE contributions become significant when the laser energy is increased above a certain threshold. For Xe and Kr at EP conditions, as compared to low-Z atoms, relatively low threshold energies have been reported [140]. Note that quantitative TALIF spectroscopy can still be performed under partial saturation conditions, where these additional processes play some role, and fully saturated as long as there remains a signal dependence of S on n_0 [141].

7.2 Absorption Lineshape Profile

The signal intensity must include a contribution stemming from the spectral profile of the absorption line and probe laser. In literature, it is common to include this dependence within the definition of the two-photon absorption cross section:

$$\sigma^{(2)} = \sigma^{(2)}(\omega) = \sigma_0^{(2)} g(\omega) G^{(2)} \tag{32}$$

where $g(\omega)$ is the normalized lineshape function and $G^{(2)}$ is the photon statistic factor.

For many applications the natural linewidth of the two-photon transition is much smaller than the Doppler width and is therefore neglected. Pressure broadening tends to be negligibly small at EP conditions. Neglecting any isotope shift, hyperfine splitting or other potential broadening contributions, the lineshape function is the convolution (denoted by the * symbol) of the Doppler profile and laser lineshape which, for two-photon absorption, is given by [135, 136, 142]:

$$g = g_D * g_L * g_L. \tag{33}$$

If the spectral laser profile is Gaussian like the Doppler profile, then $g(\omega)$ is also Gaussian and the resulting full-width at half maximum (FWHM) is

$$\Delta\omega = \sqrt{\Delta\omega_D^2 + 2\Delta\omega_L^2} \tag{34}$$

where $\Delta\omega_D$ and $\Delta\omega_L$ are the FWHMs of the Doppler and laser (Gaussian) lineshapes respectively. However, in some cases the lineshapes of sources used for TALIF may be better described by Lorentzians (e.g., in [140] where the profile is determined by the short pulse duration which allowed for very few resonator passes) in which case the final lineshape will be a Voigt profile and, instead of Eq. (34), the relation between Doppler and laser linewidths has to be modeled differently (see e.g. [143, 144]).

As discussed relative to signal levels above, additional factors associated with laser saturation may affect the measured line profile. When REMPI becomes active the fluorescence signal intensity will generally asymptote as laser energy increases [145]. REMPI has been demonstrated to have almost no influence on the TALIF linewidth if the exciting laser pulse is coherent [146]. This finding may not hold for multi-mode laser sources, when the detection volume consists of spatial parts that are saturated by REMPI and other parts that are not. Another channel could be ASE, which has a strong directional dependence (propagation along the laser beam axis), and might be the reason for the low saturation thresholds observed for xenon or krypton [140]. However, for the formation of ASE, thresholds for the particle densities need to be exceeded [147], which may not be reached in low-density EP applications. Significant ground state depletion, if present, also affects the TALIF signal intensity. Apart from saturation, pressure broadening, which is relevant in applications such as atmospheric plasma jets, plays only a minor role at typical low-density EP relevant conditions.

7.3 TALIF Schemes

The selection of a workable TALIF scheme – meaning transition wavelengths to be used for excitation (the laser source) and fluorescence (detection) - for measurements in EP devices or their plumes is driven by many considerations including the relatively low particle densities typical found in these experiments. An "efficient" TALIF scheme therefore primarily relies on large transition probabilities for the two-photon absorption and/or the emitting fluorescent transition. In addition, there are several additional factors that may be considered, such as the availability and pulse energy of laser source at the needed wavelength (typically pulsed lasers with second harmonic generation crystals), the quantum efficiency of the detector, and the intensity of the plasma emission at the fluorescence wavelength (due to possible measurement interference).

Energy levels that can be excited from the ground state must follow the two-photon absorption electric dipole selection rules [148] which, for atoms as well as molecules with a center of symmetry, require transitions between states of matching parity (in contrast to one-photon absorptions which connect states of opposite parity). For the energy levels of rare gas neutrals such as xenon and krypton, the $nl[k]_J$ notation is commonly used [149]. Here, n and l represent the principal quantum number and the orbital angular momentum quantum number of the valence electron, respectively. The quantum number k is attributed to the vector addition of the orbital angular momentum of the valence electron and the total angular momentum of the core electrons. The prime symbol distinguishes two angular momentum configurations of the core electrons. J is the quantum number of the total angular momentum including all core electrons and the valence electron. Since xenon and krypton neutral ground states have total angular momentum $J = 0$, the excited state may have $J = 0$ or $J = 2$ and must have even parity.

From Eq. 28 the detected fluorescence intensity will increase with both the absorption cross section of the two-photon transition and the branching ratio of the fluorescence transition used. While for xenon and krypton the branching ratios are well tabulated [151, 154], data on the two-photon absorption cross sections, especially based on measurements, is still relatively rare. Some possible TALIF schemes with known transition rates are summarized in Table 3. Two TALIF schemes which have been used in recent investigations are shown in Fig. 12, however, it is emphasized that other schemes may be preferred depending on the detailed design and conditions of the experiment. For xenon, excitation of the lower energetic $6p$ multiplet may be a good alternative, although plasma emission background from these levels may be more intense. For argon neutrals, two-photon excitation from the ground state requires a vacuum ultraviolet wavelength well below 200 nm, which is difficult or impossible to generate with adequate pulse energy, and the beam line must be in vacuum. The situation is the same for ions of xenon and krypton.

8 TALIF Experimental Setups

Here we describe typical experimental setups, with best practices and suggestions, for EP TALIF diagnostic studies. To ground the discussion, we will focus on experimental campaigns directed at gridded ion thrusters (GITs) and Hall effect thrusters (HETs), but similar approaches can be used for related studies of other components or thruster types. We discuss the setups starting with the laser source, followed by delivery to the test article, and finally signal collection and data acquisition.

Neutral	λ_{exc} (nm)	excited level	$\sigma_0^{(2)}$ (10^{-43}m^4)	λ_{flc} (nm)	final level	branching ratio	EP application in Ref.
Xe	2×222.6	$6p'[1/2]_0$	1.88^a [150]	788.7	$6s'[1/2]^\circ_0$	0.62 [151]	[124, 128, 130]
Xe	2×224.3	$6p'[3/2]_2$	1.36^b [150], $2.5^{c,d}$ [140]	834.7	$6s'[1/2]^\circ_1$	0.733 [151]	[131–133]
Xe	2×225.5	$7p[3/2]_2$	$0.48^{c,f}$ [136]	462.4	$6s[3/2]^\circ_2$	0.373 [151]	[127]
Xe	2×249.6	$6p[1/2]_0$	5.0^e [152]	828.0	$6s[3/2]^\circ_1$	0.998 [151]	-
Xe	2×252.5	$6p[3/2]_2$	1.7^e [152]	823.2	$6s[3/2]^\circ_2$	0.7 [151]	-
Xe	2×256.0	$6p[5/2]_2$	2.9^f [152]	904.5	$6s[3/2]^\circ_2$	0.363 [151]	-
Kr	2×204.2	$5p'[3/2]_2$	3.25^g [153]	826.3	$5s'[1/2]^\circ_1$	0.953 [154]	-
Kr	2×212.6	$5p[1/2]_0$	23.6^g [153]	758.7	$5s[3/2]^\circ_1$	0.981 [154]	[125, 126, 129, 130]
Kr	2×214.8	$5p[3/2]_2$	4.18^g [153], 5.2^h [155]	760.2	$5s[3/2]^\circ_2$	0.712 [154]	-
Kr	2×216.7	$5p[5/2]_2$	6.33^g [153]	877.7	$5s[3/2]^\circ_1$	0.693 [154]	-

Table 3: Some TALIF schemes including data on transition probabilities. Data for some additional $7p$ levels in xenon can be found in [156], where relative measurements are reported.

[a] Uncertainty $+0.75/-0.54$.

[b] Uncertainty $+0.46/-0.34$.

[c] Measured relative to the two-photon excitation of the $3p\,^3P_{2,1,0}$ levels in atomic oxygen, for which the two-photon absorption cross section of 1.33×10^{-43}m^4 has been found [134]. Uncertainty given for the relative measurement.

[d] Uncertainty 20%.

[e] Uncertainty 30%.

[f] Uncertainty 50%.

[g] Calculated numerically using hybrid quantum defect theory/oscillator strength method, see [153] for uncertainty.

[h] Uncertainty ±2.2.

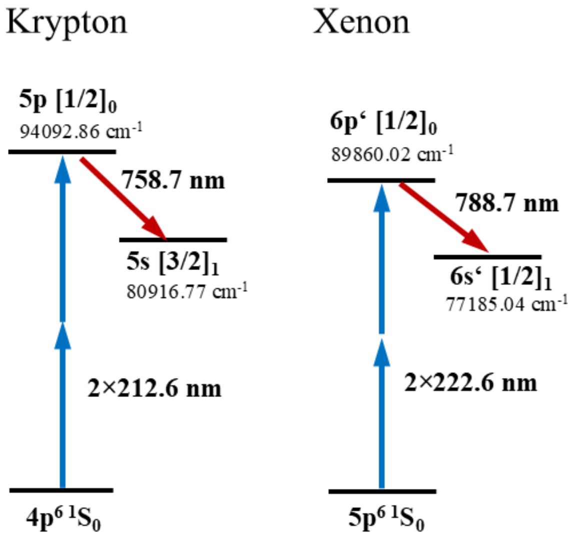

Figure 12: Two common TALIF schemes for detection of neutral xenon and krypton.

8.1 Laser Source

As discussed above, EP TALIF studies have concentrated primarily on Xe and Kr, and in both cases the wavelengths used for laser excitation are in the $\sim 205-250$ nm range. Relatively high laser pulse intensity is required due to the weak two-photon absorption cross-sections, therefore studies have employed pulsed lasers, usually either tunable dye systems or optical parametric oscillators (OPOs). In each case a Nd:YAG laser, frequency doubled to 532 nm or tripled to 355 nm, is the common pumping source. The output of the dye laser or OPO system is then converted with a nonlinear crystal or crystals via harmonic generation and/or frequency mixing to obtain the TALIF laser beam. Pulse energy is significantly reduced at each successive stage. As specific examples, corresponding to the schemes of Fig. 12, Kr can be accessed by pumping a dye laser (Exalite 428 dye) with the 355 nm Nd:YAG output to produce a dye fundamental wavelength of ~ 424 nm which is then frequency doubled to ~ 212 nm [157], or Xe can be similarly accessed by operating the dye laser at ~ 445 nm (Coumarin 120 dye) and doubling to ~ 222 nm [130].

Typical output in the $200-225$ nm range is $\sim 1-10$ mJ energy per pulse with $\sim 5-15$ ns pulse duration (primarily determined by the Nd:YAG pump) at repetition rates of $10-30$ Hz (though use of higher repetition-rate lasers, including burst mode lasers, may provide a future research direction). While typical peak pulse powers of ~ 1 MW promote high TALIF signal levels, which is nominally desirable, tight beam focusing (to beam waist $\lesssim 100\mu$m) can readily produce power saturation. Because saturation can reduce the signal and/or complicate signal dependence it can be desirable to avoid saturation by using a weaker focusing optic or by making the TALIF measurement at a location away from the waist.

Although most EP studies have not employed injection seeded Nd:YAG lasers as can modestly increase pulse energy, smooth the temporal profile, and significantly narrow the linewidth of the pump laser. These characteristics, in turn, improve the output of the tunable source being pumped. Typical final linewidths used for TALIF vary considerably but are commonly in the range of a few pm (~ 10 GHz). If the FWHM of the Doppler profile is much less than the laser profile, as is often the case in EP related TALIF research to date, the ability to infer (deconvolve) the Doppler profile from the measured signal (see Eq. 33) is severely limited. In addition, species like xenon can have hyperfine structure (although not for $J = 0$ levels) and isotope shifts (small in comparison to typical hyperfine structure) that complicates and slightly broaden the profile [158]. Regarding laser wavelength control, some TALIF experiments “scan” (tune) the laser wavelength over the full transition spectrum while others, to enable more efficient data collection across plasma conditions or spatial positions, “park” (fix) the laser wavelength at the peak frequency of the TALIF lineshape. In the latter case, the peak signal can be found by first scanning the laser over the full transition

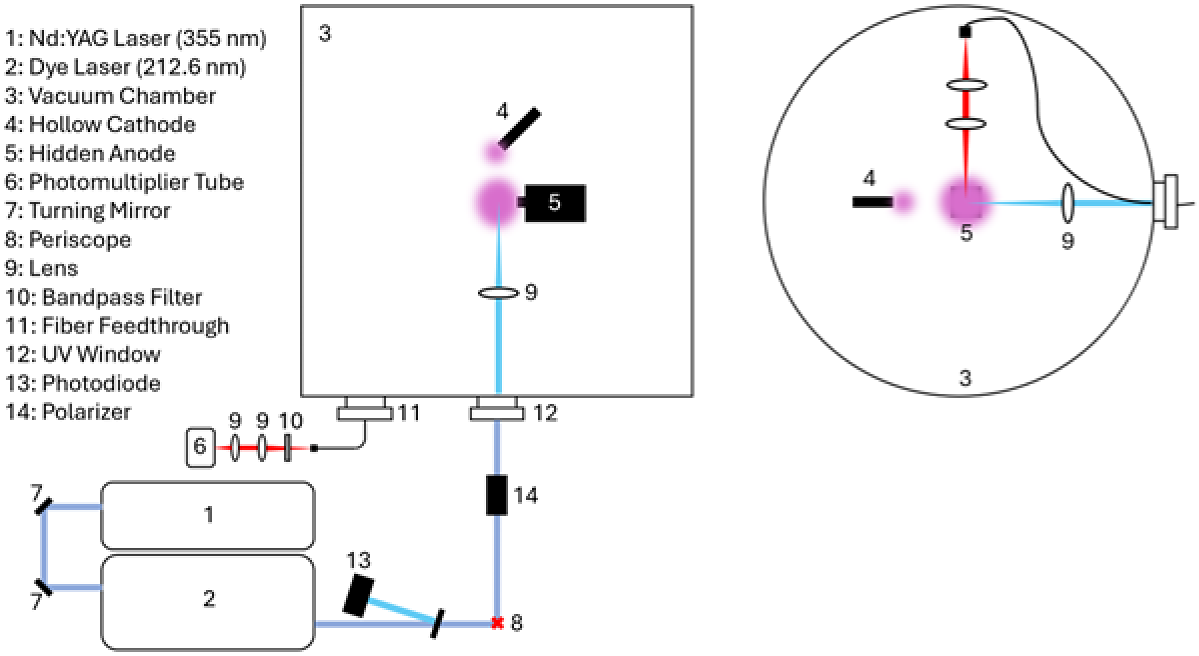

Figure 13: Experimental setup for TALIF measurement in plume of a plasma device (hidden anode shown here) [125].

while other methods include use of an additional TALIF reference leg (where a small fraction of the beam is split off and directed to a stationary gas reference cell, containing low density Xe or Kr, and TALIF is conducted, e.g., [124]). As with other pulsed laser diagnostics, additional reference monitoring can be performed to measure laser pulse energy with a photodiode or laser frequency with a wavemeter (serving a similar purpose as a gas reference cell and with tradeoff depending on the achievable resolution).

8.2 Laser Beam Delivery

The delivery of the probe beam to the measurement environment, and collection of the fluorescence signal can be configured in different ways. Figure 13 provides an example TALIF configuration similar to that used in past studies of a 1.5 kW HET [125]. In the configuration shown in Figure 13, a 212 nm beam from a frequency-doubled dye laser is used for TALIF of a hidden anode (but HET or GIT or other articles could be studied similarly). The source beam is delivered to the chamber via a series of mirrors, including a periscope to elevate the beam line, passing into the chamber through an ultraviolet (UV) grade fused silica window and weakly focused by a plano-convex lens with 50-cm focal length. While beam delivery is relatively straightforward it should be noted that the peak power (~ 1 MW) can be damaging to components. Dielectric mirrors with appropriately high damage thresholds, or UV fused-silica turning prisms, are generally used. The high beam power also generally precludes fiber optic delivery of the probe laser to within the chamber (which would be convenient if possible). Experiments have generally used relatively slow lenses to obtain $0.1-1$ mm multimode beam waist diameter.

As was noted in the Theory section, because TALIF, unlike LIF, is a non-linear technique, the beam diameter (intensity) at the measurement location influences signal levels and power saturation. In some cases the beam waist is placed at the measurement location (defined by the intersection of the laser beam and collection optics focal location) while in other cases it is preferred to measure at a location away from the waist where the beam is partly defocused (to avoid signal reduction by saturation) [124]. From a practical perspective, the focusing lens should not be too proximate to the plasma to avoid perturbing it, but also to better protect the mirror from damage due to sputtered particles or intense UV light, with typical standoff distances being 50 cm – 1 m. Depending on conditions, any in-chamber optics (including the window) can be damaged over time and may be covered with protective plates (when not in use) and/or need to be periodically cleaned. Of course, the requirement to use relatively long focal length lenses can be challenging in terms of maintaining exact alignment, both between the probe laser and thruster as well as between probe laser and collection optics. The latter tends to be more critical and one possible approach to mitigate this is given below.

8.3 TALIF Light Collection

Figure 13 also shows typical collection optics for a point (0-D) measurement in the thruster plume. In this case, the TALIF signal, along with the plasma's luminous emission (including at the TALIF detection wavelength), is collected and collimated by a 5 cm diameter, 30 cm focal length plano-convex lens at an angle perpendicular to the probe beam. The collected light is focused into a multimode optical fiber with a core diameter of 0.6 mm by a 5 cm diameter 15 cm focal length plano-convex lens. Similar concerns as for the beam delivery optics apply to these optics, i.e., they should not be too proximate to the plume and they may be damaged by sputtering (a protective wrap or casing should be used). Collection optics of larger diameter, to gather a higher solid-angle fraction of the fluorescence, will boost the TALIF signal. Alternatively, fluorescence can be collected below with a large spherical mirror rather than a lens, and beamed toward the detection system. Practical limits exist with respect to collection optic size, minimum focal length, quality, expense, and proximity to the laser interaction region. In either case, focusing the collected light into an optical fiber or through a slit improves the spatial definition of the probe region and reduces the detected noise level from background emission. For the imaging train shown in Figure 13 the magnification factor is 0.5 and the resulting cross sectional area at the collection location (waist of the 212 nm probe beam) is a circle with 1.2 mm diameter. Because the collection area is roughly an order of magnitude larger than the probe laser waist, there is resilience against micro-movements of the beam delivery and collection optics during chamber evacuation and heating, and signal is increased because fluorescence is obtained along 1.2 mm of laser propagation.

The collected light is coupled out of the vacuum chamber, via a bulkhead mounted feedthrough, where it is typically passed to a second fiber optic that delivers the light to the final photodetector. Most experiments use photomultiplier tubes (PMTs) for detection of the weak TALIF light along with bandpass filters (with bandpass $\sim 2-10$ nm) to remove any ambient light along with plasma emission from other emission lines. Details of the filter selection are important in terms of achieving maximum transmission of the desired TALIF emission line while mitigating contributions from other, often spectrally close, emission lines that emit interfering light. Data collection from the PMT can be handled as in other laser diagnostic experiments. The actual TALIF signal is due to the two-photon excitation followed by spontaneous emission and so has typical time duration ("exponential-tail") of ~ 100 ns (depending on the lifetime of the upper state, lifetimes for Xe and Kr levels been tabulated extensively in literature, e.g. in [151, 154, 159, 160]).

The TALIF signal typically rides on a non-zero baseline (due to the abovementioned plasma luminosity) that should be subtracted and then the (time-integrated) area of the resulting signal PMT trace yields the TALIF signal. The PMT signal can be acquired by a variety of methods including via an oscilloscope connected to a computer, or directly with a suitable fast DAQ card to computer, or with a boxcar integrator for analogue analysis.

A boxcar is often used to integrate the time-dependent fluorescence signal during a defined window of time following each laser pulse. If the plasma emission signal is monitored with a second boxcar, and the integration window coincides with a period between pulses during which there is no fluorescence, this baseline can be subtracted from the signal output of the first boxcar, eliminating the plasma emission noise from the TALIF signal to first order.

Some setups do not use optical fibers for light collection but instead use lenses to directly image the detection volume (through an appropriate window in the vacuum facility) on the sensor area of the PMT. In this case, the PMT is usually equipped with a narrow entrance slit or a pinhole aperture [130], or is attached to the back end of a monochromator with entrance and exit slits of variable width. The latter approach is an effective way to simultaneously reduce the spectral acceptance bandwidth and improve the spatial resolution, with continuous (but not independent) control over each. A narrow band filter and slit combination performs a similar function, without continuous control, and may be more limited in ability to reduce the acceptance bandwidth.

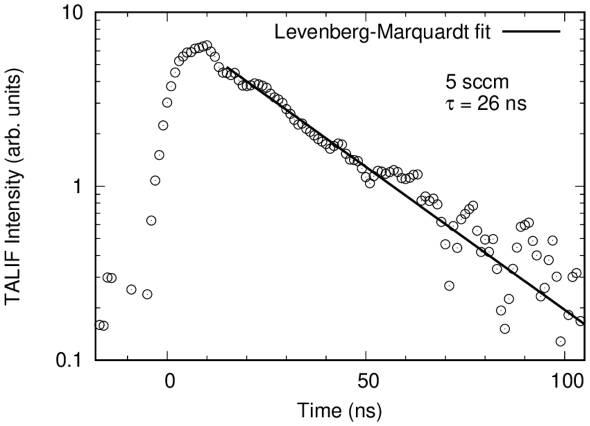

Figure 14: Time-resolved fluorescence signal after excitation of the $5p[1/2]_0$ level in Krypton, measured in the plume of a RIT-10 thruster, accumulated over 3000 laser pulses [129].

9 Measurement and Data Analysis

9.1 Preparatory Steps for Characterization of TALIF System

In contrast with most LIF for EP, TALIF measures ground states such that plasma generation is not required for detection of signal. This aspect can be useful to “find the signal” prior to thruster operation and to enable system optimization or calibration. In particular, the TALIF experimental apparatus can be tested and optimized in a cold gas environment including possibilities of measuring the test-article under “cold-flow” (plasma-off) conditions, ”flooding” the overall vacuum chamber at static conditions, or using a reference cell located at the probe region of interest. Pre-measurements with an artificially increased particle density might be very helpful, for example, to optimize the spatial alignment of components in setups where the detection volume is imaged onto a small PMT entrance aperture.

Performing temporal analysis of the fluorescence signal collected with a fast oscilloscope can also be helpful as a means to examine and optimize triggering and integration-window settings depending on the acquisition method used. Especially in the presence of strong plasma emission at the wavelength of the selected fluorescence transition, an accurate positioning of the integration gate (and its width) may have considerable influence on the signal-to-noise ratio. Note that, as the triggering takes place on the nanosecond timescale, any changing of cable lengths (for example by changing the number of preamplifier stages) may have an immediate effect on the signal integration timing. An example fluorescence curve, as would be obtained from a fast oscilloscope or DAQ system is shown in Fig. 14 including use of a single-exponential decay to extract the (natural) lifetime of the excited state.

9.2 TALIF Measurement

The TALIF signal can be collected on an individual shot basis, or by averaging multiple laser shots, but in either case, accumulation of a relatively large number of shots is often needed to attain reasonable signal-to-noise levels (due to the combination of relatively low particle densities that are typically $\sim 10^{10} - 10^{14}\,\mathrm{cm}^{-3}$, the weak two-photon absorption cross-section, and interfering plasma luminosity). Typical experiments may collect $\sim 100 - 5000$ laser shots (at a given condition) which can take from 10s of seconds up to even a few minutes for typical laser repetition rates of 10 Hz.

As mentioned, measurements can be performed by scanning the laser wavelength across the transition, which records the full lineshape but is time intensive or by fixing “parking” the laser at the spectral peak of the absorption line. Of course, in the latter case one forgoes information of the full absorption line profile and needs to be careful both the laser does not drift off the peak and that the spectral width and shape is unchanged over the series of measurements (since, if it does, peak measurements alone are inadequate for density analysis). Note that small drifts of the laser wavelength due to thermal effects may have considerable

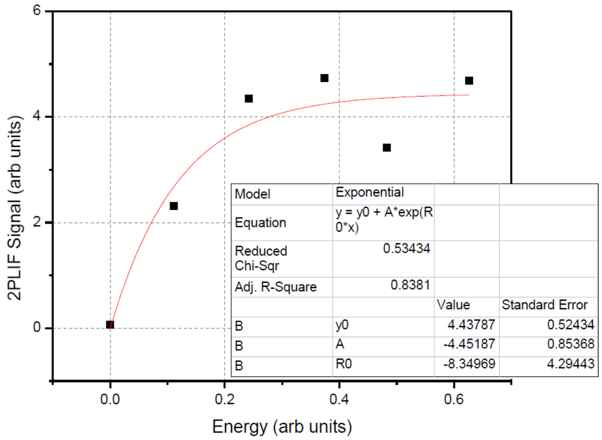

Model	Exponential		
Equation	y = y0 + A*exp(R0*x)		
Reduced Chi-Sqr	0.53434		
Adj. R-Square	0.8381		
		Value	Standard Error
B	y0	4.43787	0.52434
B	A	-4.45187	0.85368
B	R0	-8.34969	4.29443

Figure 15: Measurement of the TALIF signal intensity in dependence of the laser pulse energy as shown in [124].

influence on the detected signal intensity. The user is advised to minimize uncertainties relying on such effects, for example by repeating selected measurements to analyze potential drifts, or carrying out full spectral scans whenever it might be necessary. Additionally, changes in the plasma emission bias (for example according to different spatial measurement positions) need to be recorded and extracted separately, either from the oscilloscope data or a second appropriately timed boxcar integrator.

9.3 Saturation

As summarized above, saturation complicates the quantitative interpretation of TALIF signals. Therefore, the signal dependence on pulse energy is important to characterize, so that any energy difference between thruster-based and known density measurements (e.g. for density calibration) can be accounted for. The general test to identify which pulse energies correspond to saturated or unsaturated energy ranges consists in a check of the $S \propto E^2$ relation. An example measurement of this dependence is given in Figure 15.

A pragmatic approach, if saturation cannot be reliably excluded, is to check that the TALIF signal is linear with the particle density, i.e., $S \propto n_0$, at a fixed laser energy for a fixed focus geometry in a separate experiment, and maintaining this laser energy also in a reference measurement for absolute density calibration. Effects of varying the laser pulse energy may also be included, but proper energy normalization requires first mapping out the TALIF signal dependence on laser energy to characterize possible signal saturation [141]. If, for example, the pulse energies are such that the TALIF signal is linear with energy then dividing the recorded TALIF signal by the pulse energy gives appropriate normalization. On the other hand, if the experiment is fully in the saturated regime there will be little energy dependence and little need to normalize.

9.4 Spectral Lineshape

The spectral lineshape profile obtained in the unsaturated TALIF regime is given by the convolution in eq. (33), which results in a Doppler, Lorentzian or Voigt (mixed) profile, depending on whether the Doppler species profile or Lorentzian laser profile is dominant, or their contributions are comparable. Here we assume that the pulsed laser spectral output is Lorentzian, as it normally is for TALIF laser sources. An example lineshape profile, fitted to a Gaussian function, is given in [124], and a fitted Voigt profile for the same Xe transition to the $6p'[1/2]_0$ upper level, using a different laser source (and different thruster) can be found in [128]. The influence of saturation, depending on the processes involved, can broaden the absorption line, but its contribution is normally small compared to the target species Doppler and laser line widths.

The Heisenberg uncertainty principle imposes a lower limit on laser spectral linewidth, determined by pulse duration. While cw-lasers used for LIF tend to have more narrow linewidths (down to MHz level and below), most TALIF work uses pulsed lasers with spectral linewidths that preclude TALIF lineshape analysis to infer bulk velocity (from Doppler shifts) or other plasma parameters. When the TALIF laser linewidth is sufficiently narrow, however, it is possible to accurately measure Doppler shifts. The Doppler profile for each hyperfine and isotopic shift component is essentially identical, with constant relative intensity, so any frequency shift of the peak of the profile is a direct reflection of a shift in the most probable velocity. An example of Doppler shifts observed with TALIF applied to an HET is shown in Figure 16. In this case, the Nd:YAG laser was injection seeded and the assumed (unmeasured) Gaussian profile width of the tunable dye laser output at 600 nm was FWHM ~ 0.04 cm^{-1} (as suggested by manufacturer's specifications). The 355 nm Nd:YAG profile, generated by mixing a doubled (532 nm) Nd:YAG beam with the 1064 nm fundamental, was then mixed with the tunable dye output in a nonlinear crystal. The linewidth may change at each stage of conversion, such that it is desirable to directly measure, but this is seldom done, especially at wavelengths well into the ultraviolet spectrum. For the measurements in Figure 16 the laser linewidth was therefore unknown. The Doppler width for the 89860.02 cm^{-1} xenon atom transition $6p'[1/2]_0$ was estimated to be 0.16 cm^{-1} at 800 K (neglecting contributions from hyperfine structure, isotopic shift effects, power broadening and so on. Figure 16 displays the relative frequency of the 600 nm scanning laser, therefore the frequency change for the two-photon transition is double, and the observed average profile width (FWHM $\sim 2 * 0.14$ cm^{-1}) is considerably more broad than the estimated Doppler width for this temperature. Similarly, the magnitude of approximately equal and opposite Doppler shifts observed at inside and outside edges of the discharge channel suggests the neutral xenon atoms are strongly hyperthermal (effective temperature exceeding 2000 K) as they leave the thruster. For this case, finding the peak signal at one spatial location and fixing the laser frequency there while attempting to map density throughout the plume would introduce considerable error due to Doppler peak shifting. A full scan at each location is preferred.

Deconvolving the hyperfine and isotopic shift structure, and laser frequency profile to accurately obtain the Doppler profile of the propellant species can be a very challenging task, unless there is good data on the spectral profile of the laser. However, for this example the laser linewidth and other factors appear to be minor contributors in comparison to the Doppler profile of xenon neutrals.

9.5 Calibration

With regard to signal quantification, in some cases TALIF data are reported in arbitrary units (still allowing spatial maps or temporal trends to be observed), while in other cases absolute densities are reported via signal calibration. The absolute density for typical propellant species such as xenon and krypton can be obtained through the comparison of signal amplitude for in-situ measurements. One approach relies on the ability

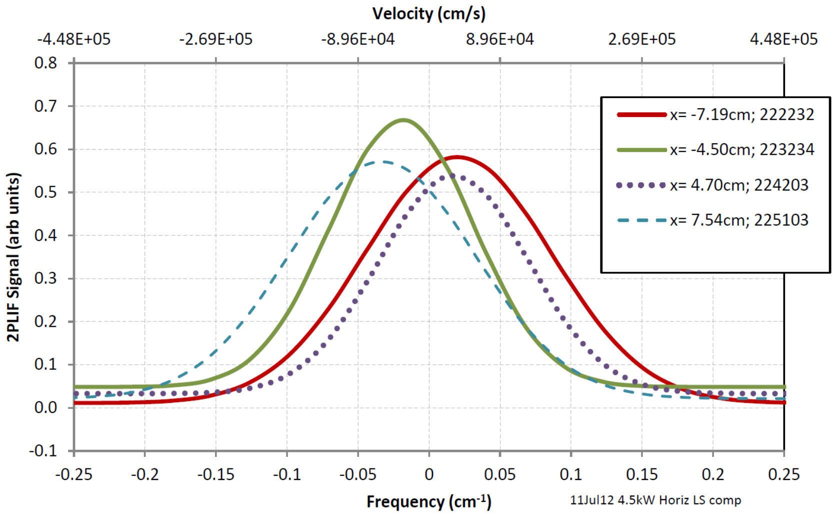

Figure 16: Fitted spectral profile results for TALIF data near the SPT-140 exit plane, for inner and outer channel edges showing the Doppler shift of most probable velocity (see [124]).

to establish a known density in the vacuum chamber and use the same setup for thruster measurements to determine the signal amplitude that corresponds to the known density. For this approach a calibrated means of determining the density is required, as is commonly done with an ion gauge verified against a certified instrument with NIST traceable calibration. The density must be the same at the ion gauge as it is in the laser interaction region. To ensure this is the case there should be no in-flowing gas at the time of measurement, minimal temperature difference between these locations, and relatively slow vacuum pumping so that a significant density gradient cannot exist. For a typical vacuum chamber situation this means turbopumps and small cryopumps can be operational, but preferably not large cryopumps [161]. It is also preferred that the ion gauge and laser interaction region are as close as possible, and that most of the surface area inside the chamber is at ambient temperature rather than cryogenic. In most cases the ion gauge will be wall mounted, with its temperature roughly ambient (although somewhat elevated due to filament heating). The TALIF signal can be measured over a range of density, so that a plot can be made with least squares fit to improve the accuracy. Signal dependence on pulse energy should be measured as well, so that any energy difference between thruster-based and known density measurements can be accounted for. If the laser linewidth is broad compared to the transition Doppler width, any difference in temperature will have little effect. If the laser linewidth is narrow in comparison, then each relative or absolute density measurement should be made by scanning the laser frequency across the entire transition Doppler profile and integrating the result. If performed appropriately, absolute accuracy on the order of 20% should be achievable for this means of density determination.

A second approach for determining absolute density is to compare hot flow results during thruster operation with ambient flow results. Ambient flow (or cold flow) means the thruster is not operating, and thruster wall temperature is near ambient (room temperature) conditions. Here the flow rate through the thruster is known, calibrated against an absolute standard, and at least for the ambient flow case the measurement is made as near to the exit plane as possible. From the exit area of the thruster, flow rate and assumed axial velocity at the exit plane, the density is readily calculated. The above comments about laser linewidth apply here as well. Divergence effects and uncertainty in the mean axial velocity and density variation across the exit, limits the accuracy of this approach. This is especially true if the device employs a flow restriction with significantly elevated backing pressure, since propellant velocity may be hyperthermal even under cold flow conditions. A good computational simulation of the exiting particles may provide improved results. In any case, the accuracy of this approach likely tends to be somewhat lower than the method previously discussed.

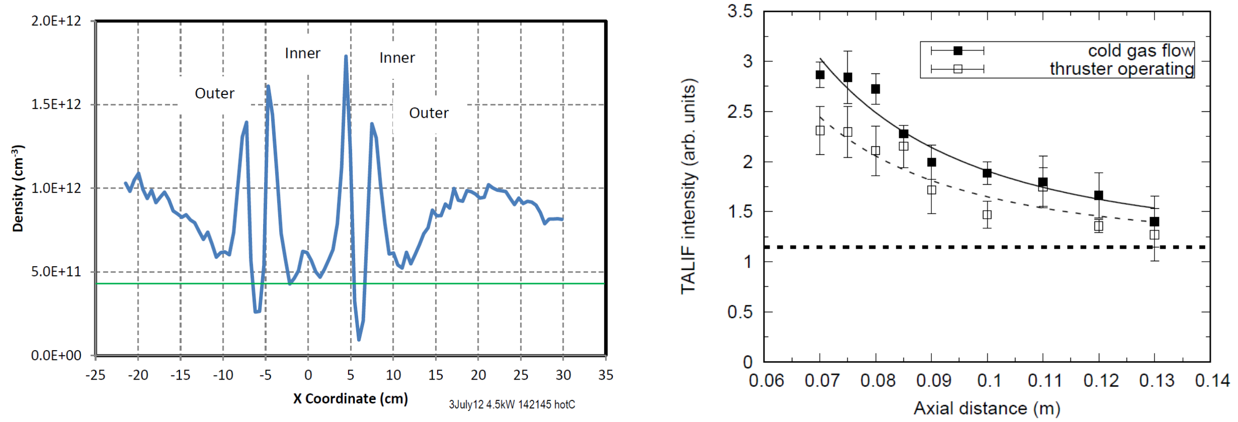

Figure 17: Left: Calibrated density profile of neutral xenon measured across the face of a SPT-140 thruster (inner and outer refer to discharge channel edges) during thruster operation [124]. Right: Relative neutral density measurements of krypton along the central thruster axis in the plume of a RIT-10 [130].

Another approach towards absolute signal calibration is to measure the TALIF signal from a reference cell filled with a known density of the target species of interest (e.g., Kr) [125]. The most straightforward method is to use the same laser beam focusing, fluorescence collection optics, and measurement position as the actual experiment, i.e., the reference cell is positioned at the measurement location of the actual experiment. In this way, the TALIF signal of the reference cell should have the same proportionality between signal to species density as in the actual experiment, since factors such as collection solid angle remain and beam intensity remain unchanged, allowing a simple-ratio method for absolute calibration. For good accuracy and precision, the reference cell should be filled with the target species at a relatively similar density to that of the actual experiments (typically $\sim 10^{11} - 10^{13}\,\mathrm{cm}^{-3}$). During the manufacturing process, a cell is typically filled using a partial pressure approach to reduce uncertainty in the absolute density of the target species, because the required absolute densities are quite low. A common method is to mix the target species with an inert buffer, for example using a fill-gas composition of 1 part Kr and 1000 parts of Ar, such that the total cell pressure with the gas mixture is about 1000 times higher than the partial pressure of the species of interest

Two examples for absolute neutral density measurement in a HET and relative neutral density measurement in a RIT device are presented in Fig. 17.

10 Recommended Practices for TALIF Measurements

In the following, we summarize some recommended practices for the application of TALIF as an EP diagnostic. TALIF is a very powerful, and, at the same time, sensitive plasma diagnostic technique. A principal challenge for the user is to obtain good signal-to-noise ratio, adapting the experimental set-up to large-scale vacuum facilities as they are required for EP testing (as well as for many other aerospace applications). Therefore, the issue of optimizing signal intensity, while ensuring quantitative measurement conditions, is an area of focus.

- Use a narrow bandwidth laser source if possible. If the laser linewidth is too broad ($\geq$ 50 GHz) the signal amplitude will be substantially reduced and limit sensitivity of the measurement. In intermediate regimes ($\sim$ 2-50 GHz) the linewidth will likely still preclude precise analyses of Doppler shifts (particle velocity) or lineshape broadening (plasma temperature). The use of yet narrower linewidths, for example for injection seeded systems also represents a promising future direction for more detailed spectral measurements. An etalon can potentially be used to reduce laser linewidth but generally at the cost of lower pulse energy (signal level) and some inconvenience.

- Capture the fluorescence with a high f-number optic to maximize signal level. Locate collection optics inside the vacuum chamber to enable higher solid angle for the detection.

- Use narrow band ($\sim$0.1-1 nm), specialized optical filters or ideally incorporate a high resolution monochromator. This will improve the signal-to-noise ratio, block the detection of extraneous emission lines, and minimize the effect of line blending, which may lead to non-single component fluorescence decay curves. The transmission of an optical filter should peak at the desired fluorescence wavelength.

- Choose a transition with high two-photon absorption cross section, in a convenient spectral region for generating energetic laser pulses. A convenient spectral region may, for example, depend on the efficiency of the laser dyes employed, and/or frequency conversion mechanisms (second or third harmonic generation, frequency mixing, etc.)

- Choose a fluorescence transition to monitor that has high oscillator strength and high branching ratio. The detector parameters (such as quantum efficiency of the PMT, efficiency of the linewidth filtering) should also be considered. Selecting a transition with weak optical emission intensity during thruster operation may also improve the signal-to-noise ratio.

- If an optical fiber, slit or aperture is employed, ensure that dimensions are suitable to obtain good signal to noise, appropriate spatial resolution and so on.

- Measure the laser energy per pulse and plot signal vs pulse energy. This will identify pulse energy regimes in which the $S \propto E^2$ relation does not hold. Normalize the signal to the pulse energy as appropriate.

- Focus the laser beam into the interaction region with focal length and beam waist suitable for high signal to noise ratio and good spatial resolution, given the available pulse energy.

- If it is difficult to measure the $S(E)$ relation, use a fixed (average) laser pulse energy for the experiment (and calibration). Check the $S \propto n_0$ proportionality, in particular if the occurrence of ASE cannot be excluded.

- Subtract plasma emission background from detector signal.

- Check for all kind of drifts (laser wavelength, -energy, box car offset, plasma self-emission, etc.), especially if absorption profiles are not fully scanned.

- Verify that the absorption profile does not depend on location of the probe region. If it does vary substantially, scan over the profile and integrate at each location to obtain relative density.

With respect to the calibration of the TALIF signal to absolute density, the user is encouraged to choose an approach described in paragraph E of section 9, which is best suited under the conditions of the respective TALIF.

11 Recent Developments and Related Techniques

In this section, we briefly discuss some recent and emerging developments of TALIF diagnostics relevant to electric propulsion. Specific areas covered include temporally-resolved TALIF, flow-tagging, and TALIF of molecular species. Additional new directions may emerge due to novel equipment capabilities such as pulse-burst lasers, providing much higher repetition rates relative to what are currently used, along with emerging possibilities due to picosecond and femtosecond lasers [162] where the high pulse intensities impact the competition of absorption and emission with quenching, photoionization and other excitation/loss channels.

11.1 Temporally Resolved TALIF Studies

Recent work has shown the possibility of temporally-resolved TALIF to show the dynamic variation of neutral population during breathing mode oscillations of a HET operating on Kr [125]. The optical setup was similar to Figure 13 with the key differences being in the signal processing methodology. The experiments employed a 212.6 nm excitation scheme with detection at 760 nm. The beam, from a nanosecond Nd:YAG pumped dye laser, was coupled into the vacuum chamber and brought to a weak focus by a plano-convex lens. The TALIF signal was collected with a lens at an angle perpendicular to the probe beam and passed with an optical fiber to a photomultiplier tube equipped with a bandpass filter. The Hall Effect thruster used in this work is a 1.5 kW SPT-like thruster with a center mounted 25 A class Ba-O based hollow cathode. A phase-binning approach was developed to measure TALIF signal oscillations synchronous to thruster breathing mode oscillations. The laser system was operated at its regular 10 Hz pulse repetition rate (using its internal clock) and the thruster was also operated in regular manner with no external voltage modulation. The current fluctuations of the specific thruster under study were rather strong, on the order of 500% in terms of the ratio of peak (∼25 A) to mean (5 A), and quite periodic, which facilitated the approach. Each individual TALIF signal (due to a single pulse from the dye laser) was binned into $N = 20$ equally sized phase-bins based on the timing of the TALIF laser relative to the phase of the breathing mode, where phase of zero and 2p were defined to coincide with maxima (peaks) of the discharge current fluctuation, as shown in the left of Figure 18. Within each phase bin, the data associated with individual laser shots are arbitrarily sub-divided into groups of $n = 100$ individual shots. The right of Figure 18 shows the resulting time-resolved TALIF signals, representing (relative) Kr density as a function of phase (or equivalently time given the measured period of 55.1 ms), across the breathing mode. Ongoing and future research will extend to absolute density measurements (e.g., with reference cell), compare data with models of the breathing mode, and seek to expand the technique to higher frequency and/or weaker and/or less periodic oscillations.

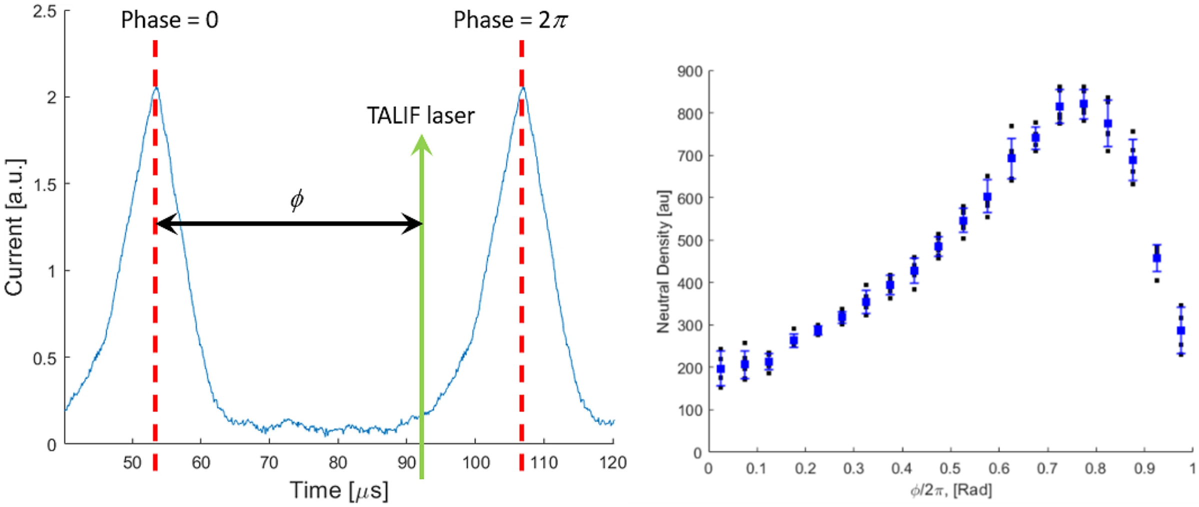

Figure 18: Left: Method for determining the phase of an individual TALIF measurement relative to the breathing mode oscillation. Right: TALIF signal versus phase angle over one oscillation period (20 phase bins) [125].

11.2 Flow-Tagging Velocimetry

Recent work has shown the possibility of using TALIF in a flow-tagging ("read-write") configuration to directly tag and track the motion (velocity) of ground state Kr atoms at EP relevant conditions [163]. While TALIF is generally used for density measurements, the motivation here is to additionally capture velocity using a 2-step TALIF/LIF approach, also referred to as Read-Write where, in short, a first TALIF step excites ground state Kr neutrals to a long-lived metastable energy level which can in turn be re-excited, and detected, by a second LIF scheme. By measuring the tagged species at later times and at known displacements relative to their creation point, velocity distributions and temperatures can be inferred. Development of the technique for EP application has followed a recent literature on Krypton Tagging Velocimetry (KVD) which has sought to develop the technique for velocity measurements in challenging fluid mechanical environments such as in hypersonic tunnels [153, 164–166]. The recent EP demonstration utilized a TALIF excitation (Write) at 214.7 nm from a pulsed dye laser, followed by a LIF re-excitation (Read) of the ensuing metastable at 769.5 nm with a second beam. Studies were performed for both cold krypton gas expanding from a hollow cathode into vacuum, yielding bulk velocity of ∼ 450 m/s, as well as in the plume with of the hollow cathode plasma yielding bulk velocity of 1200 m/s. In contrast to the KDV hypersonics work, the EP demonstration was a background pressure of $\sim 10^{-5}$ Torr. In the future, it may be possible to use such combined TALIF/LIF approaches to directly measure both the density and velocity of ground state propellant atoms.

11.3 TALIF of Atoms due to Molecular Feedstocks

Nearly all TALIF work conducted to date in support of EP applications has been directly at noble gases, primarily xenon and krypton (argon also possible), owing to their prominent usage as EP propellants. However, there is growing interest in other propellant species, particularly molecular propellants (i.e., propellants with molecular gases as the feedstock to the thruster) owing to emerging applications including air breathing propulsion for Very Low Earth Orbit (VLEO), dual-mode propulsion (i.e., use of a common fuel, potentially liquid or gas, for both chemical propulsion and electric propulsion, possibly after initial decomposition steps), and future schemes based on in situ resource utilization (ISRU). As diagnostic interest for these applications grow, it is likely that the TALIF diagnostic will expand accordingly to allow probing of species relevant to these systems. Plasma kinetics of molecular feedstocks tend to be more complex since processes including dissociation and vibrational excitation now also compete with ionization and electronic excitation. Depending on conditions, atomic species, such as H, O and N can form from starting diatomic (or larger molecules) feedstocks. The energy levels for these species also preclude direct single-photon probing of the group state but TALIF schemes for H, O and N are available from past EP work and fields such as plasma assisted combustion [167–170], with the TALIF generally in the $\sim 200-225$ nm range. There have also been limited reports of TALIF to directly probe ground states of molecular species themselves, notably for CO [171], which may be of interest for EP molecular feedstocks.

Acknowledgments

This research was carried out at the Jet Propulsion Laboratory (JPL), California Institute of Technology,under a contract with the National Aeronautics and Space Administration (80NM0018D0004). The contribution of Christoph Eichhorn was financially supported by the Deutsches Zentrum für Luft- und Raumfahrt (DLR) and the Bundesministerium für Wirtschaft und Klimaschutz (BMWi) through project grant BMWi 50RS2102, which is gratefully acknowledged. The contribution of Azer Yalin was financially supported by NASA through the Joint Advanced Propulsion Institute, a NASA Space Technology Research Institute, grant number 80NSSC21K1118.

References

[1] Stern, R. A., and Johnson, III, J. A., "Plasma Ion Diagnostics Using Resonant Fluorescence," *Phys. Rev. Lett.*, Vol. 34, No. 25, 1975, pp. 1548–1551.

[2] Manzella, D. H., "Stationary Plasma Thruster Ion Velocity Distribution," *30th AIAA/ASME/SAE/ASEE Joint Propulsion Conference*, Indianapolis, IN, 1994. AIAA-94-3141.

[3] Cedolin, R. J., W. A. Hargus, J., Storm, P. V., Hanson, R. K., and Cappelli, M. A., "Laser-Induced Fluorescence Study of a Xenon Hall Thruster," *Appl. Phys. B*, Vol. 65, 1997, pp. 459–469.

[4] Shine, B., and Day, T., "Tunable Diode Lasers," *Lasers and Optronics*, 1998, pp. 13–14. URL `https://www.newport.com/medias/sys_master/images/images/h00/h0b/8797292822558/Tunable-Diode-Lasers.pdf`.

[5] Hargus, W. A., "Investigation of the Plasma Acceleration Mechanism within a Coaxial Hall Thruster," Ph.D. thesis, Stanford University, 2001.

[6] Crofton, M. W., "Measurement of Barium Production in a Hollow Cathode," *43rd AIAA Aerospace Sciences Meeting and Exhibit*, Reno, NV, 2005. AIAA-2005-368.

[7] Huang, W., Gallimore, A. D., and Hofer, R. R., "Neutral Flow Evolution in a Six-Kilowatt Hall Thruster," *J. Prop. Power*, Vol. 27, No. 3, 2011. https://doi.org/10.2514/1.B34048.

[8] Mazouffre, S., "Laser-Induced Fluorescence Diagnostics of the Cross-Field Discharge of Hall Thrusters," *Plasma Sources Sci. Technol.*, Vol. 22, 2013, p. 013001.

[9] Vaudolon, J., and Mazouffre, S., "Indirect Determination of the Electric Field in Plasma Discharges Using Laser-Induced Fluorescence Spectroscopy," *Phys. Plasmas*, Vol. 21, 2014, p. 093505.

[10] Jorns, B. A., Dodson, C., Anderson, J., Goebel, D. M., Hofer, R. R., Sekerak, M., Lopez Ortega, A., and Mikellides, I. G., "Mechanisms for Pole Piece Erosion in a 6-kW Magnetically Shielded Hall Thruster," *52nd AIAA/SAE/ASEE Joint Propulsion Conference*, Salt Lake City, UT, 2016. https://doi.org/10.2514/6.2016-4839, AIAA-2016-4839.

[11] Grimaud, L., and Mazouffre, S., "Ion Behavior in Low-Power Magnetically Shielded and Unshielded Hall Thrusters," *Plasma Sources Sci. Technol.*, Vol. 26, 2017, p. 055020.

[12] Young, C. V., Lucca Fabris, A., MacDonald-Tenenbaum, N. A., Hargus, W. A., and Cappelli, M. A., "Time-Resolved Laser-Induced Fluorescence Diagnostics for Electric Propulsion and Their Application to Breathing Mode Dynamics," *Plasma Sources Sci. Technol.*, Vol. 27, 2018, p. 094004. https://doi.org/10.1088/1361-6595/aade42.

[13] Eichhorn, C., Scholze, F., Bundesmann, C., Spemann, D., Neumann, H., and Leiter, H., "Two-Photon Laser-Induced Fluorescence Diagnostics of a Radiofrequency Ion Thruster: Measurements in Xenon and Krypton," *36th International Electric Propulsion Conference*, Vienna, Austria, 2019. IEPC-2019-503.

[14] Dale, E. T., and Jorns, B. A., "Non-Invasive Time-Resolved Measurements of Anomalous Collision Frequency in a Hall Thruster," *Phys. Plasmas*, Vol. 26, 2019, p. 013516. https://doi.org/10.1063/1.5077008.

[15] Chaplin, V. H., Lobbia, R. B., Lopez Ortega, A., Mikellides, I. G., Hofer, R. R., Polk, J. E., and Friss, A. J., "Time-Resolved Ion Velocity Measurements in a High-Power Hall Thruster Using Laser-Induced Fluorescence with Transfer Function Averaging," *Appl. Phys. Lett.*, Vol. 116, 2020, p. 234107. https://doi.org/10.1063/5.0007161.

[16] Wegner, T., Dumitrache, C., and Yalin, A. P., "Rate-Equation Modeling of Xe and Kr TALIF for Electric Propulsion Applications," *37th International Electric Propulsion Conference*, Cambridge, MA, USA, 2022.

[17] Gottfried, J., Antozzi, S., Stienike, J., Thompson, S., Williams, J., and Yalin, A., "Temporally Resolved Neutral Density Measurements of Hall Effect Thruster Breathing Mode by Two-Photon Absorption Laser Induced Fluorescence (TALIF)," *AIAA SciTech Forum*, Orlando, FL, 2024.

[18] Jorns, B. A., Goebel, D. M., and Hofer, R. R., "Plasma Perturbations in High-Speed Probing of Hall Thruster Discharge Chambers: Quantification and Mitigation," *51st AIAA/SAE/ASEE Joint Propulsion Conference*, Orlando, FL, 2015. https://doi.org/10.2514/6.2015-4006, AIAA-2015-4006.

[19] Grimaud, L., Pétin, A., Vaudolon, J., and Mazouffre, S., "Perturbations Induced by Electrostatic Probe in the Discharge of Hall Thrusters," *Rev. Sci. Instrum.*, Vol. 87, 2016, p. 043506. https://doi.org/10.1063/1.4945563.

[20] Huang, W., and Kamhawi, H., "Counterstreaming Ions at the Inner Pole of a Magnetically Shielded Hall Thruster," *J. Appl. Phys.*, Vol. 129, 2021, p. 043305. https://doi.org/10.1063/5.0029428.

[21] Roberts, P. J., Chaplin, V. H., and Jorns, B. A., "Azimuthal Ion Dynamics at the Inner Pole of an Axisymmetric Hall Thruster," *Phys. Plasmas*, Vol. 31, 2024, p. 083513.

[22] Lopez Ortega, A., Mikellides, I. G., Chaplin, V. H., Huang, W., and Frieman, J. D., "Anomalous Ion Heating and Pole Erosion in the 12.5 kW Hall Effect Rocket with Magnetic Shielding (HERMeS)," *AIAA Propulsion and Energy 2020 Forum*, Virtual Event, 2020. https://doi.org/10.2514/6.2020-3620, AIAA-2020-3620.

[23] Mikellides, I. G., Lopez Ortega, A., and Chaplin, V. H., "Theory of the Anomalous Momentum Exchange from Wave-Particle Interactions in Hall-Effect Ion Accelerators and Comparisons with Measurements," *Phys. Fluids*, Vol. 36, 2024, p. 074121.

[24] Crofton, M. W., Schoeffler, D. T., Young, J. A., and Patterson, M. J., "Erosion Rate Measurements for DART Spacecraft Ion Propulsion System," *Applied Sciences*, Vol. 12, 2022, p. 7831. https://doi.org/10.3390/app12157831.

[25] Storm, P. V., and Cappelli, M. A., "Arcjet Nozzle Flow-Field Characterization by Laser-Induced Fluorescence," *Applied Optics*, Vol. 37, No. 3, 1998, pp. 486–495. https://doi.org/10.1364/AO.37.000486.

[26] Williams, Jr., G. J., Smith, T. B., Domonkos, M. T., Gallimore, A. D., and Drake, R. P., "Laser-Induced Fluorescence Characterization of Ions Emitted from Hollow Cathodes," *IEEE Trans. Plasma. Sci*, Vol. 28, No. 5, 2000, pp. 1664–1675.

[27] Roberts, P. J., Jorns, B. A., and Chaplin, V. H., "Experimental Characterization of Wave-Induced Azimuthal Ion Velocities in a Hollow Cathode Plume," *AIAA SciTech 2022 Forum*, San Diego, CA and Virtual, 2022. AIAA-2022-1561.

[28] Vinci, A. E., Mazouffre, S., Gómez, V., Fajardo, P., and Navarro-Cavallé, J., "Laser-Induced Fluorescence Spectroscopy on Xenon Atoms and Ions in the Magnetic Nozzle of a Helicon Plasma Thruster," *Plasma Sources Science and Technology*, Vol. 31, 2022, p. 095007. https://doi.org/10.1088/1361-6595/ac8db8.

[29] Elias, P.-Q., Packan, D., Bonnet, J., Ceccanti, F., Cesari, U., De Tata, M., Nicolini, D., and Gengembre, E., "Optical Measurements of Neutral Cesium Mass Flow Rate in Field Emission Thrusters," *Journal of Propulsion and Power*, Vol. 27, No. 2, 2011, pp. 448–460. https://doi.org/10.2514/1.47830.

[30] Chaplin, V. H., Johnson, L. K., Lobbia, R. B., Konopliv, M. F., Simka, T., and Wirz, R. E., "Insights from Collisional-Radiative Models of Neutral and Singly Ionized Xenon in Hall Thrusters," *Journal of Propulsion and Power*, Vol. 38, No. 5, 2022, pp. 866–879. https://doi.org/10.2514/1.B38676.

[31] Eichhorn, C., Pietzonka, L., Scholze, F., Bundesmann, C., Spemann, D., Neumann, H., and Leiter, H. J., "Single- and Two-Photon Absorption Laser-Induced Fluorescence Spectroscopy in Rare Gases for Gridded Ion Thruster Diagnostics," *EPJ Techniques and Instrumentation*, Vol. 9, No. 2, 2022. https://doi.org/10.1140/epjti/s40485-022-00077-y.

[32] Cedolin, R. J., W. A. Hargus, J., Storm, P. V., Hanson, R. K., and Cappelli, M. A., "Laser-Induced Fluorescence Study of a Xenon Hall Thruster," *Applied Physics B*, Vol. 65, 1997, pp. 459–469. https://doi.org/10.1007/s003400050297.

[33] Hargus, W. A., "Laser-Induced Fluorescence of Neutral Xenon in the Near Field of a 200 W Hall Thruster," *41st AIAA/ASME/SAE/ASEE Joint Propulsion Conference & Exhibit*, Tucson, AZ, 2005. AIAA-2005-4400.

[34] Hargus Jr., W. A., "A Preliminary Study of Krypton Laser-Induced Fluorescence," *46th AIAA/ASME/SAE/ASEE Joint Propulsion Conference & Exhibit*, 2010. AIAA-2010-6524.

[35] Hargus, Jr., W. A., Lubkeman, J. S., Remy, K. E., and Gonzales, A. E., "Investigation of Singly Ionized Iodine Spectroscopy in Support of Electrostatic Propulsion Diagnostics Development," *48th AIAA/ASME/SAE/ASEE Joint Propulsion Conference and Exhibit*, Atlanta, GA, 2012. AIAA-2012-4316.

[36] Esteves, B., "Investigation of Iodine Plasmas for Space Propulsion Applications," Ph.D. thesis, Ecole Polytechnique, Laboratoire de Physique des Plasmas, 2022.

[37] Kramida, A., Y. Ralchenko, Reader, J., and NIST ASD Team, NIST Atomic Spectra Database (ver. 5.12), [Online]. Available: `http://physics.nist.gov/asd` [Thu Mar 13 2025]. National Institute of Standards and Technology, Gaithersburg, MD., 2024. https://doi.org/10.18434/T4W30F.

[38] Peck, E. R., and Reeder, K., "Dispersion of Air," *Journal of the Optical Society of America*, Vol. 62, No. 8, 1972, pp. 958–962. https://doi.org/10.1364/JOSA.62.000958.

[39] Young, L., Yang, D., and Dunford, R. W., "Optical Production of Metastable Krypton," *Journal of Physics B: Atomic, Molecular and Optical Physics*, Vol. 35, No. 13, 2002, pp. 2985–2992. https://doi.org/10.1088/0953-4075/35/13/311.

[40] Cannon, B. D., and Janik, G. R., "Hyperfine Splittings and Isotope Shifts in Eight Transitions from the Metastable $4p^5 5s$ J = 2 and J = 0 states of Kr I," *Physical Review A*, Vol. 42, No. 1, 1990, p. 397. https://doi.org/10.1103/PhysRevA.42.397.

[41] Scharfe, D. B., "Alternative Hall Thruster Propellants Krypton and Bismuth: Simulated Performance and Characterization," Ph.D. thesis, Stanford University, 2009.

[42] Hargus Jr., W. A., Azarnia, G. M., and Nakles, M., "Kr II Laser-Induced Fluorescence for Measuring Plasma Acceleration," *Review of Scientific Instruments*, Vol. 83, No. 10, 2012. https://doi.org/10.1063/1.4754889.

[43] Su, L. L., Marks, T. A., and Jorns, B. A., "Trends in Mass Utilization of a Magnetically Shielded Hall Thruster Operating on Xenon and Krypton," *Plasma Sources Science and Technology*, Vol. 33, No. 6, 2024, p. 065008. https://doi.org/10.1088/1361-6595/ad52be.

[44] Lejeune, A., Bourgeois, G., and Mazouffre, S., "Kr II and Xe II Axial Velocity Distribution Functions in a Cross-Field Ion Source," *Physics of Plasmas*, Vol. 19, No. 7, 2012. https://doi.org/10.1063/1.4731688.

[45] Zhang, F., Komurasaki, K., Iida, T., and Fujiwara, T., "Diagnostics of an Argon Arcjet Plume with a Diode Laser," *Applied Optics*, Vol. 38, No. 9, 1999, pp. 1814–1822. https://doi.org/10.1364/AO.38.001814.

[46] Ruyten, W. M., and Keefer, D., "Laser Fluorescence Velocimetry of an Arcjet Exhaust Plume," *22th International Electric Propulsion Conference*, Viareggio, Italy, 1991. IEPC-91-093.

[47] Severn, G. D., Edrich, D. A., and McWilliams, R., "Argon Ion Laser-Induced Fluorescence with Diode Lasers," *Rev. Sci. Instrum.*, Vol. 69, No. 1, 1998, pp. 10–15.

[48] Kang, I. J., Yang, J. K., Park, I. S., Choi, Y., and Chung, K., "Measurement of Laser Induced Fluorescence for Argon Plasma Flow with Oxygen Injection," *AIP Advances*, Vol. 13, 2023, p. 075227.

[49] Steinberger, T. E., and Scime, E. E., "Laser-Induced Fluorescence of Singly Ionized Iodine," *Journal of Propulsion and Power*, Vol. 34, No. 5, 2018, pp. 1235–1239. https://doi.org/10.2514/1.B37107.

[50] Lazo, M. J., Steinberger, T. E., Good, T. N., and Scime, E. E., "Measurements of the $^5D^o_4$ – $^5P_3$ transition of singly ionized atomic iodine using intermodulated laser induced fluorescence," *Journal of Quantitative Spectroscopy and Radiative Transfer*, Vol. 277, 2022, p. 107960. https://doi.org/10.1016/j.jqsrt.2021.107960.

[51] Gaeta, C. J., Matossian, J. N., Turley, R. S., Beattie, J. R., Williams, J. D., and Williamson, W. S., "Erosion Rate Diagnostics in Ion Thrusters Using Laser-Induced Fluorescence," *J. Prop. Power*, Vol. 9, 1993, p. 369. https://doi.org/10.2514/3.23631.

[52] Crofton, M. W., "Laser Spectroscopic Study of the T5 Ion Thruster," *31st Joint Propulsion Conference*, San Diego, CA, 1995. AIAA-95-2921.

[53] Quinet, P., Vinogradoff, V., Palmeri, P., and Biemont, E., "Radiative Decay Rates for W I, W II and W III Allowed and Forbidden Transitions of Interest for Spectroscopic Diagnostics in Fusion Plasmas," *J. Phys. B: At. Mol. Opt. Phys.*, Vol. 43, 2010, p. 144003. https://doi.org/10.1088/0953-4075/43/14/144003.

[54] Den Hartog, E. A., Duquette, D. W., and Lawler, J. E., "Absolute transition probabilities in Ta I and W I," *J. Opt. Soc. Am. B*, Vol. 4, 1987, pp. 48–63. https://doi.org/10.1364/JOSAB.4.000048.

[55] Simmonds, J. B., Byrne, M. P., and Chaplin, V. H., "Xenon Tracers for Cost Effective Laser Induced Fluorescence of Alternative Propellant Hall Thrusters," *Review of Scientific Instruments*, Vol. 95, 2024, p. 023502. https://doi.org/10.1063/5.0179938.

[56] Vaudolon, J., and Mazouffre, S., "Indirect Determination of the Electric Field in Plasma Discharges Using Laser-Induced Fluorescence Spectroscopy," *Physics of Plasmas*, Vol. 21, 2014, p. 093505. https://doi.org/10.1063/1.4895532.

[57] Cedolin, R. J., "Laser-Induced Fluorescence Diagnostics of Xenon Plasmas," Ph.D. thesis, Stanford University, 1997.

[58] Su, L., "Performance of a Magnetically Shielded Hall Thruster Operating on Krypton at High Powers," Ph.D. thesis, 2023.

[59] ANSI Z136.1-2022, *American National Standard for Safe Use of Lasers*, Washington, D.C., 2022.

[60] Smith, T. B., "Deconvolution of Ion Velocity Distributions from Laser-Induced Fluorescence Spectra of Xenon Electrostatic Thruster Plumes," Ph.D. thesis, University of Michigan, 2003.

[61] Roberts, P. J., "Characterization of Momentum and Heat Flow in Hall Thrusters with Laser Scattering," Ph.D. thesis, University of Michigan, 2025.

[62] Elias, P. Q., Jarrige, J., Cucchetti, E., Cannat, F., and Packan, D., "3D Ion Velocity Distribution Function Measurement in an Electric Thruster Using Laser Induced Fluorescence Tomography," *Rev. Sci. Instrum.*, Vol. 88, 2017, p. 093511.

[63] Chaplin, V. H., Jorns, B. A., Conversano, R. W., Lobbia, R. B., Lopez Ortega, A., Mikellides, I. G., and Hofer, R. R., "Laser-Induced Fluorescence Measurements of the Acceleration Zone in the 12.5 kW HERMeS Hall Thruster," *35th International Electric Propulsion Conference*, Atlanta, GA, 2017. IEPC-2017-229.

[64] "About Lock-In Amplifiers," Tech. Rep. Application Note #3, Stanford Research Systems, ???? https://www.thinksrs.com/downloads/pdfs/applicationnotes/AboutLIAs.pdf, Accessed: July 8, 2025.

[65] Beiting, E. J., Spektor, R., Diamant, K. D., Corey, R., and Delgado, J., "Near Field Maps of Xenon Ion Velocity of the SPT-140 Hall Thruster by Laser Induced Fluorescence," *33rd International Electric Propulsion Conference*, Washington D. C., USA, 2013. IEPC-2013-053.

[66] Durot, C. J., Gallimore, A. D., and Smith, T. B., "Validation and Evaluation of a Novel Time-Resolved Laser-Induced Fluorescence Technique," *Rev. Sci. Instrum.*, Vol. 85, 2014, p. 013508.

[67] Chaplin, V. H., Byrne, M. P., Lobbia, R. B., Polk, J. E., Lopez Ortega, A., and Mikellides, I. G., "Azimuthal Ion Velocity Measurements in the 12 kW HERMeS Hall Thruster," *38th International Electric Propulsion Conference*, Toulouse, France, 2024. IEPC-2024-207.

[68] Paschotta, R., "Acousto-optic Modulators," RP Photonics Encyclopedia, 2008. Available online at https://www.rp-photonics.com/acousto_optic_modulators.html.

[69] Chaplin, V. H., Jorns, B. A., Lopez Ortega, A., Mikellides, I. G., Conversano, R. W., Lobbia, R. B., and Hofer, R. R., "Laser-Induced Fluorescence Measurements of Acceleration Zone Scaling in the 12.5 kW HERMeS Hall Thruster," *J. Appl. Phys.*, Vol. 124, 2018, p. 183302.

[70] Cusson, S. E., Dale, E. T., Jorns, B. A., and Gallimore, A. D., "Acceleration Region Dynamics in a Magnetically Shielded Hall Thruster," *Phys. Plasmas*, Vol. 26, 2019, p. 023506.

[71] Hargus, W. A., and Cappelli, M. A., "Laser-Induced Fluorescence Measurements of Velocity with a Hall Discharge," *Appl. Phys. B*, Vol. 72, 2001, pp. 961–969.

[72] Spektor, R., "Computation of Two-Dimensional Electric Field from the Ion Laser Induced Fluorescence Measurements," *Phys. Plasmas*, Vol. 17, 2010, p. 093503.

[73] Chaplin, V. H., Lopez Ortega, A., Byrne, M. P., and Mikellides, I. G., "Swirl Torque Projections for the 12 kW Advanced Electric Propulsion System (AEPS) Hall Thruster," *AIAA SciTech 2025 Forum*, Orlando, FL, 2025.

[74] Williams, Jr., G. J., Smith, T. B., Gulczinski, F. S., Beal, B. E., Gallimore, A. D., and Drake, R. P., "Laser Induced Fluorescence Measurement of Ion Velocities in the Plume of a Hall Effect Thruster," *35th AIAA/ASME/SAE/ASEE Joint Propulsion Conference & Exhibit*, Los Angeles, CA, 1999. https://doi.org/10.2514/6.1999-2424, aIAA-1999-2424.

[75] Sadeghi, N., Dorval, N., Bonnet, J., Pigache, D., Kadlec-Phiippe, C., and Bouchoule, A., "Velocity Measurements of Xe+ in Stationary Plasma Thruster Using LIF," *35th AIAA/ASME/SAE/ASEE Joint Propulsion Conference & Exhibit*, Los Angeles, CA, 1999. https://doi.org/10.2514/6.1999-2429, aIAA-1999-2429.

[76] Duan, X., Cheng, M., Yang, X., Guo, N., Li, X., Wang, M., and Guo, D., "Investigation on Ion Behavior in Magnetically Shielded and Unshielded Hall Thrusters by Laser-Induced Fluorescence," *J. Appl. Phys.*, Vol. 127, 2020, p. 093301. https://doi.org/10.1063/1.5140514.

[77] Roberts, P. J., Chaplin, V. H., Lopez Ortega, A., and Mikellides, I. G., "Impact of Low-Frequency Oscillations on Ion Energy in a High-Power Magnetically Shielded Hall Thruster," *J. Appl. Phys.*, Vol. 131, No. 3, 2023, p. 033301. https://doi.org/10.1063/5.0067325.

[78] Huang, W., "Study of Hall Thruster Discharge Channel Wall Erosion via Optical Diagnostics," Ph.D. thesis, University of Michigan, 2011.

[79] Nussbaumer, H. J., *Fast Fourier Transform and Convolution Algorithms*, Springer Series in Information Sciences, Springer, Berlin, Germany, 1982.

[80] Petrov, G. M., "A Simple Algorithm for Spectral Line Deconvolution," *J. Quant. Spectrosc. Radiat. Transfer*, Vol. 72, No. 3, 2002, pp. 281–287.

[81] Hansen, P. C., and O'Leary, D. P., "The Use of the L-Curve in the Regularization of Discrete Ill-Posed Problems," *SIAM Journal on Scientific Computing*, Vol. 14, No. 6, 1993, pp. 1487–1503. https://doi.org/10.1137/0914086.

[82] Rybicki, G. B., and Lightman, A. P., *Radiative Processes in Astrophysics*, 2^{nd} ed., Wiley-VCH, Germany, 2004.

[83] Woodgate, G. K., *Elementary Atomic Structure*, Clarendon, Oxford, UK, 1980.

[84] Schuessler, H. A., Alousi, A., Idrees, M., Li, Y. F., Buchinger, F., Evans, R. M., and Fischer, C. F., "Isotope Shifts and Hyperfine-Structure-Splitting Constants of the $4d$-$5p$ Transition of Kr II at $\lambda = 729$ nm," *Phys. Rev. A*, Vol. 45, 1992, p. 6459.

[85] Pawelec, E., Mazouffre, S., and Sadeghi, N., "Hyperfine Structure of some Near-Infrared Xe I and Xe II Lines," *Spectrochimica Acta Part B*, Vol. 66, 2011, pp. 470–475.

[86] Sargsyan, A., Tonoyan, A., Hakhumyan, G., Leroy, C., Pashayan-Leroy, Y., and D.Sarkisyan, "Atomic Transitions of Rb, D2 Line in Strong Magnetic Fields: Hyperfine Paschen–Back Regime," *Opt. Commun.*, Vol. 334, 2015, pp. 208–213.

[87] Condon, E. U., and Shortley, G. H., *The Theory of Atomic Spectra*, Cambridge University Press, Cambridge, UK, 1935.

[88] Demtröder, W., *Laser Spectroscopy*, Springer-Verlag, Berlin Heidelberg, 2003.

[89] Mazouffre, S., Bourgeois, G., Garrigues, L., and Pawelec, E., "A Comprehensive Study on the Atom Flow in the Cross-Field Discharge of a Hall Thruster," *J. Phys. D: Appl. Phys.*, Vol. 44, 2011, p. 105203.

[90] Saloman, E. B., "Energy Levels and Observed Spectral Lines of Xenon, Xe I Through Xe LIV," *J. Phys. Chem. Ref. Data*, Vol. 33, 2004, pp. 765–921.

[91] Suzuki, M., Katoh, K., and Nishimiya, N., "Saturated Absorption Spectroscopy of Xe Using a GaAs Semiconductor Laser," *Spectrochim Acta A Mol. Biomol. Spectrosc.*, Vol. 58, 2002, pp. 2519–2531.

[92] Smith, T. B., Ngom, B. B., Linnell, J. A., and Gallimore, A. D., "Diode Laser-Induced Fluorescence of Xenon Ion Velocity Distributions," *41st AIAA/ASME/SAE/ASEE Joint Propulsion Conference*, Tuscon, AZ, 2005. AIAA-2005-4406.

[93] Broström, L., Kastberg, A., Lidberg, J., and Mannervik, S., "Hyperfine-Structure Measurements in Xe II," *Phys. Rev. A*, Vol. 53, 1996, pp. 109–112.

[94] Fuller, G. H., "Nuclear Spins and Moments," *J. Phys. Chem. Ref. Data*, Vol. 5, 1976, pp. 835–1092.

[95] Sansonetti, J. E., and Martin, W. C., "Handbook of Basic Atomic Spectroscopic Data," *J. Phys. Chem. Ref. Data*, Vol. 34, 2005, pp. 1559–2259.

[96] Kopfermann, H., *Nuclear Moments (Pure and Applied Physics)*, Vol. 2, Elsevier, Amsterdam, Holland, 1958.

[97] Vinci, A. E., Inchingolo, M. R., Mazouffre, S., and Navarro-Cavallé, J., "Ion Dynamics in the Magnetic Nozzle of a Waveguide ECR Thruster Via Laser-Induced Fluorescence Spectroscopy," *J. Phys. D: Appl. Phys.*, Vol. 56, 2023, p. 025204.

[98] Ngom, B. B., "Magnetic Field Simulation and Mapping Based on Zeeman-Split Laser-Induced Fluorescence Spectra of Xenon in the Discharge Channel of 5–6 kW Coaxial Stationary-Plasma Hall Thrusters," Ph.D. thesis, University of Michigan, 2009.

[99] Huang, W., Ngom, B. B., and Gallimore, A. D., "Using Nonlinear Zeeman Spectroscopy to Obtain In-Situ Magnetic Field Measurements in a Hall Thruster," *31st International Electric Propulsion Conference*, Ann Arbor, MI, USA, 2009. IEPC-2009-088.

[100] Da Valle, M., Dancheva, Y., Khanbekyan, A., Mariotti, E., and Scortecci, F., "Laser-Induced Fluorescence Spectroscopy on Neutrals for Plasma Studies in Hall Thrusters," *J. Electric Propulsion*, Vol. 4, 2025, p. 23.

[101] Huang, W., Smith, T. B., and Gallimore, A. D., "Obtaining Velocity Distribution using a Xenon Ion Line with Unknown Hyperfine Constants," *40th AIAA Plasmadynamics and Laser Conference*, San Antonio, Texas, USA, 2009. https://doi.org/10.2514/6.2009-4226, AIAA-2009-4226.

[102] Svanberg, S., *Atomic and Molecular Spectroscopy*, 4th ed., Springer-Verlag, Berlin, Germany, 2004.

[103] Chaplin, V. H., Conversano, R. W., Lopez Ortega, A., Mikellides, I. G., Lobbia, R. B., and Hofer, R. R., "Ion Velocity Measurements in the Magnetically Shielded Miniature Hall Thruster (MaSMi) Using Laser-Induced Fluorescence," *36th International Electric Propulsion Conference*, Vienna, Austria, 2019. IEPC-2019-531.

[104] Pérez Luna, J., Hagelaar, G. J. M., Garrigues, L., and Boeuf, J. P., "Method to Obtain the Electric Field and the Ionization Frequency from Laser Induced Fluorescence Measurements," *Plasma Sources Sci. Technol.*, Vol. 18, 2009, p. 034008.

[105] Koslover, R., and McWilliams, R., "Measurement of Multidimensional Ion Velocity Distributions by Optical Tomography," *Rev. Sci. Instrum.*, Vol. 57, 1986, p. 2441.

[106] Huang, W., Frieman, J. D., Kamhawi, H., Peterson, P. Y., and Hofer, R. R., "Ion Velocity Characterization of the 12.5-kW Advanced Electric Propulsion System Engineering Hall Thruster," *AIAA Propulsion and Energy 2021 Forum*, Virtual Event, 2021. AIAA-2021-3432.

[107] Efron, B., "Bootstrap Methods - Another Look at the Jackknife," *Ann. Stat.*, Vol. 7, No. 1, 1979, pp. 1–26.

[108] Chaplin, V. H., Lobbia, R. B., Lopez Ortega, A., Mikellides, I. G., Roberts, P. J., Friss, A. J., Peter, J. S., Hofer, R. R., and Polk, J. E., "Spatiotemporally Resolved Ion Velocity Distribution Measurements in the 12.5 kW HERMeS Hall Thruster," *36th International Electric Propulsion Conference*, Vienna, Austria, 2019. IEPC-2019-532.

[109] Chernick, M. R., "Resampling Methods," *Wiley Interdisciplinary Reviews: Data Mining and Knowledge Discovery*, Vol. 2, No. 3, 2012, pp. 255–262.

[110] Sivia, D. S., and Skilling, J., *Data Analysis: A Bayesian Tutorial*, Oxford University Press, New York, 2006.

[111] Yim, J. T., "A Survey of Xenon Ion Sputter Yield Data and Fits Relevant to Electric Propulsion Spacecraft Integration," *35th International Electric Propulsion Conference*, Atlanta, GA, 2017. IEPC-2017-060.

[112] Konopliv, M. F., Chaplin, V. H., Johnson, L. K., and Wirz, R. E., "Accuracy of Using Metastable State Measurements in Laser-Induced Fluorescence Diagnostics of Xenon Ion Velocity in Hall Thrusters," *Plasma Sources Sci. Technol.*, Vol. 32, 2023, p. 015009. https://doi.org/10.1088/1361-6595/acb00b.

[113] Zhu, X., Wang, Y., Wang, Y., Yu, D., Zatsarinny, O., Bartschat, K., Tsankov, T. V., and Czarnetzki, U., "A Xenon Collisional-Radiative Model Applicable to Electric Propulsion Devices: II. Kinetics of the 6s, 6p, and 5d states of atoms and ions in Hall Thrusters," *Plasma Sources Sci. Technol.*, Vol. 28, No. 10, 2019, p. 105005. https://doi.org/10.1088/1361-6595/ab30b7.

[114] Romadanov, I., Raitses, Y., Diallo, A., Hara, K., Kaganovich, I. D., and Smolyakov, A., "On Limitations of Laser-Induced Fluorescence Diagnostics for Xenon Ion Velocity Distribution Function Measurements in Hall Thrusters," *Phys. Plasmas*, Vol. 25, 2018, p. 033501. https://doi.org/10.1063/1.5020749.

[115] Polk, J. E., Brophy, J. R., and Wang, J., "Spatial and Temporal Distribution of Ion Engine Accelerator Grid Erosion," *31st AIAA/ASME/SAE/ASEE Joint Propulsion Conference and Exhibit*, AIAA Paper 95-2924, 1995.

[116] Wang, J., Polk, J., Brophy, J., and Katz, I., "Three-Dimensional Particle Simulations of Ion-Optics Plasma Flow and Grid Erosion," *Journal of Propulsion and Power*, Vol. 19, No. 6, 2003, pp. 1192–1199. https://doi.org/10.2514/2.6939.

[117] Nakano, M., "Three-dimensional simulations of grid erosion in ion engines," *Vacuum*, Vol. 83, No. 1, 2003, pp. 82–85. https://doi.org/10.1016/j.vacuum.2008.03.080.

[118] Tartz, M., Hartmann, E., and Neumann, H., "Validated simulation of the ion extraction grid lifetime," *Review of Scientific Instruments*, Vol. 79, No. 2, 2008, pp. 02B905–02B905–4. https://doi.org/10.1063/1.2801376.

[119] Wirz, R. E., Anderson, J. R., and Katz, I., "Time-Dependent Erosion of Ion Optics," *Journal of Propulsion and Power*, Vol. 27, No. 1, 2012, pp. 211–217. https://doi.org/10.2514/1.46845.

[120] Walker, M., "Effects of Facility Backpressure on the Performance and Plume of a Hall Thruster," *PhD Thesis*, University of Michigan, Available: https://pepl.engin.umich.edu, 2005.

[121] Walker, M. L. R., Victor, A. L., Hofer, R. R., and Gallimore, A. D., "Effect of Backpressure on Ion Current Density Measurements in Hall Thruster Plumes," *Journal of Propulsion and Power*, Vol. 21, No. 3, 2005, pp. 408–415. https://doi.org/10.2514/1.7713.

[122] Cabrera, J., Jovel, D. R., and Walker, M. L. R., "Pressure Facility Effects on the Impedance Characteristics of a 9-kW HET," *38th International Electric Propulsion Conference*, Paper IEPC-2024-808, 2024.

[123] Zheng, H., Cai, G., Liu, L., Shang, S., and He, B., "Three-dimensional particle simulation of back-sputtered carbon in electric propulsion test facility," *Acta Astronautica*, Vol. 132, 2017, pp. 161–169. https://doi.org/10.1016/j.actaastro.2016.12.016.

[124] Crofton, M. W., Hsu Schouten, A. G., Young, J. A., Beiting, E. J., and Diamant, K. D., "Neutral Xenon Density in the SPT-140 Near-Field Plume," *33rd International Electric Propulsion Conference*, Paper IEPC-2013-399, 2013.

[125] Gottfried, J. A., Antozzi, S., Stienike, J., Thompson, S. J., Williams, J. D., and Yalin, A. P., "Temporally resolved relative krypton neutral density during breathing mode of a hall effect thruster recorded by TALIF," *Journal of Electric Propulsion*, Vol. 3, No. 1, 2024, p. 9. https://doi.org/10.1007/s44205-024-00070-5.

[126] Stienike, J., Antozzi, S., Ku, E., Thompson, S., Williams, J., and Yalin, A., "Spatially and Temporally Resolved Neutral Density Measurements in Plume of a Hallow Cathode by Two-Photon Absorption Laser Induced Fluorescence (TALIF)," *38th International Electric Propulsion Conference*, Paper IEPC-2024-401, 2024.

[127] Crofton, M. W., "Measurement of neutral xenon density profile in an ion thruster plume," *27th AIAA Plasma Dynamics and Lasers Conference*, AIAA Paper 1996-2290, 1996. https://doi.org/10.2514/6.1996-2290.

[128] Eichhorn, C., Löhle, S., Fasoulas, S., Leiter, H., Fritzsche, S., and Auweter-Kurtz, M., "Two-Photon Laser-Induced Fluorescence of Neutral Xenon in a Thin Xenon Plasma," *J. Propul. Power*, Vol. 28, No. 5, 2012, pp. 1116–1120. https://doi.org/10.2514/1.B34434.

[129] Eichhorn, C., Scholze, F., Bundesmann, C., Spemann, D., Neumann, H., and Leiter, H. J., "Two-Photon Laser-Induced Fluorescence in a Radiofrequency Ion Thruster Plume in Krypton," *J. Propul. Power*, Vol. 35, No. 6, 2019, pp. 1175–1178. https://doi.org/10.2514/1.b37487.

[130] Eichhorn, C., Pietzonka, L., Scholze, F., Bundesmann, C., Spemann, D., Neumann, H., and Leiter, H. J., "Single- and two-photon absorption laser-induced fluorescence spectroscopy in rare gases for gridded ion thruster diagnostics," *European Physical Journal: Techniques and Instrumentation*, Vol. 9, No. 1, 2022, p. 2. https://doi.org/10.1140/epjti/s40485-022-00077-y.

[131] Tsukizaki, R., Yamashita, Y., Kinefuchi, K., and Nishiyama, K., "Neutral atom density measurements of xenon plasma inside a μ10 microwave ion thruster using two-photon laser-induced fluorescence spectroscopy," *Vacuum*, Vol. 190, 2021, p. 110269. https://doi.org/10.1016/j.vacuum.2021.110269.

[132] Yamashita, Y., Tsukizaki, R., and Nishiyama, K., "Importance of stepwise ionization from the metastable state in electron cyclotron resonance ion thrusters," *Journal of Electric Propulsion*, Vol. 1, No. 1, 2022, p. 2. https://doi.org/10.1007/s44205-022-00002-1.

[133] Yamashita, Y., Tsukizaki, R., and Nishiyama, K., "Effect of ion beam extraction on neutral density distribution inside a gridded microwave discharge ion thruster," *Vacuum*, Vol. 200, 2022, p. 110962. https://doi.org/10.1016/j.vacuum.2022.110962.

[134] Bamford, D. J., Jusinski, L. E., and Bischel, W. K., "Absolute two-photon absorption and three-photon ionization cross sections for atomic oxygen," *Phys. Rev. A*, Vol. 34, No. 1, 1986, pp. 185–198. https://doi.org/10.1103/PhysRevA.34.185.

[135] Goehlich, A., Kawetzki, T., and Döbele, H. F., "On absolute calibration with xenon of laser diagnostic methods based on two-photon absorption," *J. Chem. Phys.*, Vol. 108, No. 22, 1998, pp. 9362–9370. https://doi.org/10.1063/1.476388.

[136] Niemi, K., Schulz-von der Gathen, V., and Döbele, H. F., "Absolute calibration of atomic density measurements by laser-induced fluorescence spectroscopy with two-photon excitation," *J. Phys. D: Appl. Phys.*, Vol. 34, No. 15, 2001, pp. 2330–2335. https://doi.org/10.1088/0022-3727/34/15/312.

[137] Bebb, H. B., and Gold, A., "Multiphoton Ionization of Hydrogen and Rare-Gas Atoms," *Phys. Rev.*, Vol. 143, No. 1, 1966, pp. 1–24. https://doi.org/10.1103/PhysRev.143.1.

[138] Bräunlich, P., *Multiphoton Spectroscopy*, Springer US, Boston, MA, 1979, pp. 777–827. https://doi.org/10.1007/978-1-4613-3935-9_4.

[139] Amorim, J., Baravian, G., and Jolly, J., "Laser-induced resonance fluorescence as a diagnostic technique in non-thermal equilibrium plasmas," *Journal of Physics D: Applied Physics*, Vol. 33, No. 9, 2000, p. R51. https://doi.org/10.1088/0022-3727/33/9/201.

[140] Niemi, K., Schulz-von der Gathen, V., and Döbele, H. F., "Absolute atomic oxygen density measurements by two-photon absorption laser-induced fluorescence spectroscopy in an RF-excited atmospheric pressure plasma jet," *Plasma Sources Sci. Technol.*, Vol. 14, No. 2, 2005, pp. 375–386. https://doi.org/10.1088/0963-0252/14/2/021.

[141] Wegner, T., Dumitrache, C., and Yalin, A. P., "Rate-Equation Modeling of Xe and Kr TALIF for Electric Propulsion Applications," *37th International Electric Propulsion Conference*, Paper IEPC-2022-298, 2022.

[142] Marx, B. R., Simons, J., and Allen, L., “The effect of laser linewidth on two-photon absorption rates,” *Journal of Physics B: Atomic and Molecular Physics*, Vol. 11, No. 8, 1978, p. L273. https://doi.org/10.1088/0022-3700/11/8/004.

[143] Olivero, J., and Longbothum, R., “Empirical fits to the Voigt line width: A brief review,” *Journal of Quantitative Spectroscopy and Radiative Transfer*, Vol. 17, No. 2, 1977, pp. 233–236. https://doi.org/https://doi.org/10.1016/0022-4073(77)90161-3.

[144] Liu, Y., Lin, J., Huang, G., Guo, Y., and Duan, C., “Simple empirical analytical approximation to the Voigt profile,” *Journal of the Optical Society of America B*, Vol. 18, No. 5, 2001, pp. 666–672. https://doi.org/10.1364/JOSAB.18.000666.

[145] Peze, P., Paillous, A., Siffre, J., and Dubreuil, B., “Quantitative measurements of oxygen atom density using LIF,” *Journal of Physics D: Applied Physics*, Vol. 26, No. 10, 1993, p. 1622. https://doi.org/10.1088/0022-3727/26/10/013.

[146] Halfmann, T., Rickes, T., Vitanov, N., and Bergmann, K., “Lineshapes in coherent two-photon excitation,” *Optics Communications*, Vol. 220, No. 4, 2003, pp. 353–359. https://doi.org/10.1016/S0030-4018(03)01368-3.

[147] Allen, L., and Peters, G. I., “Amplified Spontaneous Emission and External Signal Amplification in an Inverted Medium,” *Physical Review A*, Vol. 8, No. 4, 1973, pp. 2031–2047. https://doi.org/10.1103/PhysRevA.8.2031.

[148] Bonin, K. D., and McIlrath, T. J., “Two-photon electric-dipole selection rules,” *J. Opt. Soc. Am. B*, Vol. 1, No. 1, 1984, pp. 52–55. https://doi.org/10.1364/JOSAB.1.000052.

[149] Racah, G., “On a New Type of Vector Coupling in Complex Spectra,” *Phys. Rev.*, Vol. 61, 1942, pp. 537–537. https://doi.org/10.1103/PhysRev.61.537.

[150] Drag, C., Marmuse, F., and Blondel, C., “Measurement of the two-photon excitation cross-section of the 6p’$[3/2]_2$ and 6p’$[1/2]_0$ levels of Xe I at the wavelengths 224.3 and 222.6 nm,” *Plasma Sources Science and Technology*, Vol. 30, No. 7, 2021, p. 075026. https://doi.org/10.1088/1361-6595/abfbeb.

[151] Horiguchi, H., Chang, R. S. F., and Setser, D. W., “Radiative lifetimes and two-body collisional deactivation rate constants in Ar for Xe(5p^{5}6p),Xe(5p^{5}6p’), and Xe(5p^{5}7p) states,” *The Journal of Chemical Physics*, Vol. 75, No. 3, 1981, pp. 1207–1218. https://doi.org/10.1063/1.442169.

[152] Kröll, S., and Bischel, W. K., “Two-photon absorption and photoionization cross-section measurements in the $5p^5$6p configuration of xenon,” *Phys. Rev. A*, Vol. 41, 1990, pp. 1340–1349. https://doi.org/10.1103/PhysRevA.41.1340.

[153] Shekhtman, D., Mustafa, M. A., and Parziale, N. J., “Two-photon cross-section calculations for krypton in the 190–220 nm range,” *Appl. Opt.*, Vol. 59, No. 34, 2020, pp. 10826–10837. https://doi.org/10.1364/AO.410806.

[154] Chang, R. S. F., Horiguchi, H., and Setser, D. W., “Radiative lifetimes and two-body collisional deactivation rate constants in argon for Kr(4p^5)5p and Kr(4p^5)5p’ states,” *Journal of Chemical Physics*, Vol. 73, No. 2, 1980, pp. 778–790. https://doi.org/10.1063/1.440185.

[155] Dakka, M. A., Tsiminis, G., Glover, R. D., Perrella, C., Moffatt, J., Spooner, N. A., Sang, R. T., Light, P. S., and Luiten, A. N., “Laser-Based Metastable Krypton Generation,” *Phys. Rev. Lett.*, Vol. 121, 2018, p. 093201. https://doi.org/10.1103/PhysRevLett.121.093201.

[156] Alekseev, V. A., and Setser, D. W., “Quenching Rate Constants and Product Assignments for Reactions of Xe($7p[3/2]_2$, $7p[5/2]_2$, and $6p'[3/2]_2$) Atoms with Rare Gases, CO, H_2, N_2O, CH_4, and Halogen-Containing Molecules,” *J. Phys. Chem.*, Vol. 100, 1996, pp. 5766–5780. https://doi.org/10.1021/jp952402c.

[157] Antozzi, S., Gottfried, J., Williams, J. D., and Yalin, A. P., “Spatially Resolved Measurements of Krypton by Two-photon Absorption Laser Induced Fluorescence (TALIF) in a Barium Oxide Hollow Cathode Plasma,” *AIAA Aviation 2023 Forum*, AIAA Paper 2023-4269, 2023. https://doi.org/10.2514/6.2023-4269.

[158] Bounds, J., Kolomenskii, A., Trainham, R., Manard, M., and Schuessler, H., “Hyperfine structure and isotope shifts of xenon measured for near-infrared transitions with Doppler-free saturated absorption spectroscopy,” *Spectrochimica Acta Part B: Atomic Spectroscopy*, Vol. 202, 2023, p. 106635. https://doi.org/https://doi.org/10.1016/j.sab.2023.106635.

[159] Bruce, M. R., Layne, W. B., Whitehaed, C. A., and Keto, J. W., "Radiative lifetimes and collisional deactivation of two-photon excited xenon in argon and xenon," *Journal of Chemical Physics*, Vol. 92, 1990, pp. 2917–2925. https://doi.org/10.1063/1.457939.

[160] Whitehead, C. A., Pournasr, H., Bruce, M. R., Hong Cai, Kohel, J., Layne, W. B., and Keto, J. W., "Deactivation of two-photon excited Xe($5p^5$6p,6p',7p) and Kr($4p^5$5p) in xenon and krypton," *Journal of Chemical Physics*, Vol. 105, No. 5, 1995, pp. 1965–1980. https://doi.org/10.1063/1.468763.

[161] Crofton, M. W., Dale, E. T., and Thuppul, A., "Electric Thruster Ingestion and Background Propellant Density Measurements," *38th International Electric Propulsion Conference*, Paper IEPC-2024-367, 2024.

[162] Schmidt, J. B., Roy, S., Kulatilaka, W. D., Shkurenkov, I., Adamovich, I. V., Lempert, W. R., and Gord, J. R., "Femtosecond, two-photon-absorption, laser-induced-fluorescence (fs-TALIF) imaging of atomic hydrogen and oxygen in non-equilibrium plasmas," *Journal of Physics D: Applied Physics*, Vol. 50, No. 1, 2016, p. 015204. https://doi.org/10.1088/1361-6463/50/1/015204.

[163] Gottfried, J. A., and Yalin, A. P., "Krypton tagging velocimetry in the plume of a plasma hollow cathode," *Opt. Continuum*, Vol. 3, No. 1, 2024, pp. 9–21. https://doi.org/10.1364/OPTCON.503138.

[164] Mustafa, M. A., and Parziale, N. J., "Simplified read schemes for krypton tagging velocimetry in N2 and air," *Opt. Lett.*, Vol. 43, No. 12, 2018, pp. 2909–2912. https://doi.org/10.1364/OL.43.002909.

[165] Parziale, N. J., Smith, M. S., and Marineau, E. C., "Krypton tagging velocimetry of an underexpanded jet," *Appl. Opt.*, Vol. 54, No. 16, 2015, pp. 5094–5101. https://doi.org/10.1364/AO.54.005094.

[166] Shekhtman, D., Yu, W. M., Mustafa, M. A., Parziale, N. J., and Austin, J. M., "Freestream velocity-profile measurement in a large-scale, high-enthalpy reflected-shock tunnel," *Exp. Fluids*, Vol. 62, No. 5, 2021, p. 118. https://doi.org/10.1007/s00348-021-03207-6.

[167] Uddi, M., Jiang, N., Mintusov, E., Adamovich, I. V., and Lempert, W. R., "Atomic oxygen measurements in air and air/fuel nanosecond pulse discharges by two photon laser induced fluorescence," *Proceedings of the Combustion Institute*, Vol. 32, No. 1, 2009, pp. 929–936. https://doi.org/https://doi.org/10.1016/j.proci.2008.06.049.

[168] Crofton, M. W., Moore, T. A., Boyd, I. D., Masuda, I., and Gotoh, Y., "Near-Field Measurement and Modeling Results for Flight-Type Arcjet: Hydrogen Atom," *Journal of Spacecraft and Rockets*, Vol. 38, No. 3, 2001, pp. 417–425. https://doi.org/10.2514/2.3700.

[169] Jolly, J., and Booth, J.-P., "Atomic hydrogen densities in capacitively coupled very high-frequency plasmas in H2: Effect of excitation frequency," *Journal of Applied Physics*, Vol. 97, No. 10, 2005, p. 103305. https://doi.org/10.1063/1.1900290.

[170] Mazouffre, S., Foissac, C., Supiot, P., Vankan, P., Engeln, R., Schram, D. C., and Sadeghi, N., "Density and temperature of N atoms in the afterglow of a microwave discharge measured by a two-photon laser-induced fluorescence technique," *Plasma Sources Science and Technology*, Vol. 10, No. 2, 2001, p. 168. https://doi.org/10.1088/0963-0252/10/2/306.

[171] Rosell, J., Sjöholm, J., Richter, M., and Aldén, M., "Comparison of Three Schemes of Two-Photon Laser-Induced Fluorescence for CO Detection in Flames," *Applied Spectroscopy*, Vol. 67, No. 3, 2013, pp. 314–320. https://doi.org/10.1366/12-06704.